Stratigraphy, Ore Mineralogy, Geochemistry, and Genesis of Gold-Bearing Quartz Veins at the Hog Mountain Tonalite, Southwestern Appalachians, USA

by

Anabelle Katherine Kline

A Thesis submitted to the Graduate Faculty of
Auburn University
in partial fulfillment of the
requirements for the Degree of
Master of Science

Auburn, Alabama
May 5, 2019

Keywords: gold-bearing quartz veins; ore mineralogy; hydrothermal fluid conditions; electron microprobe; sulfur isotope; Hog Mountain

Approved by

Dr. Laura D. Bilenker, Chair, Assistant Professor of Economic Geology
Dr. Stefanie M. Brueckner, Research Associate, Laurentian University
Dr. Mark G. Steltenpohl, Professor of Structural Geology
Dr. Willis E. Hames, Professor of Mineralogy and Metamorphic Petrology

Abstract

Hog Mountain of the southern Appalachians is a gold deposit in the eastern Blue Ridge of Alabama. The mineralized quartz veins found there have an average Au grade of 0.14 oz/t (maximum: 2.4 oz/t Au) and occur within a tonalite that intruded into the moderately metamorphosed phyllites of the Wedowee Group during the Neoacadian orogeny. Vein formation and mineralization is epigenetic and took place during the Pennsylvanian-Permian Alleghanian orogeny. This study employed a multi-faceted observational and geochemical approach to understanding the genesis of Hog Mountain; core logging, microscopy (reflected light, scanning electron microscope), and electron microprobe analysis provided important textural and compositional data, whereas sulfur isotopic analysis allowed for source fingerprinting of the ore-forming fluids.

The quartz ± plagioclase ± calcite veins at Hog Mountain have an ore assemblage dominated by pyrrhotite with minor to trace pyrite and trace arsenopyrite – chalcopyrite ± sphalerite – Bi-Te-Au±S phases. Gold mineralization is spatially related to Bi±Te±S phases and it occurs dominantly as native gold and electrum and rare maldonite.

Electron microprobe analyses show a wide range of Bi (80-509 ppm), Au (97-627 ppm), and Co (33-1130 ppm) within base metal sulfides. Native bismuth and Bi-chalcogenides have relatively elevated concentrations of Ag, Sb, Pb, S, and Se up to several 1000 ppm due to preferred substitution of these elements for Bi and Te. Electrum has an Au/Ag ratio of 10.4.

Sulfur isotopic compositions of sulfides emerge as two populations: Group 1, $\delta^{34}S_{sulfide}$ = 5.2 to 9.0 ‰, average: 7.7 ± 0.9 ‰; Group 2, $\delta^{34}S_{sulfide}$ = 11.6 to 15.2 ‰, average: 12.9 ± 1.4 ‰. The sulfides in each group differ in occurrence and texture; Group 1 represents the dominant ore assemblage and main stage of mineralization, whereas Group 2 sulfides were late stage.

The ore mineralogy at Hog Mountain is consistent with reduced, nearly neutral, relatively H_2S- and CO_2-rich, low saline fluids with relatively high f_{Te2} that allowed telluride precipitation. Fluid temperatures ranged between 400-200 ºC. Sulfur and metals originated from the surrounding metasedimentary rocks and variations in $\delta^{34}S$ reflect changes in the redox state of the hydrothermal fluid. Interaction with tonalite or mixing with meteoric water is excluded as S and metal sources. Gold precipitation occurred via Au scavenging by Bi(±Te) melts that formed directly from the reduced hydrothermal fluid at temperatures > 271 ºC due to the breakdown of Bi_2S_2OH-complexes. Molten droplets of Bi±Te±Au±S were remobilized during syngenetic vein and sulfide crystallization.

With these new data, this study confidently classifies Hog Mountain as an orogenic gold deposit rather than a reduced intrusion-related gold deposit despite overlapping characteristics (e.g., hosted by a reduced tonalite). Importantly, no metal zoning occurs around the veins, veins are younger than the intrusion, and they display no distinct changes in ore grade. Establishing this genetic model for Hog Mountain impacts on-going and future exploration in the southernmost Appalachians.

Acknowledgments

First, I would like to thank Wellborn Mining LLC for providing funding for this project and allowing me to use their facilities and drill core. More specifically, thank you to Mark Whitney, Josh Poole, and Jody East for helping me in any way possible. I enjoyed getting to spend time and learn from each of you. Thank you, also, to SEG, the Auburn University Department of Geosciences Advisory Board and donors of the Bob Fousek award for providing additional financial support for my research. To the lab technicians I spent many hours with while in Canada, including Glenn Piercy (MUN), David Grant (MUN), Dylan Goudie (MUN), Wanda Aylward (MUN), and Mitch Kerr (SMU), thank you for your expertise and patience. Thank you to my undergraduate apprentice, Sophie Milich for the many hours of help. To the staff of the Department of Geosciences (Ashleigh Rudd, Miss Pam, Miss Jackie, and Tony Hall), thank you for making the day-to-day tasks less stressful and always being there for moral support. To all of my fellow graduate students, thank you for struggling along side of me and making the past two years very enjoyable. I will always remember the memories we made. Thanks to Dr. Steltenpohl and Dr. Hames for serving on my committee and for offering your expert advice. A special “thank you” to my parents, sister, brother-in-law, and grandparents for supporting me through all of my education, but especially these past two years. To Trey Foster, thank you for helping me stay sane. I couldn’t have done it without your support. To the many professors at Auburn University that I have come to know very well, thank you for everything you’ve done for me. Finally, I would like to thank my two advisors, Dr. Bilenker and Dr. Brueckner. Dr. Bilenker, thank you for willingly taking me on

as a student mid-way through my project and never skipping a beat. I have learned so much from you in the short period of time we worked together, and value your mentorship very highly. Dr. Brueckner, thank you for introducing me to economic geology and sticking with me through my masters. This project would not be possible without you, and I would not be where I am today without your abundance of knowledge and guidance. I consider both of you a mentor and a friend.

Table of Contents

List of Tables

List of Figures

List of Appendices

List of Abbreviations

AC	Alexander City Fault
Ag-Te	Hessite
AL	Alabama
Apy	Arsenopyrite
Au-Bi	Maldonite
AUS	Australia
bdl	Below detection limit
BF	Brevard Fault
Bi-S	Bismuthinite
Bi-Te	Bismuth telluride(s)
BIF	Banded iron formation
Bio	Biotite
Bis	Bismuthinite
BSE	Back scattered electron
C	Cambrian
CAN	Canada
Ccp	Chalcopyrite
CHI	China
Chl	Chlorite
cm	centimeter
CREAIT	Core Research Equipment and Instrument Training
CZE	Czech Republic
D	Devonian
$D_{1, 2, 3, 4, 6}$	Deformation event 1, 2, 3, 4, 6
EBR	eastern Blue Ridge
EDX	Energy dispersive X-ray
e.g.	exempli gratia (for example)
El	Electrum
EMPA	Electron microprobe analysis
EOH	End of Hole
Eq.	Equation

eq.	Equivalent
f_{O2}	Oxygen fugacity
f_{Te2}	Tellurium fugacity
Fig.	Figure
Figs.	Figures
ft	Feet
G-E	Goodwater-Enitachopca Fault
Gn	Galena
g/t	Gram per ton
Hed	Hedleyite
Hess	Hessite
HLF	Hollins Line Fault
HM	Hog Mountain
i.e.	id est (in other words)
IMF	Instrument mass fractionation
in	Inch(es)
J	Jurassic
K	Kreide (Cretaceous)
kbar	Kilo bar
keV	Kiloelectron Volt
km	Kilometer
LCME	Low melting chalcophile elements
LIF, LIFH	Lithium fluoride
LLC	Limited Liability Company
m	Molal
$M_{1, 2}$	Metamorphism event 1 or 2
Ma	Millenum annum (million years)
Mal	Maldonite
Max	Maximum measured value
mM	Millimolar
mi^2	Square miles
Min	Minimum measured value
mol%	Mole percent

Mt	Magnetite
MUN	Memorial University of Newfoundland
n	Number of analyses
nA	Nano Ampere
NAD-83	North American Datum 1983
native Au	Native gold
native Bi	Native bismuth
NNW	North-north-west
O	Ordovician
oz/t	Ounce per ton
P	Pressure
P [Fig. 2.14]	Permian
pA	Pico Ampere
PETL	Pentaerythritol
pH	Power of the concentration of the hydrogen ion
Plag	Plagioclase
Po	Pyrrhotite
ppb	Parts per billion
ppm	Parts per million
Py	Pyrite
PyPoMt	Pyrite-pyrrhotite-magnetite assemblage
QMKA	Quartz–muscovite–(K) feldspar–albite assemblage
Qtz	Quartz
RIRG	Reduced intrusion-related gold
RUS	Russia
S	Silurian
sec	Seconds
SEM	Scanning electron microscopy
SEM [Tables 2.3 and 2.7]	Standard error mean
SIMS	Secondary ion mass spectrometry
Sp	Sphalerite
SSE	South-south-east

Std	Standard deviation
T	Temperature
T [Fig. 2.14]	Triassic
T-max	Peak metamorphic temperature
TAP	Thallium acid phthalate
TCF	Talladega-Cartersville Fault System
Tr	Triassic
US	Unites States
USA	United States of America
USGS	United States Geological Survey
UTM	Universal Transverse Mercator
UZB	Uzbekistan
VCDT	Vienna Canyon Diablo Troilite
VHMS	Volcanic hosted massive sulfide
vol%	Volume percent
WBR	western Blue Ridge
wt%	Weight percent
X_{CO2}	Amount of CO_2 in a system relative to the whole system (e.g., X_{CO2} = 0.1 means CO_2 =10%)
Å	Angstrom
€	Cambrian
p€	Pre-Cambrian
$\delta^{34}S$	Sulfur isotopic composition of any substance relative to a reference material expressed in delta notation and given in per mil
µm	Micrometer
σ	Sigma
ΣAu	Total gold
ΣS	Total sulfur
‰	Per mil
ºC	Degrees Celsius
✓	Analyzed

Chapter 1

Background and Previous Research

1.1 Orogenic Gold Deposits

Orogenic gold deposits account for one third of the gold mined worldwide and belong to the broad class of hydrothermal ore deposits. Orogenic gold deposits, sometimes also referred to as mesothermal deposits, are a type of Au-bearing hydrothermal deposit that have formed ubiquitously throughout geologic time, from the Archean through today. These deposits are a product of continental margin deformational events (Fig. 1.1) and occur in three main environments within collisional orogens: (1) Archean and early Proterozoic greenstone belts, (2) slate belts, and (3) Cordilleran-type orogenic belts (Groves et al., 1998).

Consistently associated with deformation and metamorphism, orogenic gold deposits are hosted in low grade sub-greenschist metamorphic facies to higher metamorphic grades of lower-amphibolite facies associated with intrusions. Ore deposition typically occurs between 250-450 ºC, 1-5 kbar and 3-15 km depth (Fig. 1.2; Groves et al., 1998). The orebodies are structurally controlled, forming steep-dipping vein systems of continuous ore grade that were created by brittle-ductile faulting and fracturing during tectonic stress. Smaller, sub-vertical shear veins that may also contain gold can be associated with steep-dipping mineralized veins as a result of an extensional environment (tension) during deformation (Jébrak and Marcoux, 2015). Brittle deformation is necessary to create the pathways for ascending hydrothermal fluids; however, those steep-dipping faults can pre-date the mineralization and be reactivated during later metamorphism and deformation within collisional environments.

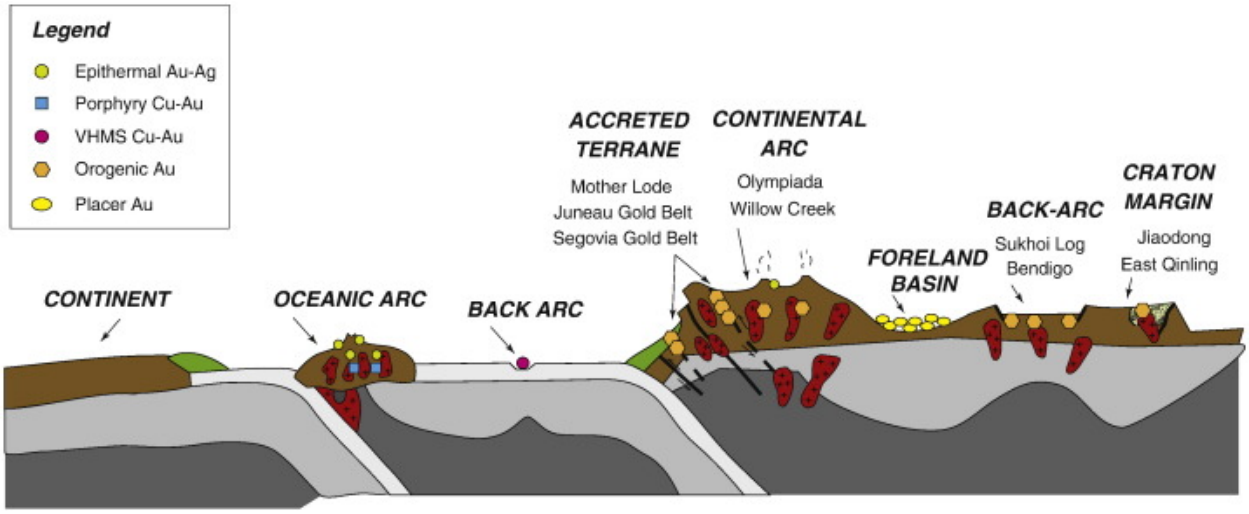

Figure 1.1. Cross-section of tectonic settings hosting hydrothermal ore deposits. Orogenic gold deposits are marked with orange hexagon. (Goldfarb and Groves, 2015)

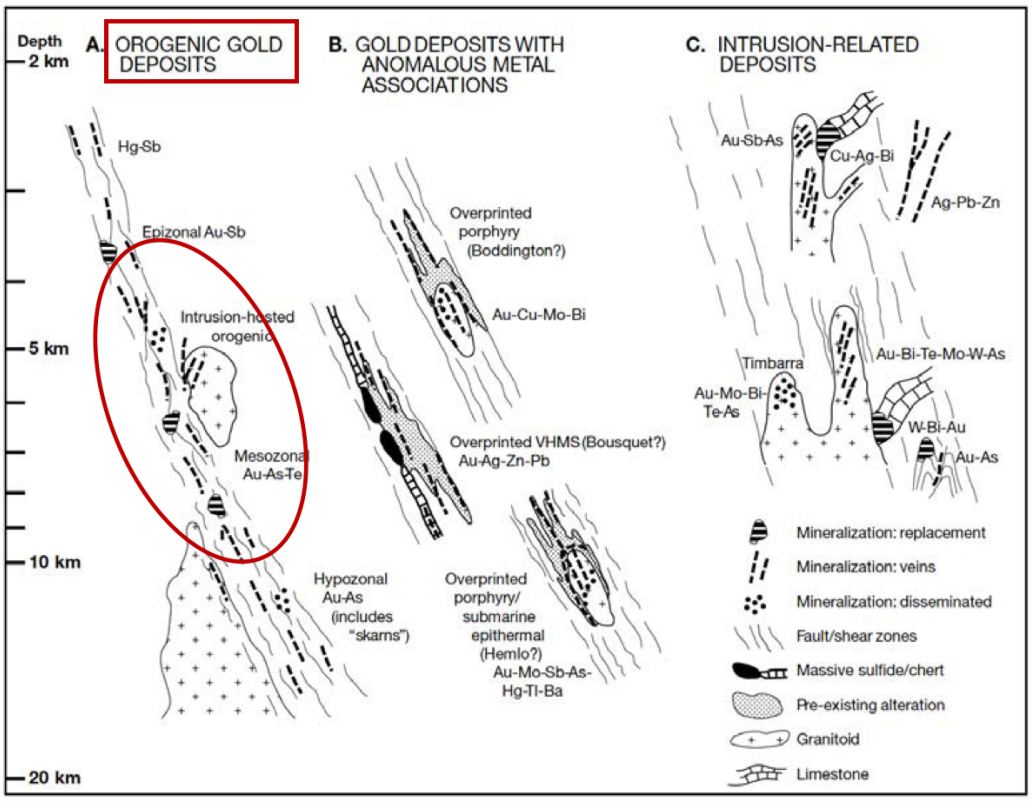

Figure 1.2. Types of gold mineralization within the continental crust. (**A)** Orogenic gold deposits; the Hog Mountain deposit belongs to this group. Red ellipse highlights the typical depth and style of orogenic gold deposits such as Hog Mountain. (**B)** Gold deposits with anomalous metal associations. **(C)** Intrusion-related gold deposits. (Groves et al., 1998)

The metals carried in the hydrothermal fluid precipitate along these faults when the physico-chemical fluid conditions change from transport-favored to deposition-favored. Such changes include changes in temperature, pH, pressure and/or redox potential of the metal-carrying fluid.

The mineralized quartz veins of orogenic gold deposits usually contain <3-5% sulfide minerals and <5-15% carbonate minerals (Groves et al., 1998). The most common sulfide mineral in metasedimentary host rocks is arsenopyrite, whereas pyrite or pyrrhotite dominate in metamorphosed igneous rocks. Hydrothermal fluids associated with orogenic gold deposits commonly have a low salinity and near neutral pH, with CO_2 concentrations between 0.05-0.25 moles/L, and a high enough concentration of H_2S to allow the transport of gold as a thio-complex (Groves et al., 1998). As the hydrothermal fluid rises, the thio-complexes interact with Fe-bearing minerals in the wall rock, forming Fe-sulfides such as pyrite or pyrrhotite. The hydrothermal fluid also becomes reduced, limiting the transport of gold as an aqueous thio-complex and resulting in the precipitation of native gold or less commonly as the gold alloy electrum (Au, Ag).

Alteration haloes around mineralized quartz veins in orogenic gold deposits are commonly thin and rarely exceed 3 meters (Jébrak and Marcoux, 2015). Alteration mineralogy is also highly dependent on the host rock composition and metamorphic grade (Fig. 1.3). The alteration assemblage is based on the mineralogical stability at the pressure and temperature conditions at which the host rock(s) is metamorphosed (Jébrak and Marcoux, 2015). Common alteration minerals found in orogenic gold deposits include carbonates, chlorite, calcite, and sulfides. There is not a strong relation between the size of the alteration halo found in the host rock and the thickness of the quartz vein.

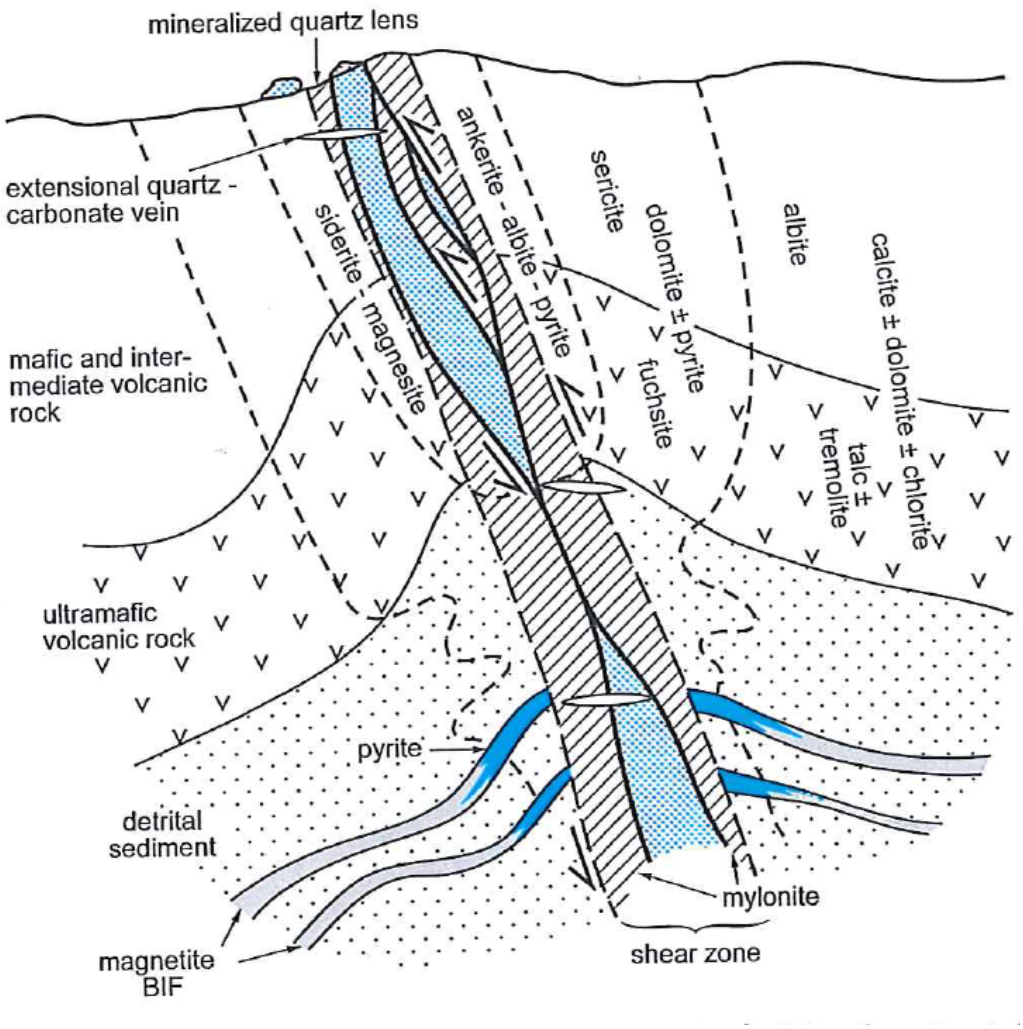

Figure 1.3. Change in alteration mineralogy with varying host rock composition around mineralized quartz veins. (Jébrak and Marcoux, 2015)

1.2 Origin of Hydrothermal Fluids

Hydrothermal fluids responsible for the formation of orogenic fluids form in the lower crust due to increased temperature and pressure at regional metamorphic conditions (Fig. 1.4; Yardley and Cleverley, 2015). Due to the higher water content and decrease in porosity with increasing temperature, many researchers favor metasedimentary rocks over meta-igneous rocks as the source of the hydrothermal fluids that are responsible for orogenic gold deposits. However, the topic remains highly debated in the literature (Groves et al., 1998; Goldfarb et al., 2005; Cox, 1987, 2005; Yardley and Cleverly, 2015). Sedimentary rocks become low-porosity metamorphic rocks such as slate, phyllite or schist during diagenesis and metamorphism, and fluid that exists in the pore spaces and within fractures is expelled as a result (Yardley and Cleverley, 2015). As prograde metamorphism continues, additional fluid is released by mineral breakdown reactions or metamorphic devolatilization reactions taking place over several millions of years (Cartwright and Oliver, 2000).

Devolatilization breaks down minerals to form new, less hydrous minerals and the expelled fluids become enriched in soluble components including chloride complexes and sulfide complexes that are necessary to transport metals in solution. With increasing temperature during prograde metamorphism, the volume of released hydrothermal fluids also increases resulting in an increase in the hydrostatic pressure. Fluids are released into overlying crust along faults and fractures that are created by the fluids (hydrostatic pressure > lithostatic pressure), earthquakes, and/or pre-existing pathways (Cartwright and Oliver, 2000; Weatherley and Henley, 2013). The expelled fluids continue migrating along an upward-focused fluid flow pathway due to the density differences between the hydrothermal, metal-carrying fluid and the wall rock.

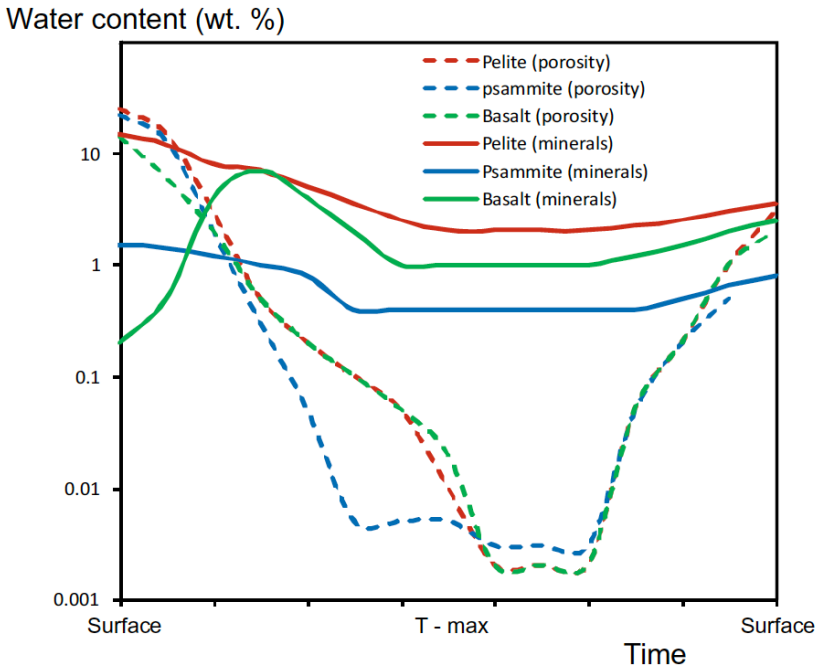

Figure 1.4. **Time versus water content of supracrustal rocks undergoing an idealized metamorphic cycle.** Note that pelites (red solid line) have the highest water content due to the increased proportion of clay minerals compared to basalt (green solid line) and psammite (blue solid line). Porosity of basalts (green dotted line) decreases the fastest with increasing temperature, whereas the porosity of sedimentary rocks (red and blue dotted lines) decreases significantly only near peak metamorphic temperature conditions (T-max). (Yardley and Cleverly, 2015)

The path of the fluid is determined by rock strength because the high fluid pressure at metamorphic temperatures can cause the rock to weaken and crack. Therefore, it is common to observe syn-metamorphic veins in regionally metamorphosed rocks (Cartwright and Oliver, 2000). The direction of fluid flow can also be influenced by faults, shear zones, dilation and closing of veins, and zones of unequal strain (Cartwright and Oliver, 2000).

1.3 Physico-Chemical Characteristics of Hydrothermal Fluids

Metamorphic fluids that form hydrothermal fluids when ascending through the crust are dominantly a mixture of H_2O, CO_2, and a dissolved load of (metal) ions. The composition of hydrothermal fluids formed by metamorphic devolatilization depends on: (1) the composition of the protolith (sedimentary or igneous) and (2) the chemical reactions between the hydrothermal fluid and wall rock during its ascent (Goldfarb et al., 2005; Yardley, 2005; Pitcairn et al., 2006; Tomkins, 2010).

As the hydrothermal fluid migrates upward through the crust along fluid pathways, it leaches metals and other elements from the wall rock. Reactions between the wall rock and the ascending hydrothermal fluids changes the mineral content of the wall rock in immediate contact with the fluids creating narrow alteration haloes of varying composition around mineralized quartz veins as a function of wall rock composition (Fig. 1.3; Yardley, 2005; Jébrak and Marcoux, 2015). Each wall rock interaction has the potential to alter the physico-chemical characteristics of the hydrothermal fluid and its ability to transport metals (Yardley, 2005). Some of the most important characteristics of ascending hydrothermal fluids affecting ore formation include a change in chemical composition, salinity, pH, and redox state.

The most important characteristic of a hydrothermal fluid is the chemical composition derived from interactions with the wall rock (Yardley, 2005) as the presence of different complexes determines what metals can be transported (e.g., chloride or chloro-complexes, sulfide or thio-complexes). Gold can be transported as a chloro- or thio-complex, although fluid temperature, pH, and the amount of dissolved chloride and sulfur control Au transport in hydrothermal fluids within an orogenic setting (Fig. 1.5; Stefánsson and Seward, 2004; Williams-Jones et al., 2009). Since the metal composition of hydrothermal fluids depends largely on its origin, interaction with the wall rock, and the water to rock ratio, most hydrothermal fluids that form orogenic gold deposits contain a limited amount of dissolved metals (Fe, Au, As ± Cu ± Zn ± Pb), resulting in simple sulfide mineralogy consisting of pyrite, pyrrhotite, arsenopyrite, chalcopyrite, electrum or native gold ± minor ± sphalerite ± galena (Goldfarb et al., 2005; Jébrak and Marcoux, 2015).

One of the most common rock types in the Earth's crust are metapelites, which contain carbon as carbonates and sulfur as sulfides. The metamorphic breakdown of these minerals produces CO_2 and SO_2, respectively (Cartwright and Oliver, 2000). Other rock types found in the crust produce different hydrothermal fluid compositions. For example, impure marbles and calc-silicates produce an H_2O-rich fluid that becomes CO_2-rich as temperatures increase, whereas pure calcite marbles will only undergo reaction at high temperatures and/or low pressures (Cartwright and Oliver, 2000). Mafic and ultramafic rocks only make up a small portion of the metamorphosed lower crust and during prograde metamorphism, the hydrous minerals they contain do not undergo dehydration until temperatures exceed upper greenschist facies conditions resulting in low volumes of fluid at moderate metamorphic facies conditions (Cartwright and Oliver, 2000). The composition of the host rock also controls salinity, redox state, and pH of the hydrothermal fluid, which in turn control the amount and type of metals transported. A change in any of these

parameters affects the amount of dissolved ligands available and therefore determines the amount of metals that can be transported (e.g., Williams-Jones et al., 2009; Zhu et al., 2011).

Salinity is expressed as the amount of dissolved NaCl in the hydrothermal fluid and can change due to: (1) dissolution of evaporites in the host rock or wall rock with which the fluid interacts; (2) mixing with meteoric water or other fluids (e.g., magmatic fluids) during ascent; and (3) addition of the products from retrograde hydration reactions (Yardley and Graham, 2002). Salinity plays a major role in ore formation, because the addition of salt (NaCl) to H_2O-CO_2-rich hydrothermal fluids can cause phase separation into immiscible fluid and vapor phases (Yardley and Cleverley, 2015). The salinity of hydrothermal fluids rises with temperature due to the increased solubility of NaCl at higher temperatures. Chloride is the dominant ligand for many metals including Cu, Zn, Pb, Ag and Au (Seward, 1976, 1984; Lydon, 1988; Seward and Barnes, 1997). On the other hand, metals including Au, As, Fe, Sb, Tl, and Hg complex with sulfur to form thio-complexes (Stefánsson and Seward, 2004; Williams-Jones et al., 2009; Yardley and Graham, 2002) or OH^- to form hydroxide complexes (Heinrich and Eadington, 1986; Wood et al., 1987).

Despite the important role of salinity in ore-forming hydrothermal fluids, orogenic gold deposits are commonly formed from fluids with low to moderate salinity (2-10 wt% NaCl eq.; Jébrak and Marcoux, 2015) resulting in a simple sulfide mineralogy made of metals such as Fe, As, and Au. Therefore, the dominant complexes that transport Au in orogenic gold systems are thio-complexes (Fig. 1.6; Goldfarb et al., 2005).

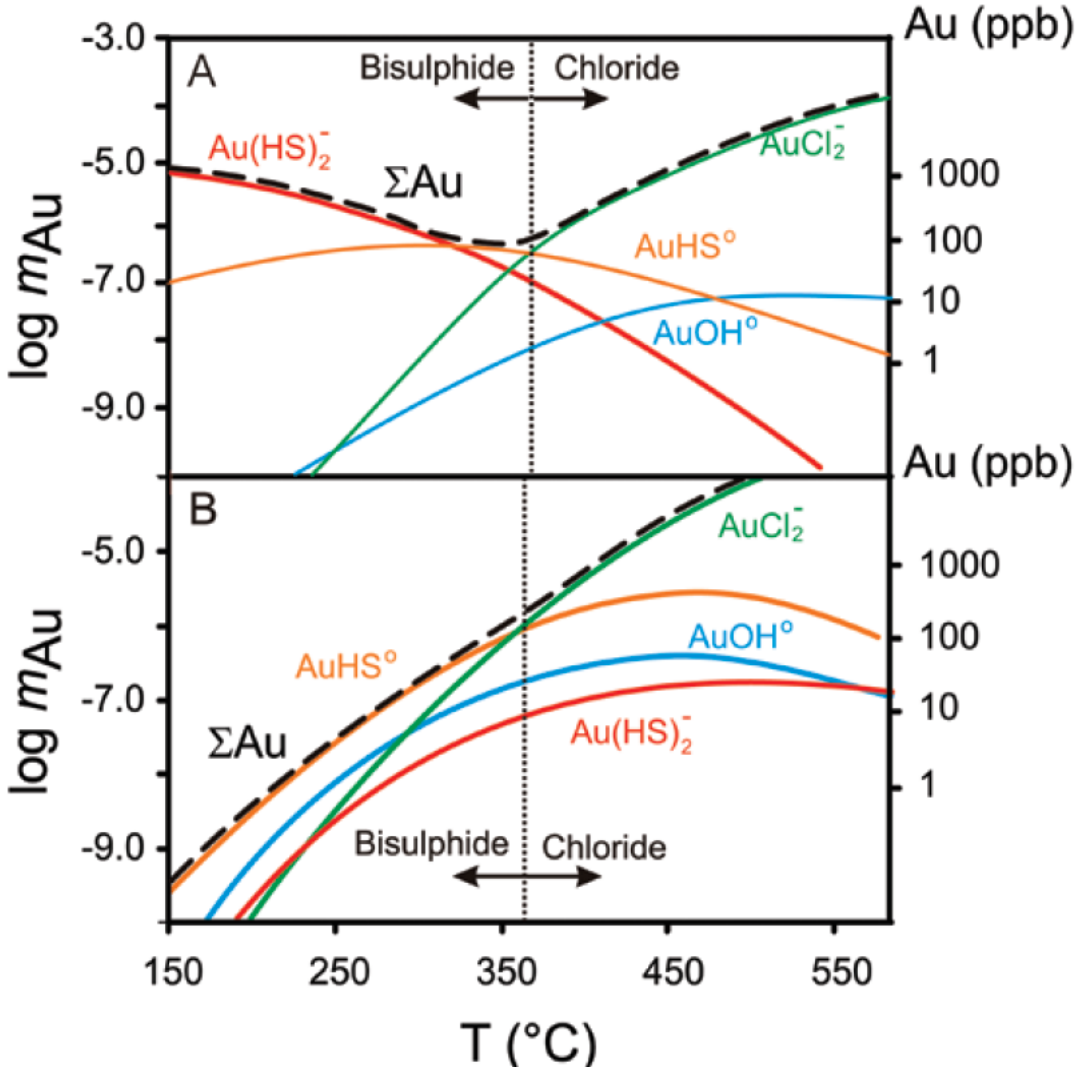

Figure 1.5. Gold solubility as function of temperature. Gold solubility (in terms of molality and parts per billion) and speciation at 1 kbar as a function of temperature for an aqueous solution containing 1.5 m NaCl and 0.5 m KCl, with pH buffered by the assemblage K-feldspar–muscovite–quartz. **A)** ΣS = 0.01 m and f_{O2} is buffered by the assemblage hematite–magnetite. **B)** ΣS and f_{O2} are buffered by the assemblage pyrite–pyrrhotite–magnetite; the maximum value of ΣS is 0.1 m. The black dashed line (ΣAu) indicates the total solubility of gold. (Williams-Jones et al., 2009 with data from Stefánsson and Seward, 2004 and Johnson et al., 1992).

The redox state of the hydrothermal fluid also influences the amount of metals transported as a direct function of the interaction of the fluid with wall rock. For example, sulfide complexes such as H_2S and HS^- are stable at reduced conditions (Yardley, 2005). This allows metals such as gold to bond with the reduced sulfur to form a thio-complex. If fluid conditions become more oxidized due to interaction with oxidized minerals in the wall rock, the sulfur will react with the oxygen to form sulfate ions, resulting in Au deposition.

The hydrothermal fluid pH, or concentration of hydrogen ions within the hydrothermal fluid, is very sensitive to the concentration of HS^-, especially when the concentration of HS^- reaches approximately 10 mM (Yardley, 2005). At this concentration, the pH of the hydrothermal fluid is acidic (Fig. 1.7; Yardley, 2005; Seward et al., 2013) and Au transport as a thio-complex is favored between pH = 2-5. At pH < 2, Au is transported as a chloro-complex (Fig. 1.8; Seward et al., 2013).

The transport of metals, and in particular Au, as either chloro- or thio-complexes is a complicated function of temperature, fluid composition, water-rock interaction, salinity, redox, and pH. Therefore, it is imperative to constrain these physico-chemical parameters in order to understand the formation of orogenic gold deposits such as Hog Mountain.

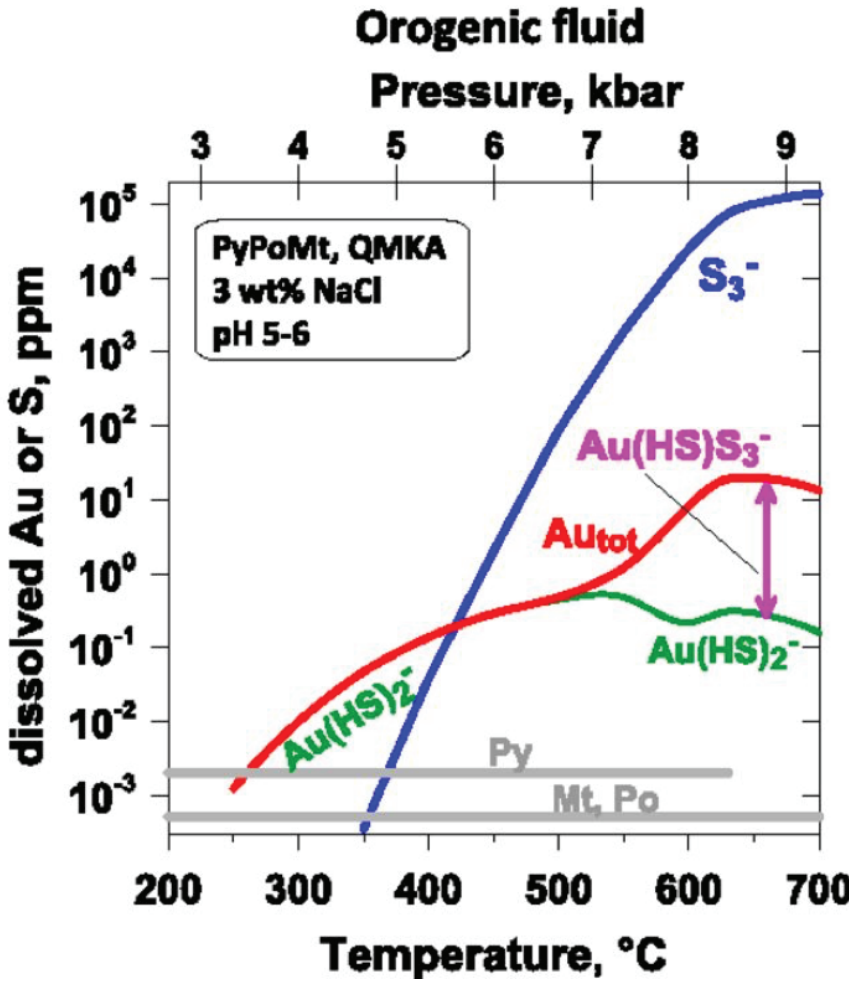

Figure 1.6. Hydrothermal fluids that form orogenic gold deposits transport gold as a thio-complexes. Abbreviations: PyPoMt – pyrite-pyrrhotite-magnetite assemblage, QMKA – quartz–muscovite–(K) feldspar–albite assemblage (Pokrovski et al., 2015)

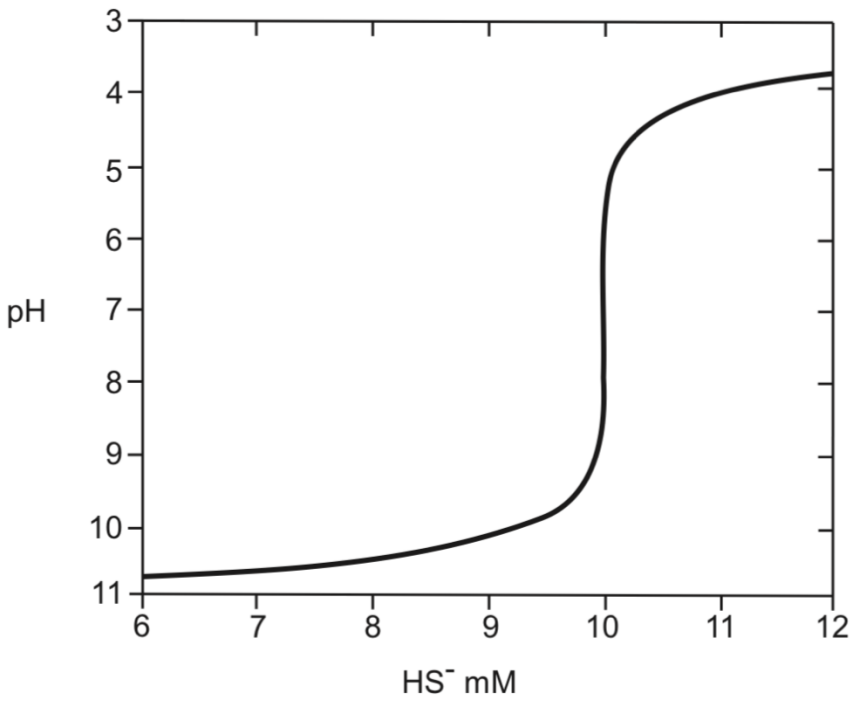

Figure 1.7. The pH of a fluid is extremely sensitive to the concentration of HS^-. With increasing HS^-, pH decreases, and Au is transported as a thio-complex. (Seward et al., 2013)

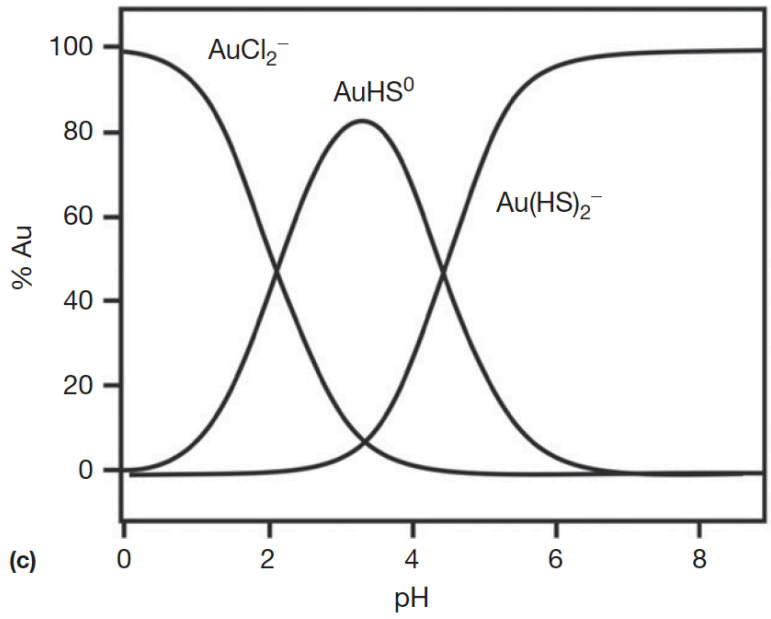

Figure 1.8. Preferred complexing of Au based on pH. When pH < 2, Au is transported as chloro-complex, whereas at pH > 2, Au is transported by thio-complexes (Seward et al., 2013)

1.4 Previous Research

The Hog Mountain area and the surrounding Goldville district are historic gold districts where mining dates back to the 19th century during the Alabama gold rush (Park, 1935). Gold has been known to exist on the Hog Mountain property since 1839 and regular mining operations began in 1903 by Hillabee Gold Mining Co. (Aldrich, 1909). At this time, Aldrich (1909) started to investigate the mineralogical associations of the gold, in order to determine how to best extract it by experimenting with methods employing cyanide and mercury.

Some of the first geological research in the area was performed by Park (1935), who identified the host lithologies and associated gold mineralization. Dominant mineralogy included sericite, pyrrhotite, chalcopyrite, pyrite, arsenopyrite, gold, sphalerite, galena, bismuth, and silver (Park, 1935). Park (1935) also described the conditions of the mine before 1916 and its continuation as well as the extraction processes that were used.

Due to the low-grade mineralization, the area was not intensely studied for several decades until Guthrie and Lesher (1989) and Stowell et al. (1989, 1996) focused on the metamorphism and gold mineralization in the Wedowee Group and the eastern Blue Ridge, which host several gold deposits including Hog Mountain. Stowell et al. (1996) reported the age of metamorphism and apparent gold mineralization at the Hog Mountain deposit at 315 ± 18 Ma based on whole rock Rb-Sr on muscovite. Metamorphic conditions were constrained using biotite and garnet geothermometer and geobarometry involving plagioclase – biotite – garnet - muscovite resulted in temperatures of 450-540 ºC and pressure of 5-7 kbar, respectively, for Hog Mountain and the surrounding schists of the Wedowee Group (Stowell et al., 1996).

These previous studies have built important context for understanding petrography and metamorphic conditions at Hog Mountain. However, the limited amount of research available on

this deposit and others in the area has left many fundamental questions unanswered regarding the genesis of mineralized veins at Hog Mountain, especially in regard to hydrothermal fluid conditions responsible for the gold mineralization, gold assemblage, Au precipitation mechanisms, the source of metals including gold, and the role of the tonalite in regard to mineral deposition.

References

Aldrich Jr, T.H., 1909, The treatment of the gold ores of Hog Mountain Alabama: American Institute of Mining Engineers, Transactions, v. 39, p. 578-583.

Cartwright, I., and Oliver, N.H.S., 2000, Metamorphic fluids and their relationship to the formation of metamorphosed and metamorphogenic ore deposits: Reviews in Economic Geology, v. 11, p. 81-96.

Cox, S.F., 2005, Coupling between deformation, fluid pressures, and fluid flow in ore-producing hydrothermal systems at depth in the crust, in Hedenquist, J.W., Thompson, J.F.H., Goldfarb, R.J., Richards, J.P., eds., Economic Geology 100th Anniversary Volume: Society of Economic Geologists, Littleton, Colorado, USA, p. 39-75.

Cox, S. F., Etheridge, M.A., and Wall, V.J., 1987, The role of fluids in syntectonic mass transport, and the localization of metamorphic vein-type ore deposits: Ore Geology Reviews, v. 2, p. 65-86.

Goldfarb, R.J., and Groves, D.I., 2015, Orogenic gold: Common or evolving fluid and metal sources through time: Lithos, v. 233, p. 2-26.

Goldfarb, R., Baker, T., Dubé, B., Groves, D.I., Hart, C.J., and Gosselin, P., 2005, Distribution, character and genesis of gold deposits in metamorphic terranes, in Hedenquist, J.W., Thompson, J.F.H., Goldfarb, R.J., Richards, J.P., eds., Economic Geology 100th Anniversary Volume: Society of Economic Geologists, Littleton, Colorado, USA, p. 407-450.

Groves, D.I., Goldfarb, R.J., Gebre-Mariam, M., Hagemann, S.G., & Robert, F., 1998, Orogenic gold deposits: a proposed classification in the context of their crustal distribution and relationship to other gold deposit types: Ore geology reviews, v. 13, p. 7-27.

Guthrie, G.M., and Lesher, C.M., 1989, Geologic setting of lode gold deposits in the northern Piedmont and Brevard zone, Alabama: Alabama Geological Survey Bulletin 136, p. 11-32.

Heinrich, C.A., and Eadington, P.J., 1986, Thermodynamic predictions of the hydrothermal chemistry of arsenic, and their significance for the paragenetic sequence of some cassiterite-arsenopyrite-base metal sulfide deposits: Economic Geology, v. 81, p. 511-529.

Jébrak, M., and Marcoux, É., 2015, Geology of mineral resources: Mineral Deposits Division of the Geological Association of Canada, 668 p.

Johnson J.W., Oelkers E.H., and Helgeson H.C., 1992, SUPCRT92: A software package for calculating the standard molal thermodynamic properties of minerals, gases, aqueous species, and reactions from 1 to 5000 bar and 0 to 1000°C: Computers & Geosciences, v. 18, p. 899-947.

Lydon, J.W., 1988, Volcanogenic massive sulfide deposits Part 2: Genetic models: Geoscience Canada, v. 15, p. 43-65.

Park, C.F., 1935, Hog Mountain gold district, Alabama: Alabama Geological Survey, Miscellaneous Paper 90, 19 p.

Pitcairn, I.K., Teagle, D.A.H., Craw, D., Olivo, G.R., Kerrich, R., and Brewer, T.S., 2006, Sources of metals and fluids in orogenic gold deposits: Insights from the Otago and Alpine Schists,

New Zealand: Economic Geology, v. 101, p. 1525-1546, doi:10.2113/gsecongeo.101.8.1525.

Pokrovski, G.S., Kokh, M.A., Guillaume, D., Borisova, A.Y., Gisquet, P., Hazemann, J.L., Lahera, E., Del Net, W., Proux, O., Testemale, D., Haigis, V., Joncheière, R., Seitsonen, A.P., Ferlat, G., Vuilleumier, R., Saitta, A.M., Boiron, M.C., and Dubessy, J., 2015, Sulfur radical species form gold deposits on Earth: Proceedings of the National Academy of Sciences, v. 112, p. 13484-13489.

Seward, T.M., 1976, The stability of chloride complexes of silver in hydrothermal solutions up to 350°C: Geochimica et Cosmochimica Acta, v. 40, p. 1329-1341.

Seward, T.M., 1984, The formation of lead(II) chloride complexes to 300°C: A spectrophotometric study: Geochimica et Cosmochimica Acta, v. 48, p. 121-134.

Seward, T.M., and Barnes, H.L., 1997, Metal transport by hydrothermal ore fluids, in Barnes, H. L., ed., Geochemistry of hydrothermal ore deposits, 3rd ed., New York, Wiley & Sons, p. 435-486.

Seward, T.M., Williams-Jones, A.E., and Migdisov, A.A., 2013, The Chemistry of Metal Transport and Deposition by Ore-Forming Hydrothermal Fluids, in Holland, H., and Turekian, K., eds., Treatise on Geochemistry, v. 13, Elsevier Ltd., p. 29-57.

Stefánsson, A., and Seward, T.M., 2004, Gold(I) complexing in aqueous sulfide solutions to 500°C at 500 bar: Geochimica et Cosmochimica Acta, v. 68, p. 4121-4143.

Stowell, H.H., Guthrie, G.M., and Lesher, C.M., 1989, Metamorphism and gold mineralization in the Wedowee Group, Goldville district, northern Piedmont, Alabama: Alabama Geological Survey Bulletin 136, p. 133-158.

Stowell, H.H., Lesher, C.M., Green, N.L., Sha, P., Guthrie, G.M., and Sinha, A.K., 1996, Metamorphism and gold mineralization in the Blue Ridge, southernmost Appalachians: Economic Geology, v.91, p. 1115-1144, doi:10.2113/gsecongeo.91.6.1115.

Stowell, H., Parker, K.O., and Madden, J., 2015, Neoacadian and Alleghanian intrusion, metamorphism, and gold mineralization in the eastern Blue Ridge: Alabama Geological Society Field Trip Guide, 52nd Annual Field Trip December 10-12, 2015, 55 p.

Tomkins, A.G., 2010, Window of metamorphic sulfur liberation in the crust: implications for gold deposit genesis: Geochimica et Cosmochimica Acta, v. 74, p 3246-3259.

Weatherley, D.K., and Henley, R.W., 2013, Flash vaporization during earthquakes evidenced by gold deposits: Nature Geoscience, v. 6, p. 294-298, doi: 10.1038/ngeo1759.

Williams-Jones, A.E., Bowell, R.J., and Migdisov, A.A., 2009, Gold in solution: Elements, v. 5, p. 281-287.

Wood, S.A., Crerar, D.A., and Borcsik, M.A., 1987, Solubility of the assemblage pyrite-pyrrhotite-magnetite-sphalerite-galena-gold-stibnite-bismuthinite-argentite-molybdenite in H_2O-NaCl-CO_2 solutions from 200º to 350ºC: Economic Geology, v. 82, p. 1864-1887.

Yardley, B.W., 2005, 100th Anniversary Special Paper: metal concentrations in crustal fluids and their relationship to ore formation: Economic Geology, v. 100, p. 613-632.

Yardley, B.W., and Cleverley, J.S., 2015, The role of metamorphic fluids in the formation of ore deposits: Geological Society, London, Special Publications, v. 393, p. 117-134.

Yardley, B.W., and Graham, J.T., 2002, The origins of salinity in metamorphic fluids: Geofluids, v. 2, p. 249-256.

Zhu, Y., An, F., and Tan, J., 2011, Geochemistry of hydrothermal gold deposits: a review: Geoscience Frontiers, v. 2, p. 367-374.

Chapter 2

Stratigraphy, Ore Mineralogy, Geochemistry, and Genesis of Gold-Bearing Quartz Veins at the Hog Mountain Tonalite, Southwestern Appalachians, USA

2.1 Introduction

Gold-mineralized quartz veins in metamorphosed lithologies have been attributed to a wide range of ore deposit types including mesothermal deposits (Lindgren et al., 1922, 1933), (Archean) lode gold deposits (Groves, 1993), orogenic gold deposits (Groves et al., 1998, 2003; Goldfarb et al., 2005), and reduced intrusion-related gold (RIRG) deposits (Thompson and Newberry, 2000; Lang and Baker, 2001; Hart, 2005, 2007; Hart and Goldfarb, 2005). In particular, Au-bearing quartz veins hosted by either metasedimentary rocks adjacent to an igneous intrusion or by tonalite to granitoid rocks have been considered controversial in their accepted genetic model and attributed to be either orogenic gold deposits or RIRG deposits (e.g., Kontoniemi and Ekdahl, 1990; Ebert et al., 2000, 2003; Goldfarb et al., 2004; Mair et al., 2006; Kontak and Kyser, 2011; Zachariáš et al., 2013, 2014). The distinction between both deposit models is difficult due to similar/overlapping features such as tectonic setting (collisional orogens), vein morphology (sheeted dikes), Au grade (relatively low), occurrence in metamorphosed terranes (sub-greenschist to upper amphibolite facies), fluid conditions (e.g., redox state, temperature, salinity, pH) or mineralogy (pyrrhotite ± pyrite ± arsenopyrite dominated with traces of Bi-Te-Au phases; Hart, 2007).

Many studies have focused on structure, whole rock geochemistry and/or fluid inclusion data to attribute igneous rock-hosted mineralized quartz veins to orogenic gold or RIRG deposits (e.g. Mair et al., 2006; Kontak & Kyser, 2011; Zachariáš et al., 2013, 2014; McDivitt et al., 2018). Less focus has been put on using detailed ore mineralogy in combination with *in situ* mineralogical and isotope data to constrain hydrothermal fluid conditions, Au precipitation mechanism, and the origin of sulfur and metals, which reveal important insights into the processes responsible for deposit formation and therefore, its assumed deposit model.

The Hog Mountain tonalite in the southernmost Appalachians, Alabama, USA, is of middle Paleozoic age (U-Pb zircon: 384 ± 32 Ma; Stowell et al., 2015) and was metamorphosed to upper greenschist to lower amphibolite facies conditions during the Pennsylvanian–Permian Alleghanian orogeny (Lesher and Guthrie, 1989; Stowell et al., 1989, 1996). The tonalite hosts moderately to steep-dipping quartz veins of simple base metal ore assemblage and trace bismuth and precious metal phases with an average Au grade of 0.14 oz/t (4.8 g/t Au) with narrow intervals of up to 2.44 oz/t Au (83.7 g/t Au; Wellborn Mining LLC, personal communication 2018). The tonalite intruded into Ordovician fine-grained, turbiditic metasedimentary rocks that also host Au-bearing quartz veins in the vicinity of Hog Mountain (Green et al., 1987; Guthrie and Lesher, 1989; Stowell et al., 1989, 1996; Smith, 2017). The gold mineralization in this region has been explained in the past by an orogenic gold model based on metamorphic and structural data (Green et al., 1987; Stowell and Lesher, 1990; Stowell et al., 1989, 1996; Saunders et al., 2013).

In this study, stratigraphic observations are combined with detailed mineralogical data (reflected light microscopy and scanned electron microscopy [SEM]) and *in situ* electron microprobe analysis (EPMA) and secondary ion mass spectrometry (SIMS) to re-evaluate the genetic model of the Au-bearing quartz veins at Hog Mountain. Moreover, major, minor and trace

element concentrations in base metal sulfides, bismuth chalcogenides and precious metal phases (EPMA) and sulfur isotopic composition of pyrrhotite, pyrite, chalcopyrite and arsenopyrite (SIMS) are applied to constrain: (1) the hydrothermal fluid conditions; (2) the dominant Au precipitation mechanism; (3) the potential sources of sulfur and metals; and (4) the genesis of mineralized quartz veins at the Hog Mountain prospect.

This work reveals the complexity in attributing a deposit model to mineralized quartz veins hosted within metamorphosed igneous rocks especially in Paleozoic orogenic belts and the importance of detailed mineralogical and geochemical investigations to decipher ore-forming fluid conditions, the Au precipitation mechanism, and sulfur and metal sources. There is a long history in gold mining within the Alabama and Georgia Appalachians, however, its exploration potential has been undervalued (Saunders et al., 2013); the results of this study impact the on-going exploration at Hog Mountain and contribute significantly to potential future exploration in the southernmost Appalachians.

2.2 Geological Setting

2.2.1 Regional Geological Setting

The Paleozoic Appalachian orogen in the eastern part of North America reaches from Newfoundland, Canada in the northeast to Alabama, U.S. in the southwest (Fig. 2.1A). It was formed during several orogenies in the Paleozoic, which resulted in the closure of the Iapetus and Rheic oceans and ultimately the formation of Pangea (e.g., van Staal, 2007; van Staal et al., 2009; Hatcher, 2010; Hibbard et al., 2010; van Staal and Barr, 2012). The orogenies include the Ordovician Taconic orogeny, the Late Devonian-Mississippian Neoacadian orogeny, and the Late

Pennsylvanian-Permian Alleghanian orogeny (Williams, 1979; Hatcher, 2002; Hatcher, 2010; Hibbard et al., 2010; van Staal and Barr, 2012). However, the tectonic evolution of the Appalachian orogen differs between the northern and southern Appalachians (Williams, 1979; Hatcher, 2010; Hibbard et al., 2007, 2010).

The southern Appalachians are divided into four paleo-geographic zones which are, from the northwest to the southeast, Valley and Ridge, Blue Ridge, Inner Piedmont (Fig. 2.1A) and the Carolinia Terrane (Hatcher, 1972). The dissected Paleozoic Appalachian Plateau borders the southern Appalachians to the northwest, whereas the Mesozoic-Cenozoic Coastal Plain borders them to the south and east forming the present-day passive continental margin (Fig. 2.1A). The Valley and Ridge, Blue Ridge and the Inner Piedmont represent Laurentia (Hatcher, 2010; Hibbard et al., 2010), whereas the Carolinia Terrane is part of peri-Gondwana and assumingly correlates with either Ganderia (Hibbard et al., 2007) or Avalonia (Nance and Murphy, 1994, 1996; Murphy and Nance, 2002; Nance et al., 2012) of the northern Appalachians. The Laurentian Paleozoic rocks of the southern Appalachians lay above Grenvillian basement (Fig. 2.1B) that formed during the Proterozoic Grenville orogeny when Laurentia is thought to have collided with South America to build Rodinia (Tohver et al., 2005; Hatcher et al., 2007).

The Valley and Ridge consists of unmetamorphosed siliciclastic rocks and limestones that were formed on the Laurentian margin during the Paleozoic (Clark, 2008). The Allegheny Front in the northwest borders the Valley and Ridge towards the Appalachian Plateau. In the southeast, a complex fault system (Talladega-Cartersville Fault System) marks the border of the Blue Ridge (Fig. 2.1A).

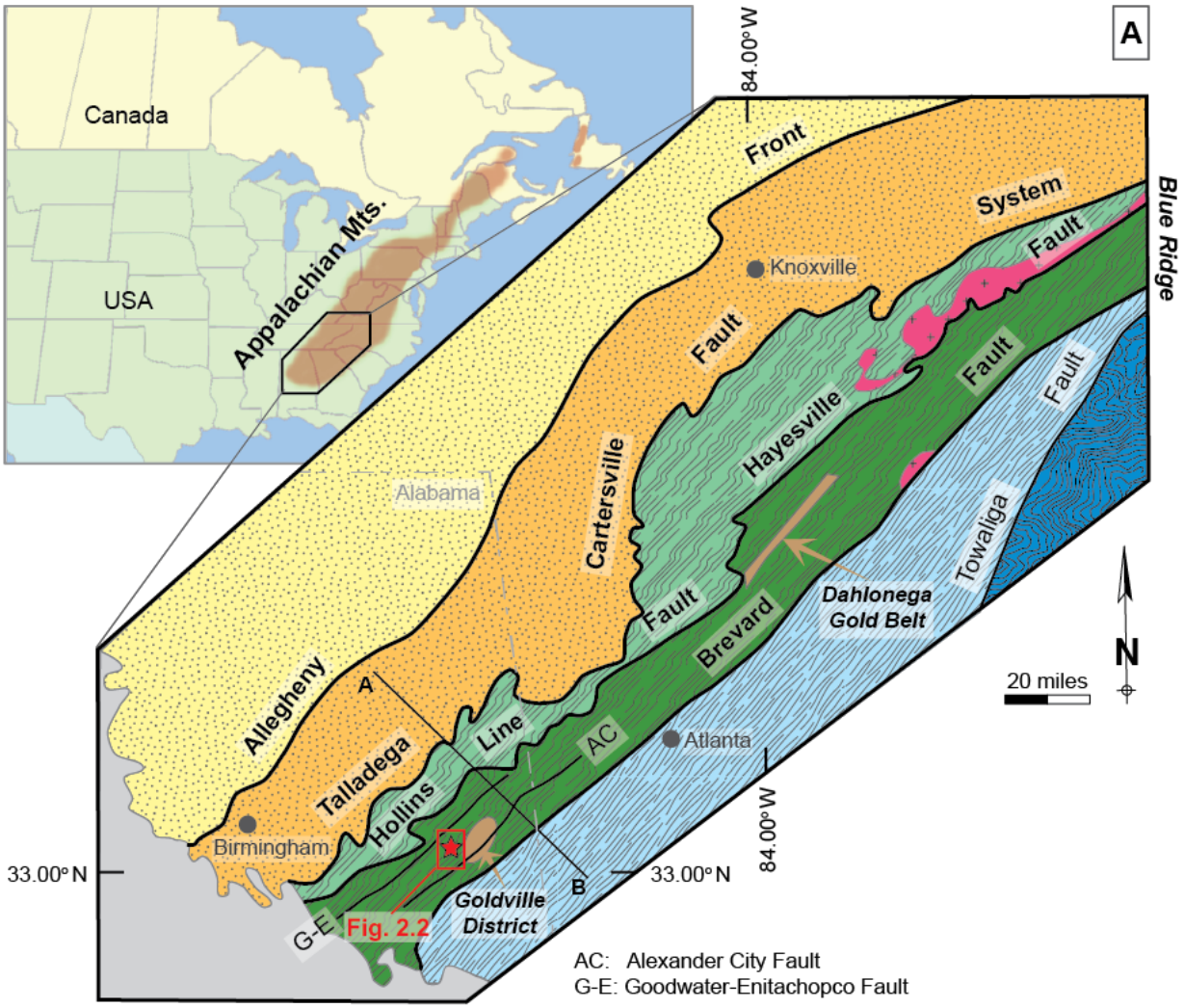

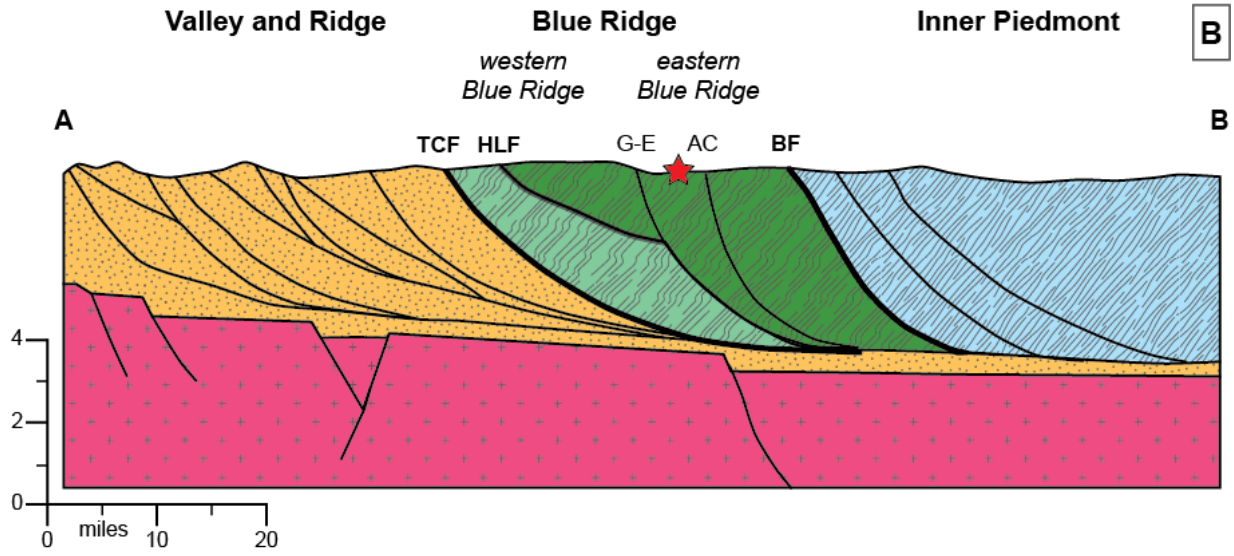

BF - Brevard Fault; HLF - Hollins Line Fault; TF - Talladega-Cartersville Fault System

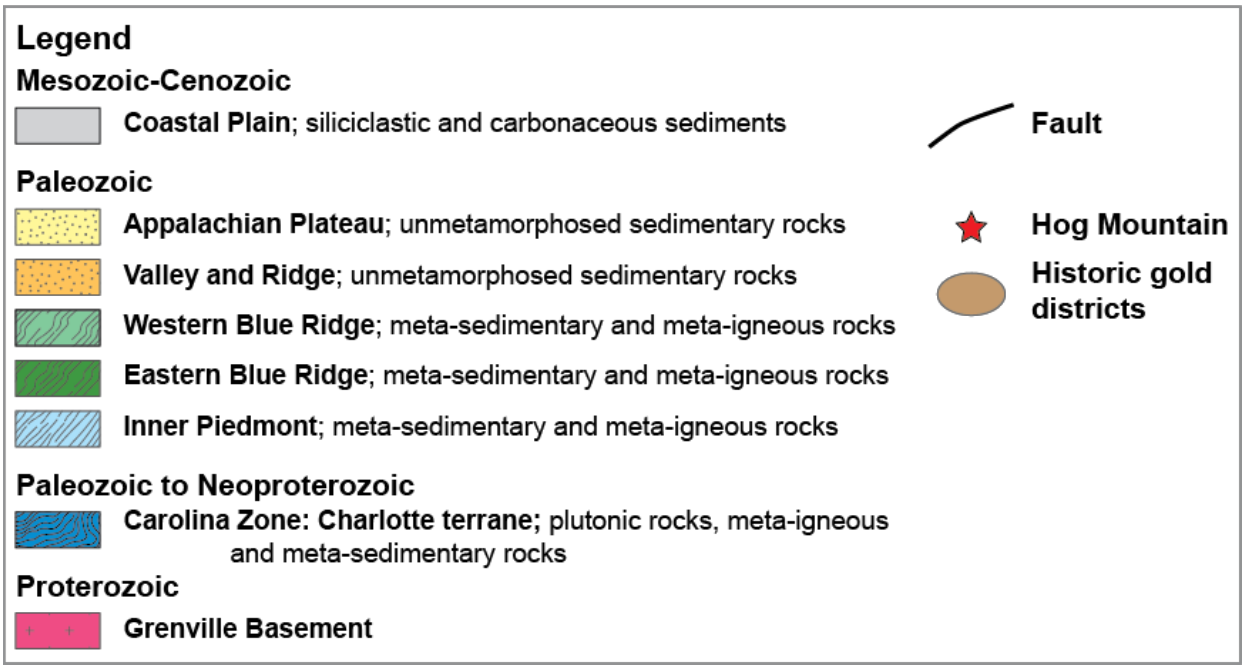

Figure 2.1. Simplified geological map and cross section of the southern Appalachians. *(previous page)* **(A)** Four geological zones of the southern Appalachians and the Coastal Plain are shown. Inlay on upper left shows location of map within Appalachians. The study area is highlighted with a red star and the detailed geological map of the area is shown in Figure 2.2. **(B)** Cross-section AB from (A) showing that allochthonous Blue Ridge and Inner Piedmont are thrusted onto Valley and Ridge and overlie Grenville basement. Location of Hog Mountain is shown as red star. (modified after Stowell et al., 1996 and Steltenpohl, 2005 and references therein)

The Blue Ridge is a complex metamorphic terrane of metavolcanic and metasedimentary rocks and is divided into the western Blue Ridge (WBR) and the eastern Blue Ridge (EBR). Episodic rifting, collision and accretion on the eastern Laurentian margin from the Neoproterozoic to the late Paleozoic formed these lithologies (Rankin, 1975; Hatcher, 1987; Thomas, 1991; Aleinikoff et al., 1995). The WBR in the southernmost Appalachians consists of Mississippian siliciclastic rocks of the Talladega Belt and Middle Ordovician felsic metavolcanic rocks of the Hillabee Greenstone (Massey and Moecher, 2005; McClellan et al., 2007; Tull et al., 2007). In contrast, the EBR is predominantly made up of Ordovician deep water pelitic to intermediate volcaniclastic rocks. Both terranes were metamorphosed durong the Alleghanian orogeny to greenschist (WBR) and amphibolite (EBR) facies. The boundary between the WBR and EBR is the Hayesville fault in the Carolinas and in Alabama and Georgia, the Hollins Line fault (Hatcher et al., 1979; Massey and Moecher, 2005). Within the Blue Ridge, several gold districts occur-the Hillabee Greenstone in the WBR and the Dahlonega gold belt of the Georgia gold belt and the Goldville district and Hog Mountain in the EBR (Fig. 2.1A; Green et al., 1987; Lesher et al., 1989; Stowell et al., 1989, 1996). The Brevard fault, to the southeast, generally corresponds to the boundary between the Blue Ridge and the Inner Piedmont. The Brevard consists of mylonitized gneisses, schists, phyllites, and amphibolites, which form several lithotectonic units. These protoliths were metamorphosed during the Neoacadian orogeny and then mylonitized during the Alleghanian orogeny (Allard and Whitney, 1994).

Both the Blue Ridge and Inner Piedmont are interpreted as allochthonous thrust sheets formed as arc or back-arc complexes during the early Paleozoic (Hibbard et al., 2007, 2010; Hatcher, 2010; Wagner et al., 2012). During the Middle Ordovician Taconic orogeny, granodioritic to tonalitic plutons intruded into the EBR terrane, and these have been interpreted to reflect

subduction beneath the the Laurentian margin (Hibbard, 2004). During the same time, bimodal volcanism is reported in the Blue Ridge and interpreted as back-arc extensional volcanism by Holm-Denoma and Ras (2010). Post-Taconic plutonism in the Late Ordovician may be related to subduction of the Piedmont beneath the Laurentian margin (Hibbard, 2004). The Neoacadian orogeny is more prominent in the northern Appalachians (Hibbard, 2004; Hibbard et al. 2010). However, plutonism recorded within the EBR is partly attributed to the Neoacadian orogeny (Miller et al., 2006). The Alleghanian orogeny is especially pronounced in the southern Appalachians up to New England and more subdued in the northern Appalachians (Hibbard, 2004) and marks the closure of the Rheic Ocean. This orogeny resulted from the continent-continent collision between Laurentia and the Gondwanan Suwannee terrane, the latter of which is buried beneath the Coastal Plain sedimentary rocks in the southeastern United States. Earlier-formed deformational structures and metamorphic features were overprinted as a result of the Alleghanian event. The Alleghanian orogeny also marks the thrusting of the Blue Ridge and Inner Piedmont onto the Valley and Ridge (Hibbard, 2004). Deformation and metamorphism during the Pennsylvanian Alleghanian orogeny resulted also in the formation of orogenic gold deposits in the Blue Ridge and Inner Piedmont (Stowell et al., 1989, 1996).

2.2.2 Geological Setting of the Study Area

The Hog Mountain tonalite is located within the EBR in the southernmost Appalachians (Figs. 2.1A, 2.2) and occurs adjacent to the Goldville district; both areas show coeval orogenic gold mineralization (Guthrie and Lesher, 1989; Stowell et al., 1989, 1996). Within the southernmost Appalachians, the EBR is stratigraphically divided from northeast to southwest into: the Ashland Supergroup (upper amphibolite mica schists), the Wedowee Group (lower

amphibolite facies phyllites and mica schists), and the Emuckfaw Group (upper amphibolite facies mica schists and amphibolites; Neathery and Reynolds, 1975; Tull, 1978). Detrital U-Pb zircon ages from metasedimentary rocks of the Emuckfaw and Wedowee Group yielded maximum deposition ages of 474 and 460 Ma, respectively (Smith, 2017). The Hog Mountain tonalite intruded into the Wedowee Group, which consists of heterogeneous metasedimentary lithologies including interlayered graphite phyllite, garnet-biotite phyllite, biotite-chlorite-sericite phyllite, garnet-biotite metagraywacke, and garnet-feldspar gneiss (Guthrie and Lesher, 1989). The Wedowee Group is separated in the northeast from the Ashland Group by the Goodwater-Enitachopca fault (G-E) and in the southeast it is separated from the Emuckfaw Group by the Alexander City fault (AC) (Figs. 2.1, 2.2; Steltenpohl, 2005).

The age of the tonalite is debatable as reported ages range from 384 ± 32 Ma (zircon U-Pb, lower intercept of 361 Ma; Stowell et al., 2015) to 333 ± 11 Ma (whole rock Rb-Sr; Green and Lesher, 1989) to 325 ± 10 Ma (whole rock Rb-Sr of moderately altered tonalite; Stowell et al., 1996). The U-Pb zircon age is likely the most robust, since it coincides with widespread felsic plutonism in the EBR during the Neoacadian and Alleghanian orogenies (Miller et al., 2006). Furthermore, Rb-Sr ages are potentially unreliable in metamorphosed rocks as those data commonly represent thermometric reset ages (Nyquist et al., 1979; Müller et al., 1999). The Hog Mountain tonalite was formed by partial melting of an intermediate igneous source (Green and Lesher, 1989).

Rocks of the Blue Ridge have been affected by multiple metamorphic (M_1, M_2) and deformational events (D_1-D_3, locally D_4-D_6) that are explained in more detail in Guthrie and Lesher (1989) and Stowell et al. (1996). Deformation events D_1-D_3 are associated with the Alleghanian orogeny and are of a compressional nature. Metamorphism occurred in the area throughout D_1 and

D_2 and occurred under greenschist to upper amphibolite facies conditions; retrograde metamorphism is associated with D_3 (Guthrie and Lesher, 1989; Stowell et al, 1989; Stowell and Lesher, 1990). The intrusion of the Hog Mountain tonalite into the phyllite of the Wedowee Group occurred prior to or during D_2 and M_2, since there is no distinct metamorphic aureole around the tonalite (Stowell et al., 1996). Stowell et al. (1989, 1996) studied the metamorphic assemblages recorded in rocks in the current study area and determined that the pressure and temperature conditions were 5.5 ± 1.1 kbar and 460 ± 50 ºC.

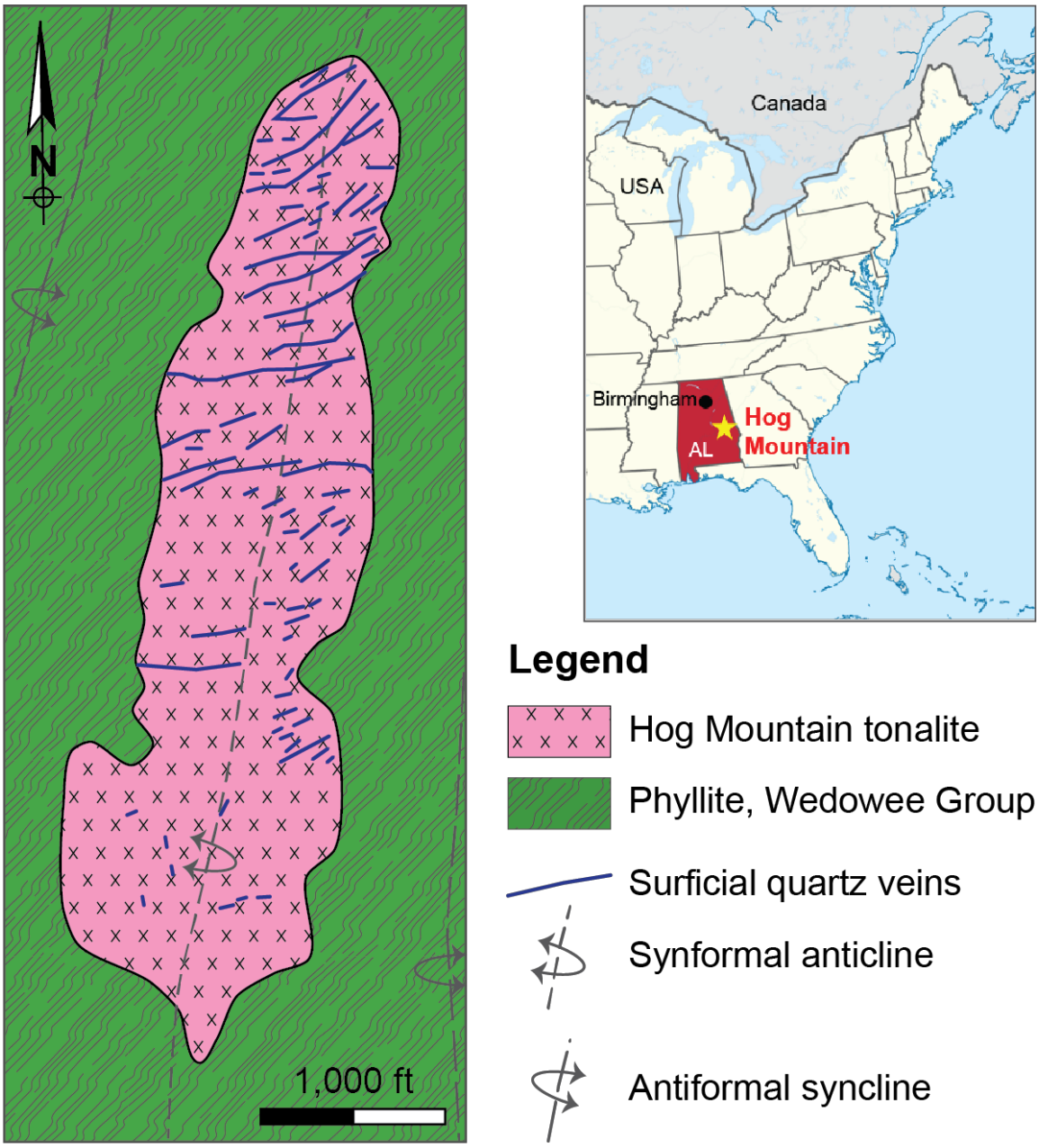

Figure 2.2. Detailed geological map of Hog Mountain. Inlay in upper right shows location of Hog Mountain within the eastern USA and Alabama (AL). (Geological map modified after Guthrie and Dean, 1989)

Vein emplacement with mineralization into the Hog Mountain tonalite and the phyllites of the Wedowee Group of the adjacent Goldville district is associated with brittle-ductile metamorphism into pre-existing shear zones post-intrusion and during syn- to post-peak metamorphism. Ar-Ar geochronology of muscovite from quartz veins and alteration zones in the tonalite provide ages of 321 Ma (Whitmore, 2018) and 294 ± 16 Ma (Stowell et al., 1996); the latter is a cooling age. These ages are interpreted to reflect the timing of retrograde metamorphism and mineralization during the end of the Alleghanian event in rocks of the EBR, which resulted in the formation of the orogenic gold deposit at Hog Mountain.

2.3 Stratigraphy

The stratigraphy at Hog Mountain was determined by detailed core logging of six drill holes (Table 2.1) that range in depth from 307 to 877 feet. The drill holes are located throughout the surficial exposure of the Hog Mountain tonalite (Fig. 2.3) and were drilled by Wellborn Mining LLC from 2014 to 2016. In Figure 2.4, a typical stratigraphic section is shown highlighting the cross-cutting relationship between quartz veins, the host tonalite, and the phyllites into which the tonalite intruded. Additional stratigraphic cross-sections can be found in Appendix A.

The tonalite is fine to moderately phaneritic with a dominantly quartz – plagioclase – biotite assemblage and commonly finely disseminated pyrite (Fig. 2.5A; Park, 1935; Green and Lesher, 1989; Stowell et al., 1996) and ranges in thickness from about 100 feet at the northern end to about 1,000 feet at the southern end (Fig. 2.3). Within the tonalite, quartz veins frequently occur and cross-cut the tonalite at a high angle relative to the core axis. Field observations show that the

veins dip between 45 to 75º with an average of 60º to the northwest (Park, 1935; M. Whitney, personal communication 2019).

Table 2.1. Drill holes used for stratigraphic observations with their length, coordinates, elevation, and range of Au grade. Coordinates are given in US feet and the system used is UTM-NAD 83, Zone 16N.

Drill hole #	Length [ft]	Easting [ft]	Northing [ft]	Elevation [ft]	Maximum Au grade [oz/t]
HM-058	600.2	1992353	12007476	600.2	0.36
HM-071	430.0	1992327	12007889	878.4	1.57
HM-083	462.0	1992404	12008149	951.2	0.23
HM-114	876.7	1992511	12006374	879.6	2.21
HM-122	843.0	1992555	12006834	913.9	0.45
HM-130	307.0	1992463	12008618	1048.8	2.44

Tonalite intruded into phyllite of the Wedowee Group and a sharp albeit irregular contact between the two units is observed near the bottom of each drill hole (Figs. 2.3, 2.4, and 2.5B). Phyllite at Hog Mountain is very fine-grained, dark and shows no porphyroblasts and porphyrocrysts.

Previous studies by Stowell et al. (1989, 1996) identified three vein types that occur both in the Goldville district and Hog Mountain. These vein classes are: (1) mono-mineralic quartz veins; (2) quartz ± plagioclase ± chlorite ± carbonate ± sulfide ± gold veins; and (3) calcite ± quartz ± sulfide ± gold veins. The dominant occurrence of vein classes 1 and 2 and minor composite veins of classes 2 and 3 within the studied drill holes support the observations of Stowell et al. (1989, 1996). The veins show no macroscopic crack-seal or ribbon texture and the quartz is white to light grey with a sugary appearance due to recrystallization. Other macroscopic quartz textures including blocky, comb, vuggy or colloform quartz are not observed. Veins range in width from less than a tenth of an inch to over 15 feet within drill core. (Fig. 2.4).

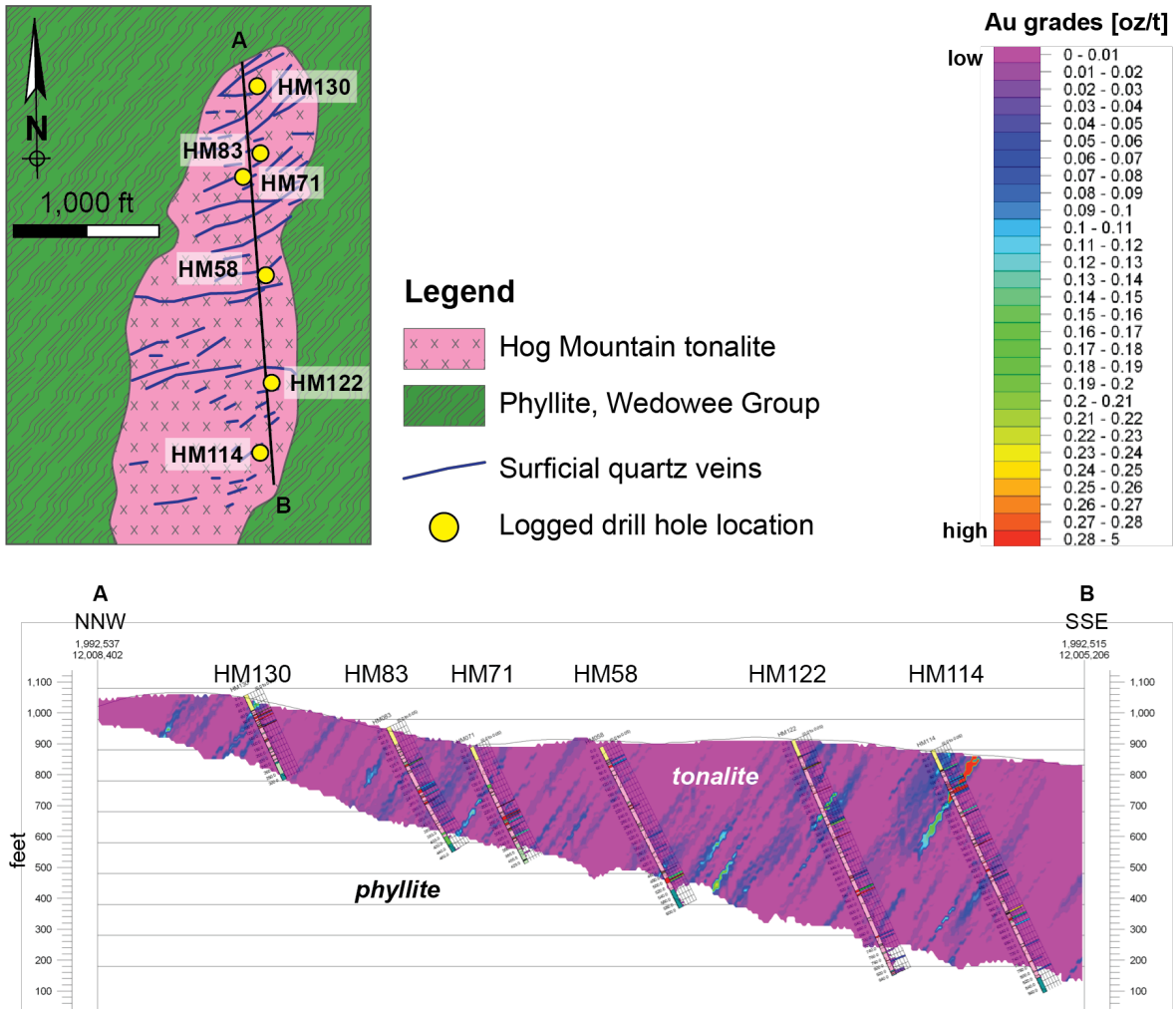

Figure 2.3. Drill hole locations and Au grades of logged drill holes. The locations of the logged drill holes are shown in the geologic map on the top right. A cross section (AB) through the logged drill holes is shown on the bottom highlighting the Au grades (legend on top right). Mineralized quartz veins with steep dips to the NW are indicated by bluish colors. (Geologic map modified after Guthrie and Dean, 1989)

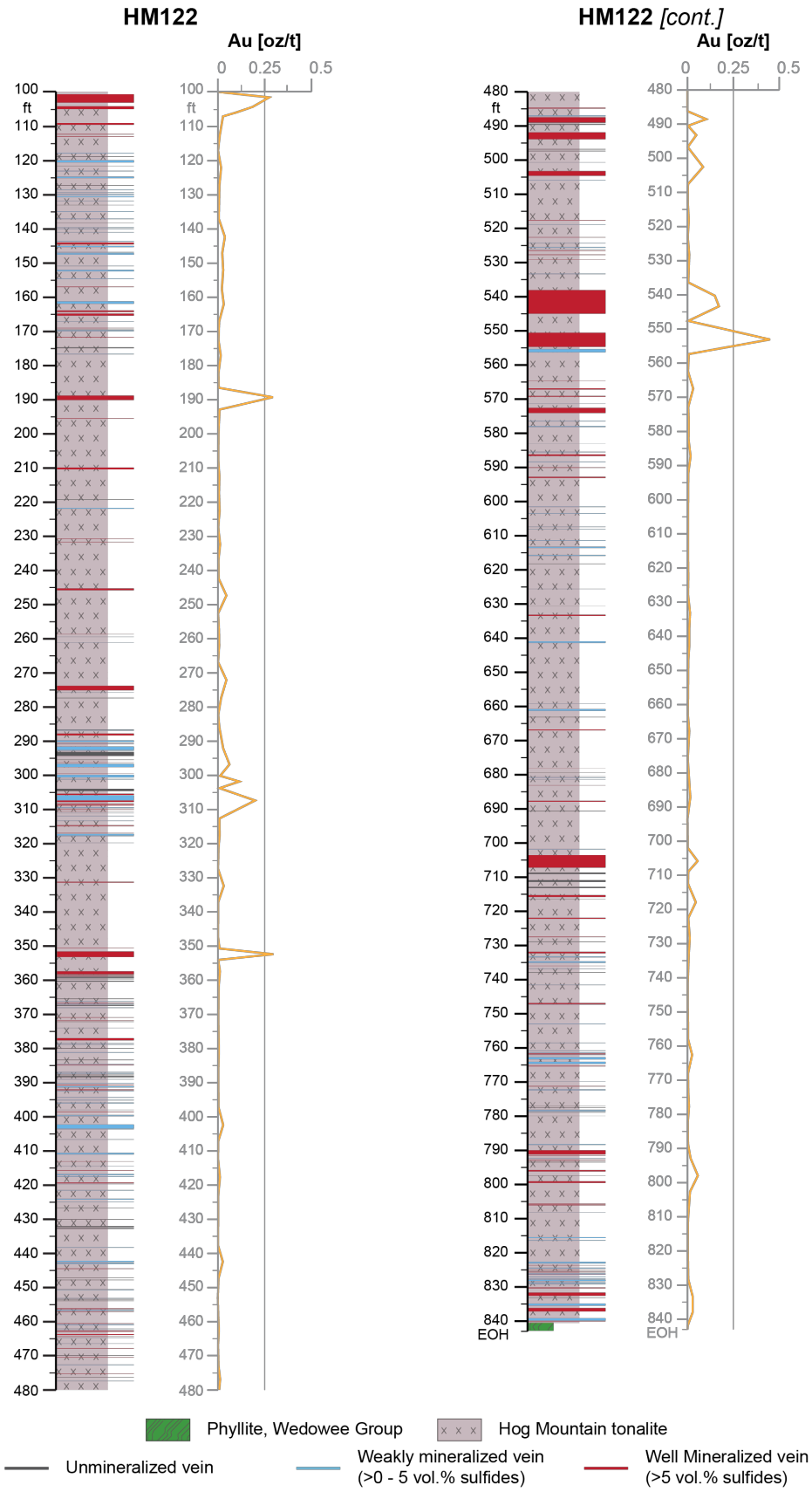
HM122
Au [oz/t]
0
0.25
0.5
100
ft
110
120
130
140
150
160
170
180
190
200
210
220
230
240
250
260
270
280
290
300
310
320
330
340
350
360
370
380
390
400
410
420
430
440
450
460
470
480
HM122 [cont.]
Au [oz/t]
0
0.25
0.5
480
ft
490
500
510
520
530
540
550
560
570
580
590
600
610
620
630
640
650
660
670
680
690
700
710
720
730
740
750
760
770
780
790
800
810
820
830
840
EOH
Phyllite, Wedowee Group
Hog Mountain tonalite
Unmineralized vein
Weakly mineralized vein
(>0 - 5 vol.% sulfides)
Well Mineralized vein
(>5 vol.% sulfides)

Figure 2.4. **Stratigraphic section of HM122 showing the relationship between tonalite, cross-cutting veins, and older phyllite of the Wedowee Group and related Au grades down hole.** *(previous page)* Veins show different degrees of mineralization (unmineralized, weakly mineralized and well mineralized) and dominantly contain quartz with traces of silicates ± calcite ± sulfides (vein class 2 after Stowell et al., 1989, 1996) or are mono-mineralic (vein class 1 after Stowell et al., 1989, 1996). Composite veins of quartz and carbonate ± silicates ± sulfides (vein classes 2 and 3 after Stowell et al., 1989, 1996) are rare. The first 100 ft are strongly weathered to saprolite. **Abbreviations:** EOH – end of hole, ft – feet, HM – Hog Mountain

The veins have varying degrees of sulfide mineralization ranging from unmineralized (0 vol% sulfides) to weakly mineralized (> 0-5 vol% sulfides; Fig. 2.5C, D) to well mineralized (> 5 vol% sulfides) veins (Fig. 2.5E, F). The sulfide mineralization is dominated by pyrrhotite ± pyrite with traces of chalcopyrite ± sphalerite ± arsenopyrite ± galena. There is no correlation between the degree of mineralization and depth as mineralization is continuous over long vertical distances. Veins typically have a chlorite – sericite ± carbonate ± pyrite alteration envelope that ranges in width from less than half an inch to several inches and shows no correlation to vein width or degree of mineralization (Fig. 2.5D-H). In addition to quartz veins, thin veinlets of arsenopyrite ± chalcopyrite ± pyrite ± pyrrhotite occasionally cross-cut the tonalite at a high angle to the core axis (Fig. 2.5G). These veinlets range in width from less than one inch to four inches and have alteration envelopes with assemblages similar to what is observed around the mineralized quartz veins. Due to their sparseness, they are not separately reported in the stratigraphic columns (Fig. 2.4 and Appendix A). Rarely, mineralization of sphalerite – chalcopyrite – arsenopyrite – galena is observed on the contact between quartz veins and the tonalite (Fig. 2.5H), which is weakly altered in the immediate vicinity of the mineralization. Although quartz veins continue into the phyllite, drilling is commonly ceased at the tonalite-phyllite contact since the veins lack significant mineralization and the highest Au grades are within the tonalite (M. Whitney, personal communication 2018).

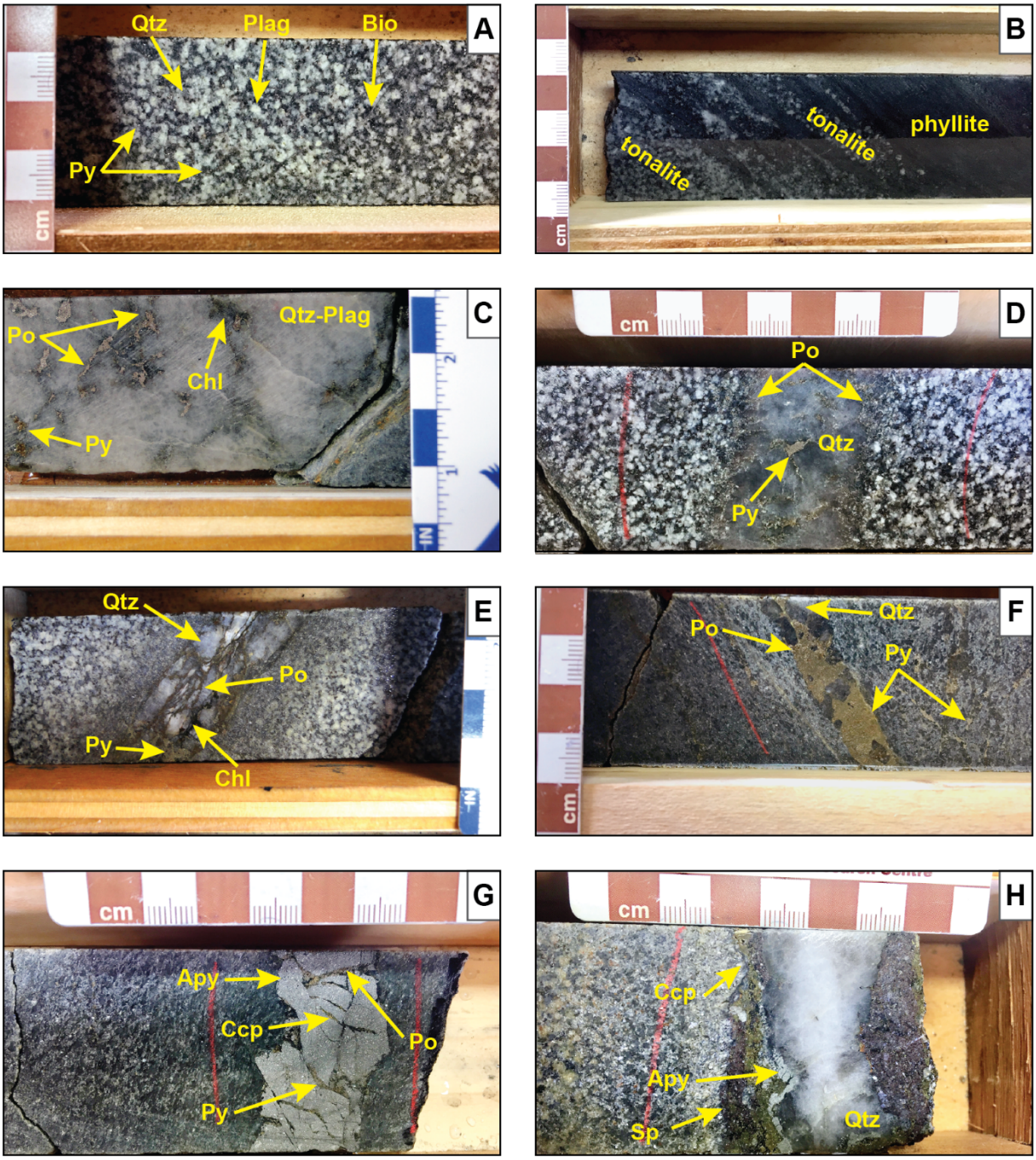
A
Qtz
Plag
Bio
Py
cm
B
tonalite
tonalite
phyllite
cm
C
Qtz-Plag
Po
Chl
Py
D
cm
Po
Qtz
Py
E
Qtz
Po
Py
Chl
F
Qtz
Po
Py
cm
G
cm
Apy
Ccp
Po
Py
H
cm
Ccp
Apy
Sp
Qtz

Figure 2.5. Typical lithologies at Hog Mountain. *(previous page)* **(A)** Phaneritic, weakly altered tonalite with quartz – plagioclase – biotite assemblage and disseminated pyrite. **(B)** Sharp but irregular contact between tonalite and dark, very fine-grained phyllite. **(C)** Weakly mineralized quartz – chlorite vein with disseminated pyrite – pyrrhotite. **(D)** Thin, weakly mineralized vein with coarse disseminated pyrite and small pyrrhotite on vein contact to tonalite. The vein has no significant alteration envelope. **(E)** Thin, well mineralized quartz vein with thin pyrite – pyrrhotite stringer that give the vein a brecciated appearance. Small chlorite – sericite alteration halo occurs around the vein. **(F)** Well mineralized quartz vein with dominant massive pyrite and minor pyrrhotite. Strong alteration halo with disseminated pyrite occurs around the vein. **(G)** Massive arsenopyrite with interstitial pyrite – pyrrhotite – chalcopyrite occurs within tonalite. A thin alteration halo occurs around the vein. **(H)** Arsenopyrite – chalcopyrite – sphalerite mineralization on contact between quartz vein and tonalite. **Abbreviations:** Apy – arsenopyrite, Bio – biotite, Ccp – chalcopyrite, Chl – chlorite, Plag – plagioclase, Po – pyrrhotite, Py – pyrite Qtz – quartz, Sp – sphalerite.

2.4 Ore Mineralogy and Paragenesis

Ore mineralization is most prominent within quartz ± silicate ± calcite veins, but occasionally occurs as disseminations within the tonalite. The mineralization is dominated by base metal sulfides (Fig. 2.6) and traces of Bi-, Te-, and Au-phases (Fig. 2.7). Pyrrhotite is the major ore phase with minor to traces of pyrite ± arsenopyrite and traces of chalcopyrite ± sphalerite ± galena ± Bi-phases ± tellurides ± Au-phases. Trace Fe ± Ti-oxides also occur. Microscopic observations on 50 thin sections from six drill holes are presented in Appendix B.

Pyrrhotite [$Fe_{(1-x)}S$ with x = 0 to 0.2] occurs as coarse anhedral grains between quartz (Fig. 2.6A, B, D), as small disseminated grains within quartz (Fig. 2.6A, F), or less commonly as small inclusions within pyrite (Fig. 2.6C) or chalcopyrite (Fig. 2.7A). Pyrrhotite dominantly occurs with pyrite and chalcopyrite (Fig. 2.6A, D) but is also observed with arsenopyrite (Fig. 2.6B). Inclusions of sphalerite, chalcopyrite or Bi-phases can occur within pyrrhotite. Pyrrhotite is sometimes replaced by euhedral pyrite near the contact with quartz or chlorite (Fig2.6D). On pyrrhotite margins, Bi and precious metal phases can occur.

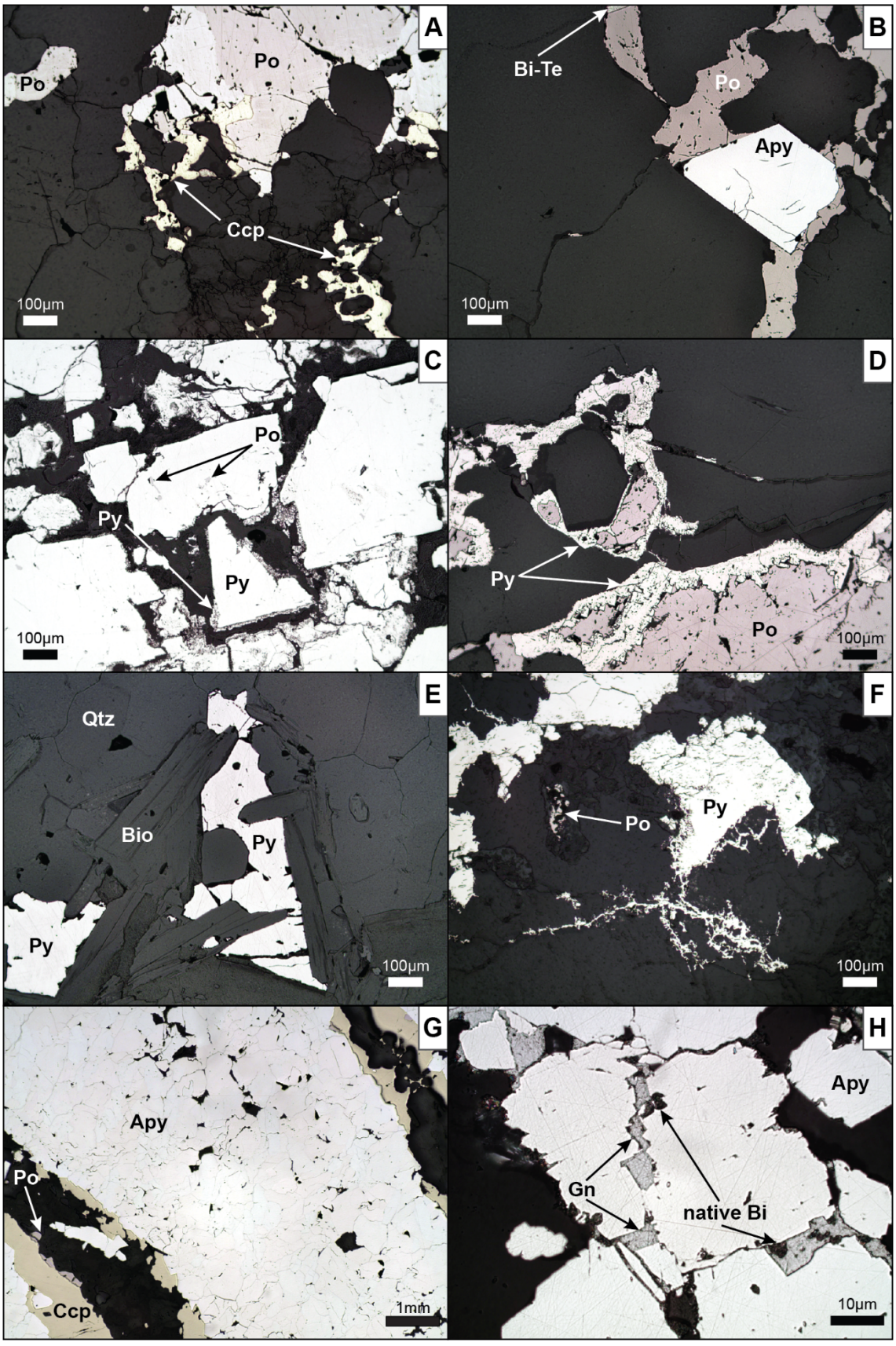
A
Po
Po
Ccp
100μm
B
Bi-Te
Po
Apy
100μm
C
Po
Py
Py
100μm
D
Py
Po
100μm
E
Qtz
Bio
Py
Py
100μm
F
Po
Py
100μm
G
Apy
Po
Ccp
1mm
H
Apy
Gn
native Bi
10μm

Figure 2.6. Reflected light images of base metal sulfides at Hog Mountain. *(previous page)* (**A)** Pyrrhotite with amoeboid chalcopyrite on margins in quartz vein. Disseminated pyrrhotite and chalcopyrite occur interstitially between quartz grains. **(B)** Anhedral pyrrhotite between quartz grains and with arsenopyrite and bismuth telluride in quartz vein. **(C)** Subhedral, partly cataclastic pyrite with pyrrhotite inclusions and fine-grained pyrite rim in quartz vein. **(D)** Partial replacement of pyrrhotite by pyrite in quartz vein. **(E)** Disseminated pyrite in tonalite partially overprinted by biotite. **(F)** Disseminated pyrite and pyrrhotite in quartz vein. Pyrite occurs as subhedral, partly recrystallized grains, and detrital grains interstitial between quartz. **(G)** Massive, anhedral, partly recrystallized arsenopyrite with marginal chalcopyrite and pyrrhotite. **(H)** Arsenopyrite with interstitial galena in quartz vein. Native bismuth is in close spatial relation to galena. **Abbreviations:** Apy – arsenopyrite, Bio – biotite, Bi-Te – bismuth telluride, Ccp – chalcopyrite, Gn – galena, native Bi – native bismuth, Qtz – quartz, Po – pyrrhotite, Py – pyrite.

Pyrite [FeS_2] is a minor to trace phase, occurs in both the tonalite (Fig. 2.6E) and veins (Fig. 2.6C, D, F), but can also be absent. Grains are commonly small and subhedral to euherdral (Fig. 2.6C-F), although recrystallized (Fig. 2.6C) and detrital (Fig. 2.6F) grains are observed within veins. Pyrite is most commonly associated with pyrrhotite ± chalcopyrite ± arsenopyrite.

Arsenopyrite [FeAsS] is either a major phase within small, arsenopyrite-dominated veinlets in tonalite (Fig. 2.5G) or a trace phase in quartz veins with other base metal sulfides. In the former case, partially recrystallized arsenopyrite is coarse, massive and can be cross-cut by pyrrhotite ± chalcopyrite veinlets (Figs. 2.5G and 2.6G). Within quartz veins, arsenopyrite is subhedral to anhedral, can be cataclastic, and occurs with pyrrhotite (Fig. 2.6B) or galena (Fig. 2.6H).

Chalcopyrite [$CuFeS_2$] is a trace phase that occurs as small, anhedral grains commonly on pyrrhotite margins and as disseminated grains in quartz (Fig. 2.6A). Rarely, chalcopyrite disease is observed within sphalerite.

Similar to chalcopyrite and arsenopyrite, sphalerite [ZnS] is a trace phase in veins or absent. Small, anhedral grains within pyrrhotite are most common, although coarse, massive sphalerite

grains with weak ‘chalcopyrite disease’ and inclusions of pyrite ± pyrrhotite are observed on quartz – tonalite contacts (Fig. 2.5H).

Among base metal sulfides, galena [PbS] is least abundant and occurs with sphalerite (Fig. 2.7B) on quartz – tonalite contacts as small anhedral grains, interstitial between arsenopyrite, as inclusions in sphalerite or pyrite, and occasionally with native bismuth and hessite (Figs. 2.6H, 2.7H).

In addition to base metal sulfides, the ore assemblage at Hog Mountain includes a variety of trace Bi-, Te- and precious metal phases (Figs. 2.7 and 2.8). In order of decreasing abundance, they are: bismuth tellurides (hedleyite [Bi_7Te_3], ‘unnamed bismuth telluride phase’ [Bi_3Te]), native bismuth [Bi], bismuthinite [Bi_2S_3], electrum [Au,Ag], native gold [Au], maldonite [Au_2Bi], and hessite [Ag_2Te]. Bismuth phases including bismuth tellurides commonly occur with gold phases (Figs. 2.7A, D, E, and F, 2.8B-D). In contrast, hessite is only observed when galena and native bismuth occur together (Fig. 2.7H).

Bismuth phases (bismuth tellurides > native bismuth > bismuthinite) are small, sub-angular to sub-roundish and occur commonly together on pyrrhotite and lesser chalcopyrite margins (Fig. 2.7A, C, D, G), in or between quartz grains (Fig. 2.7A, C, E, F), less commonly as inclusions in pyrrhotite (Figs. 2.7A, 2.8E) or rarely with galena (Fig. 2.7B, H). Intergrowth textures between native bismuth, bismuthinite and/or bismuth tellurides are relatively common especially in samples with Au grades above average (Fig. 2.8A-E). Additionally, bismuthinite can exhibit a rim of native bismuth (Figs. 2.7A, C, F, 2.8A). Trails of native bismuth and bismuth tellurides droplets are present in some quartz grains, along quartz grain boundaries (Fig. 2.7H) and within very fine cracks in pyrrhotite (Fig. 2.8E).

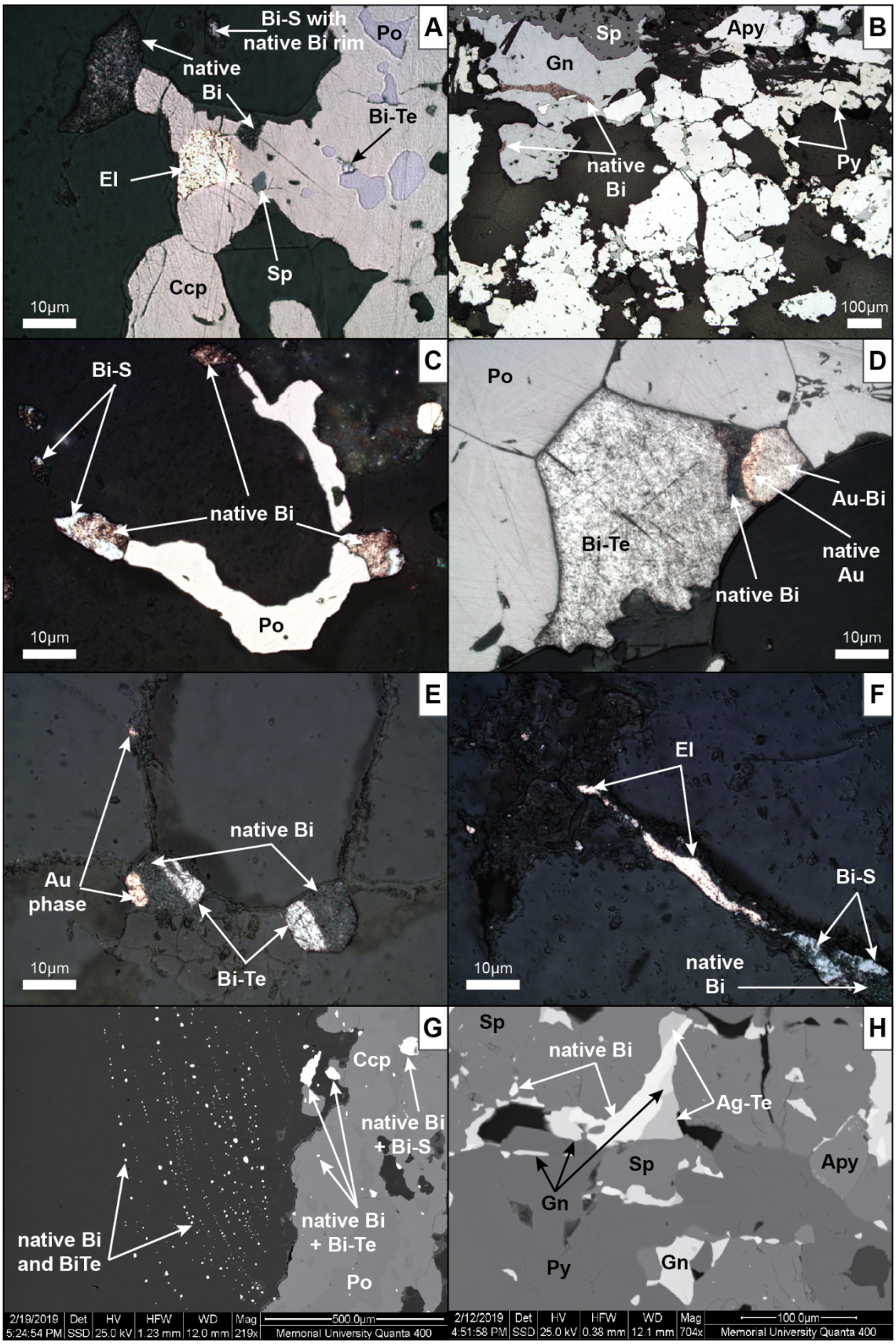
A
Bi-S with
native Bi rim
Po
native
Bi
Bi-Te
El
Sp
Ccp
10µm
B
Sp
Apy
Gn
native
Bi
Py
100µm
C
Bi-S
native Bi
Po
10µm
D
Po
Au-Bi
Bi-Te
native
Au
native Bi
10µm
E
native Bi
Au
phase
10µm
Bi-Te
F
El
Bi-S
10µm
native
Bi
G
Ccp
native Bi
+ Bi-S
native Bi
+ Bi-Te
native Bi
and BiTe
Po
2/19/2019 | Det | HV | HFW | WD | Mag | 500.0µm
5:24:54 PM | SSD | 25.0 kV | 1.23 mm | 12.0 mm | 219x | Memorial University Quanta 400
H
Sp
native Bi
Ag-Te
Sp
Apy
Gn
Py
Gn
2/12/2019 | Det | HV | HFW | WD | Mag | 100.0µm
4:51:58 PM | SSD | 25.0 kV | 0.38 mm | 12.1 mm | 704x | Memorial University Quanta 400

Figure 2.7. Reflected light and backscattered electron images of Bi, Te, and precious metal assemblages at Hog Mountain. *(previous page)* **(A)** Chalcopyrite with inclusions of pyrrhotite, sphalerite, bismuth tellurides and marginal electrum and native bismuth in quartz vein. Disseminated bismuthinite with native bismuth rim. **(B)** Galena with native bismuth and can have inclusions of arsenopyrite or occurs interstitial between arsenopyrite grains. Arsenopyrite has marginal pyrite. Sphalerite occurs adjacent to galena. **(C)** Pyrrhotite with native bismuth rimmed by bismuthinite in quartz vein. Small disseminated grains of native bismuth ± bismuthinite occur also in quartz vein. **(D)** Bismuth tellurides with native bismuth, native gold, and maldonite on margins of recrystallized pyrite in quartz vein. Semi-quantitative elemental map is shown in Figure 2.8D. **(E)** Sub-roundish grains of native Au and electrum with native bismuth and bismuth tellurides interstitial between quartz grains in quartz vein. **(F)** Electrum veinlet with marginal maldonite and native bismuth between quartz grains within quartz vein. **(G)** Trails of droplets of native bismuth and bismuth tellurides within quartz grains and along quartz grain boundaries. Bismuth phases (native bismuth, bismuth tellurides, bismuthinite) on chalcopyrite margins and as inclusions in both chalcopyrite and pyrrhotite. **(H)** Hessite with native bismuth and galena in sphalerite. Native bismuth also occurs as inclusions in sphalerite and galena and along sulfide contacts. **Abbreviations:** Ag-Te – hessite, Apy – arsenopyrite, Au – native gold, Au-Bi – maldonite, Au phase – native gold or electrum, Bi – native bismuth, Bi-S – bismuthinite, Bi-Te – bismuth tellurides (hedleyite or unnamed Bi_3Te), Ccp – chalcopyrite, El – electrum, Gn – galena, Sp – sphalerite, Po – pyrrhotite, Py – pyrite.

Gold phases (native gold ≈ electrum > maldonite) are spatially closely associated with Bi-phases (Figs. 2.7A, D, E, F, 2.8B-E), in particular native bismuth and bismuth tellurides (Fig. 2.8B-E). They occur either on pyrrhotite margins (Fig. 2.7A, C, D, E), between quartz grains as sub-roundish aggregates or veinlets with Bi-phases (Figs. 2.7E, F, 2.8C), as inclusions or very small droplets in pyrrhotite (Fig. 2.8B, E), or rarely in native bismuth (Fig. 2.8B).

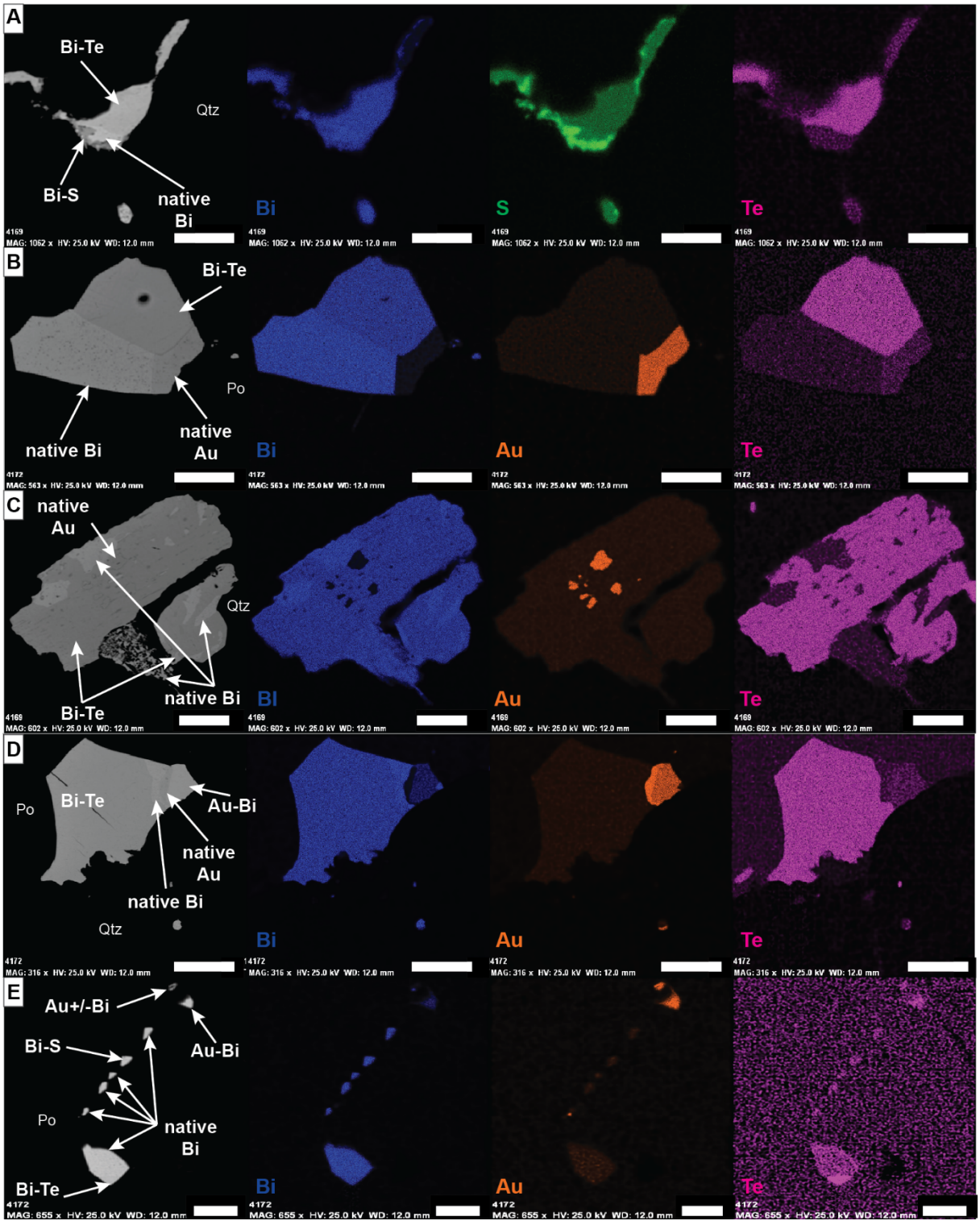
A
Bi-Te
Qtz
Bi-S
native Bi
Bi
S
Te
B
Bi-Te
Po
native Bi
native Au
Bi
Au
Te
C
native Au
Qtz
native Bi
Bi-Te
Bi
Au
Te
D
Po
Bi-Te
Au-Bi
native Au
native Bi
Qtz
Bi
Au
Te
E
Au+/-Bi
Au-Bi
Bi-S
Po
native Bi
Bi-Te
Bi
Au
Te

Figure 2.8. Backscattered electron (BSE) images (greyscale) and maps (color) of selected elements for bismuth and gold assemblages. *(previous page)* **(A)** Intergrowth of bismuth telluride (hedleyite or unnamed Bi_3Te) with native bismuth and bismuthinite in quartz. Elemental maps of bismuth (blue), sulfur (green), and tellurium (magenta) highlight individual phases. White scale bars are 20 μm. **(B)** Agglomerate of native bismuth with native gold and bismuth telluride (hedleyite or unnamed Bi_3Te) in pyrrhotite. Elemental maps of bismuth (blue), gold (orange), and tellurium (magenta) highlight individual phases. White scale bars are 50 μm. **(C)** Intergrowth of bismuth tellurides (hedleyite or unnamed Bi_3Te) with native bismuth and inclusions of native gold in quartz. Native bismuth tellurides exists as worm-like intergrowths with quartz in lower half of image. Elemental maps of bismuth (blue), gold (orange), and tellurium (magenta) highlight individual phases. White scale bars are 50 μm. **(D)** Figure 2.7D. Bismuth telluride (hedleyite or unnamed Bi_3Te) occurs together with – from left to right – native bismuth, native gold and maldonite. Elemental maps of bismuth (blue), gold (orange), and tellurium (magenta) highlight individual phases. White scale bars are 100 μm. **(E)** Individual droplets of native gold, maldonite, bismuthinite, native bismuth and one aggregated droplet of bismuth telluride (hedleyite or unnamed Bi_3Te) with native bismuth in pyrrhotite along very fine cracks. Elemental maps of bismuth (blue), gold (orange), and tellurium (magenta) highlight individual phases. White scale bars are 30 μm. **Abbreviations:** Au-Bi – maldonite, Au±Bi – native gold with or without bismuth, Bi-S – bismuthinite, Bi-Te – bismuth telluride (hedleyite or unnamed Bi_3Te), native Au – native gold, native Bi – native bismuth, Po – pyrrhotite, Qtz – quartz. Conditions for BSE images and elemental maps are described in 2.5 Analytical Methods.

The mineral paragenesis at Hog Mountain is summarised in Figure 2.9. Ore mineralization of the different phases is continuous. Although, not all observed ore mineral phases in the mineralized quartz veins precipitated at the same time.

Among base metal sulfides, arsenopyrite deposited first or coeval with pyrrhotite from highly reduced fluids (Heinrich and Eadington, 1986) and chalcopyrite followed by pyrite. However, pyrite might be, at least in part, the product of retrograde growth due to pyrrhotite breakdown and subsequent replacement (Craig and Vokes, 1993). Sphalerite and galena are late stage. The precipitation of sphalerite occurred coeval with ongoing chalcopyrite precipitation that is documented in minute, randomly oriented droplets of chalcopyrite within sphalerite (‘chalcopyrite disease’, Fig. 2.7B; Barton Jr. and Bethke, 1987).

Bismuth and Au-bearing phases deposited coeval with the first base metals, in particular pyrrhotite. Bismuth phase precipitation continued throughout the formation of the mineralized veins at Hog Mountain since they are spatially associated with early and late stage base metal sulfides (Fig. 2.7). In contrast, precipitation of Au-bearing phases ceased before galena precipitated, since no close spatial relationship is observed.

Retrograde and/or epigenetic processes affected both base metal sulfides and Bi- and Au-bearing phases. Cataclastic cracks and recrystallization in some pyrite and arsenopyrite grains is observed (Fig. 2.6B, C, F). This is in accordance with brittle-ductile behavior of pyrite that behaves brittle at temperatures below 400 ºC under greenschist metamorphic conditions (Marshall and Gilligan, 1987 and references therein). Liberation and/or remobilization of Bi- and Au-phases by low-grade, retrograde metamorphism and/or later deformation occurred and will be discussed below.

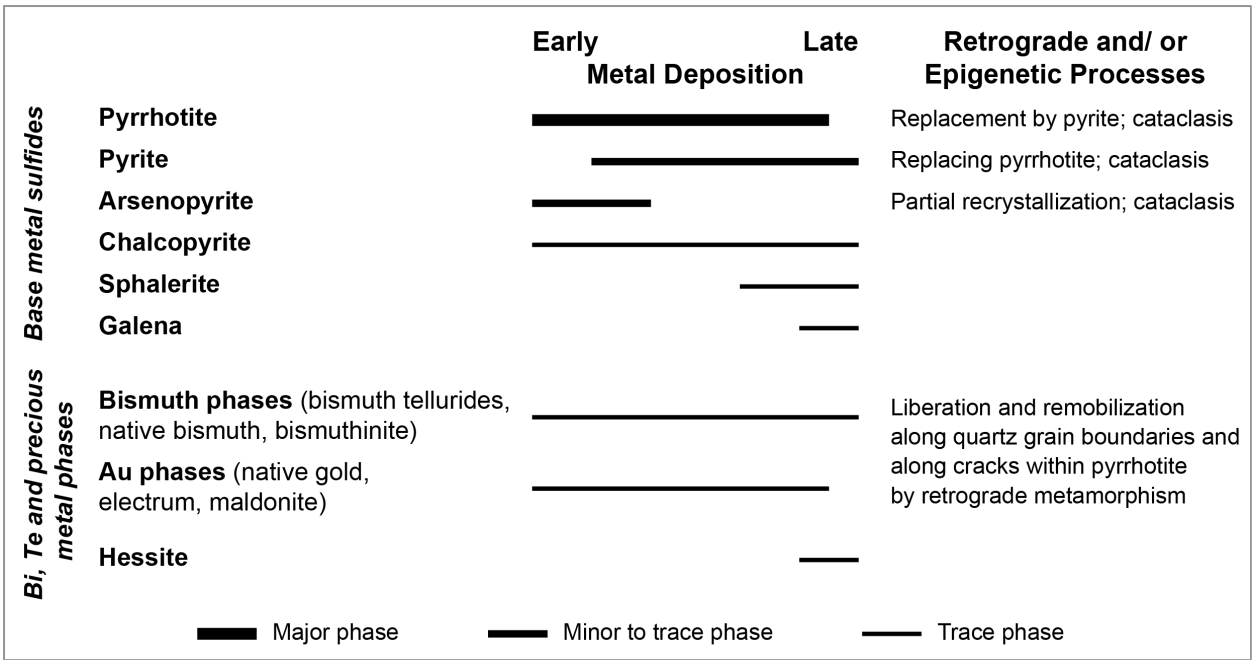

Figure 2.9. Paragenetic chart for metal deposition at Hog Mountain. Retrograde and/or epigenetic processes affecting ore minerals are listed on the left and are based on textural observations.

2.5 Analytical Methods

Scanning electron microscopy (SEM), electron microprobe analysis (EMPA), and secondary ion mass spectrometry (SIMS) were conducted at the Department of Geosciences and the Bruneau Innovation Center at Memorial University of Newfoundland (MUN), St. John's, Canada in February 2019.

Back scattered electron (BSE) images and elemental maps were obtained using a FEI Quanta 400 scanning electron microscope (SEM) at the Microanalysis Facility of the CREAIT Network, Bruneau Innovation Center at MUN. The FEI Quanta 400 is equipped with a Bruker silicon drift energy dispersive X-ray (EDX) detector. This system allows quick semi-quantitative detection of a variety of elements (e.g., Ag, As, Au, Bi, Cu, Fe, Pb, S, Si, Te and Zn), produces element maps, and shows EDX spectra for numerous phases in order to corroborate mineral composition and textures previously documented using reflected light microscopy. The FEI Quanta 400 was run in high vacuum mode at a beam energy of 25 keV and a beam current of 10 nA. A scintillator detected the Kα emission lines of Si, S, Fe, Cu, Zn, and As, and the Lα emission lines of Ag, Au, Bi, Te, and Pb. In order to detect possible interferences (e.g., Zn Kβ interferes with Au Lα; S Kα interferes with Bi Mα), the mineral of interest was scanned and alternative emission lines were then used to check for any elemental overlaps. If an overlap occurred, the alternate, interference-free emission line was used for semi-quantitative EDX scans. EDX scans allow for the detection of individual elements within minerals but the elemental maps produced via EDX do not provide specific elemental concentrations; instead, they are based on raw counts per second. However, as the measured intensity for each element is proportional to its concentration, this approach is semi-quantitative.

Electron microprobe analysis was performed on sulfides (pyrrhotite, pyrite, chalcopyrite, arsenopyrite, sphalerite, galena), Bi±Te phases (native bismuth, hedleyite, 'unnamed bismuth telluride phase', hessite), precious metals (electrum), and silicates (quartz) at the Department of Geosciences, MUN. A JEOL JXA-8230 Superprobe with five tunable wavelength dispersive spectrometers was used to determine major, minor and trace element compositions of the analyzed mineral phases. In total, 19 elements (Ag, As, Au, Bi, Cd, Co, Cr, Cu, Fe, Hg, Ni, Pb, S, Sb, Se, Te, Ti, V, Zn) were analyzed on six samples that are representative of the Hog Mountain ore assemblage. The wavelength dispersive probe is equipped with a W filament, Be window, and Faraday cup; measurements were run at 25 keV with a 20 nA current at a beam diameter of 1 µm and takeoff angle of 40º. The measured elements were either analyzed by a LIF crystal (Zn Kα, Fe Kα, Cr Kα), PETL crystal (Sb Lα, Cd Lα, Ag Lα, Hg Mα, Te Lα, Bi Mα, Pb Mα, S Kα, Au Mα), TAP crystal (As Lα, Se Lα), or LIFH crystal (Cu Kα, Ni Kα, Co Kα, V Kα, Ti Kα). Counting times were: 30 sec for Zn Kα, Cr Kα, Sb Lα, Cd Lα, Ag Lα, Hg Mα, Te Lα, Pb Mα, Au Mα, As Lα, Se Lα, Cu Kα, Ni Kα, Co Kα, V Kα, Ti Kα; 20 sec for Fe Kα and Bi Mα; 10 sec for S Kα. Off peak counting times were identical to the counting time. Detection limits for each analyzed element measuring ore minerals and quartz are summarized in Table 2.2.

Quality control was maintained by utilizing MUN internal standards for each analyzed phase; calibration standards were measured at the beginning and end of the phase in question and after every 20 analyses. Measured values of each internal standard were in accordance with the accepted concentrations in these standards (W. Aylward, personal communication 2019). Additionally, data were deemed acceptable if analytical totals fell within a range of 100 ± 1.5 wt% and their stoichiometry represented the accepted mineral composition. All presented analyses of sulfide minerals, Bi-, Te- and Au-phases and quartz fell within this range or were discarded. The

only exception are some Bi and Bi-Te phases that have accepted totals between 98.1 and 101.8 wt%. These values were deemed acceptable after careful textural observation of the analyzed grains to exclude any overlap with adjacent phases. Additionally, the grain size of these analyzed points is generally < 10 μm and also the spot analyses was set as best as possible in the center of each grain, grain size effects on the total cannot be completely excluded.

Table 2.2. Detection limit and standard deviation in ppm for elements analyzed in ore minerals and quartz using the JEOL JXA-8230 Superprobe. n – number of analyses, Std – standard deviation.

	Ore Minerals (n=197)		Quartz (n=31)	
Element	**Average**	**Std**	**Average**	**Std**
S [ppm]	33.9	3.88	37.1	2.07
Fe	151	40.0	120	3.22
Cu	40.1	10.3	29.1	0.27
As	102	24.7	100.0	2.07
Zn	263	77.5	176	2.25
Pb	83.9	20.8	45.7	1.82
Au	96.3	22.7	59.0	2.48
Ag	32.9	5.65	24.1	0.37
Hg	95.6	22.4	59.2	2.27
Bi	78.1	23.1	51.8	1.92
Te	35.2	5.76	29.6	4.47
Se	50.8	12.4	50.4	1.24
Sb	39.9	6.66	35.3	5.65
Cd	32.9	5.52	25.2	0.43
Cr	160	42.3	153	4.29
Co	31.5	7.00	23.2	0.24
Ni	36.8	9.47	27.6	0.31
V	27.2	5.53	24.8	0.62
Ti	31.8	6.15	33.5	1.04

For quartz analysis, a total SiO_2 concentration of 99.9 wt% was assumed in order to determine the composition of the analyzed 19 elements, because the focus of this study is on the metal concentrations in different phases. The accuracy of the results was monitored via MUN in-house standards. The results above detection limit were within 5 % of the accepted values. Moreover, wavelength scans of the unknown samples were undertaken to monitor background

conditions, potential peak overlaps and interferences, and to check the quality of minor element peaks. Precision of each analysis was calculated from the counting rate and is below 0.4 % for all major elements; precision for minor components is between 5 and 33 %. However, precision increases with increasing concentrations for minor components. Unknown and standard intensities were corrected for dead time. Standard intensities were corrected for standard drift over time by internal software corrections. Interference corrections were applied to Cd for interference by Ag; to V for interference by Ti; to Hg for interference by Ag; to Te for interference by Ag; to Bi for interference by Pb; and to Cr for interference by Bi and V.

Secondary ion mass spectrometry was performed on four samples from mineralized veins and an arsenopyrite veinlet in tonalite to determine the $\delta^{34}S$ composition relative to the Vienna Canyon Diablo Troilite (VCDT) of pyrrhotite (n=13), pyrite (n=9), chalcopyrite (n=6), and arsenopyrite (n=4). The grains were chosen based on mineral assemblage, size, and texture.

The sulfur isotopic composition of materials is expressed in delta (δ) notation, as parts per thousand variation relative to a reference material and expressed in per mil (‰). Mathematically, the S isotopic composition of any substance is expressed as:

$$\delta^{34}S = \left[\frac{(^{34}S/^{32}S)_{Sample} - (^{34}S/^{32}S)_{Reference}}{(^{34}S/^{32}S)_{Reference}}\right] \times 1000 \qquad \text{(Eq. 1)}$$

with $(^{34}S/^{32}S)_{Sample}$ is the measured $^{34}S/^{32}S$ ratio of the sample, $^{34}S/^{32}S_{Refernce}$ is the known $^{34}S/^{32}S$ ratio of the reference material. For sulfur isotopic composition the agreed upon reference is the Vienna Canyon Diablo Troilite (VCDT) with a $\delta^{34}S$ = 0 ‰ by definition (Krouse and Coplen, 1997).

Sample preparation prior to analyses involved mounting 1 cm x 1cm sample slabs in polished epoxy sections that were coated with 300Å of Au in order to mitigate charging under

primary ion bombardment. All analyses were performed using the Cameca IMS 4f Secondary Ion Mass Spectrometer (SIMS) at the Microanalysis Facility of the CREAIT Network, Bruneau Center of MUN following the described methodology of Brueckner et al. (2015).

For each sample, determinations of $\delta^{34}S$ were performed on multiple grains of pyrrhotite, pyrite, chalcopyrite, and arsenopyrite. Each analysed spot was bombarded with a primary ion microbeam of 350–1,150 pA of Cs^+, accelerated by a 10 keV potential, and focused into a 5–15 µm diameter spot. The Cs^+ current depended on the analyzed sulfide phase, the size of the analyzed phase, and the matrix surrounding the analyzed grain (sulfides or non-sulfide gangue). Contamination in the polished surface was prevented by pre-sputtering each spot for 120 sec with a 25 µm square raster prior to analyses. Depending on the minimum diameter of the critically focused analysis, the homogeneity of primary ion delivery was improved by maintaining lateral resolution at better than 20 µm. Negatively charged sputtered secondary ions were accelerated into the mass spectrometer using a potential of 4.5 keV.

The instrument was operated with a medium Contrast Aperture (150µm), and Entrance and Exit Slits paired to give flat-topped peaks at a mass resolving power of 2,975 (10 % peak height definition) - sufficient to discriminate $^{33}SH^-$ (and $^{32}SH_2^-$) from $^{34}S^-$.

In-house standards used to monitor instrumentation and analysis were: (1) PoW1 ($\delta^{34}S$ = 2.3 ‰) for pyrrhotite; (2) UL9 ($\delta^{34}S$ = 15.8 ‰) for pyrite; (3) USGS Norilsk ($\delta^{34}S$ = 8.3 ‰) for chalcopyrite; and (4) Arspy57 ($\delta^{34}S$ = 2.8 ‰) for arsenopyrite. More information about the in-house standards used in this study can be found in Brueckner et al. (2015).

Analyses accumulated in 12 minutes and routinely yielded internal precisions on individual $\delta^{34}S$ determinations of better than ± 0.4 ‰ (1σ), while producing sputter craters only a few µm

deep. These precisions closely approach the optimal precision as calculated from Poisson counting statistics. Overall reproducibility, based on replicate standard analyses, is typically better than ± 0.5 ‰ (1σ). Results of analyzed in-house standards Po W1, UL 9, USGS Norilsk, and Arspy 57 are shown in Table 2.3. The results are consistent to the respective accepted values and corrected for Instrument Mass Fractionation (IMF) that was calculated during data reduction based on the measured $^{34}S/^{32}S$ ratio.

This approach is closely comparable to the "shallow pit" method of Kozdon et al. (2010). Their study demonstrated that any effects due to grain orientation or sputtering response were subsidiary to the better than ± 0.3 ‰ (2σ) overall reproducibility they achieved for replicate analyses of pyrite, chalcopyrite, and pyrrhotite.

Table 2.3. Results of measured $^{34}S/^{32}S$ ratio, calculated instrumental mass fractionation, and $\delta^{34}S$ analysis corrected for IMF of the used in-house standards analyzed via SIMS. IMF – Instrumental mass fractionation; SEM – standard error mean; VCDT – Vienna Canyon Diablo Troilite.

In-house standard name	$^{34}S/^{32}S_{measured}$	SEM [%]	$IMF_{calculated}$ [‰ VCDT]	$\delta^{34}S_{corrected}$ [‰ VCDT]	SEM [1σ]	$\delta^{34}S$ accepted value [‰ VCDT]
PoW1	0.043568	0.023	-16.4	2.8	0.2	2.3
PoW1	0.043580	0.033	-16.4	3.1	0.3	2.3
UL9	0.044260	0.033	-13.7	15.9	0.3	15.8
UL9	0.044261	0.021	-13.7	15.9	0.2	15.8
UL9	0.044297	0.038	-13.7	16.7	0.4	15.8
USGS Norilsk	0.043960	0.028	-11.9	7.3	0.3	8.3
USGS Norilsk	0.044027	0.039	-11.9	8.8	0.4	8.3
USGS Norilsk	0.044029	0.041	-11.9	8.9	0.4	8.3
USGS Norilsk	0.044009	0.038	-11.9	8.4	0.4	8.3
Arspy 57	0.043713	0.023	-13.0	2.8	0.2	2.8
Arspy 57	0.043712	0.022	-13.0	2.7	0.2	2.8

2.6 Results

Ore minerals from six samples were analyzed using EPMA and SIMS to detect the major, minor and trace element composition, and the sulfur isotopic composition, respectively. For EPMA, a total of 130 measurements were made on pyrrhotite (n=39), pyrite (n=21), chalcopyrite (n=11), arsenopyrite (n=19), sphalerite (n=5), galena (n=7), native bismuth (n=8), hedleyite (n=3), 'unnamed bismuth telluride phase' (Bi_3Te, n=3), electrum (n=2), hessite (n=3), and quartz (n=9) from all six samples (Table 2.4). A total of 33 sulfur isotope analyses were made on pyrrhotite (n=13), pyrite (n=10), chalcopyrite (n=6), and arsenopyrite (n=4) from four samples via SIMS (Table 2.4). The results for both methods are described here.

Table 2.4. Summary of samples analyzed for EPMA and SIMS, their ore assemblage and average Au grade. Apy – arsenopyrite, Bi_3Te – 'unnamed Bi_3Te phase', Bis – bismuthinite, Ccp – chalcopyrite, El – electrum, Hed – hedleyite, Hess – hessite, Gn – galena, Mal – maldonite, N – not analyzed, native Au – native gold, native Bi – native bismuth, Po – pyrrhotite, Py – pyrite, Sp – sphalerite, ✓ – analyzed.

Sample No.	Drill hole	Depth [feet]	Au grade [oz/t]	Ore assemblage	EPMA	SIMS
4164	HM-114	156.60	2.21	Po + Py + Ccp + Hed + Bi_3Te + native Bi + El + native Au	✓	
4169	HM-71	219.00	0.34	Po + Py + Ccp + Sp + Hed + Bi_3Te + native Bi + Bis + El + native Au ± Mal		✓
4173	HM-71	267.10	1.57	Po + Py + Ccp + Hed + Bi_3Te + native Bi + Bis + El + native Au ± Mal	✓	
4185	HM-58	80.00	0.007	Py + Sp Apy + Po + Ccp + Gn + Hed + Bi_3Te + Hess	✓	✓
4194	HM-58	464.75	0.006	Apy + Py + Po + Ccp	✓	✓
4199	HM-130	117.00	2.44	Po + Py + Ccp + Hed + Bi_3Te + native Bi + Bis + El + native Au ± Mal	✓	✓
4200	HM-130	117.25	2.44	Po + Py + Ccp + Hed + Bi_3Te + native Bi + Bis + El + native Au ± Mal	✓	

2.6.1 EPMA

Compositional results for base metal sulfides pyrrhotite, pyrite, chalcopyrite, arsenopyrite, sphalerite, and galena are summarized in Table 2.5. Details are found in Appendix C. Most of the base metal sulfides (pyrrhotite, pyrite, chalcopyrite, arsenopyrite) analyzed from Hog Mountain are stoichiometrically homogenous. Their calculated mineral formulae are: (1) pyrrhotite (n=39) with $Fe_{(1-x)}S$, x=0.09-0.15; (2) pyrite (n=21) with $Fe_{0.98-1.03}S_2$; (3) chalcopyrite (n=11) with $Cu_{0.99-1.00}Fe_{1.01-1.03}S_2$; and (4) arsenopyrite (n=19) with $Fe_{0.96-1.01}As_{0.91-1.01}S$, although arsenopyrite can have weak deficits in arsenic. Sphalerite and galena show prominent substitutions in the cation site resulting in mineral compositions that are non-ideal. Substitutions of Fe^{2+} and Cd^{2+} for Zn^{2+} in sphalerite are observed in all analyses and range between 7.6 to 8.3 wt% and 1.0 to 1.1 wt% for Fe and Cd, respectively (Fig. 2.10A, B). The resulting mineral formula for sphalerite (n=5) is $(Zn_{0.84-0.86}, Fe_{0.13-0.14}, Cd_{0.01})_{\Sigma 0.99-1.00}S$. The reported substitutions are common for sphalerites from different environments (DiBenedetto et al., 2005; Cook et al., 2009). Galena has a coupled substitution of Bi^{3+} and Ag^{+} for $2Pb^{2+}$ (van Hook, 1960; Blackburn and Schwendeman, 1977; Foord and Shawe, 1989; Renock and Becker, 2011) with Bi and Ag concentrations ranging between 0.6 to 2.6 wt% and 0.15 to 1.1 wt%, respectively (Fig. 2.10C, D). The resulting mineral formula for galena is $(Pb_{0.94-0.97}, Bi_{0.01-0.03}, Ag_{0.00-0.02})_{\Sigma 0.98-0.99}S$ (n=7).

Trace concentrations vary widely in all base metal sulfides (Fig. 2.11, Table 2.5). Bismuth and Au are present in all analyzed base metal sulfides other than galena, which has up to several wt% Bi but no detected Au (Fig. 2.11A, B). Bismuth and Au concentrations reach up to several hundred ppm in pyrrhotite, pyrite, chalcopyrite, arsenopyrite and sphalerite. Average concentrations of Bi are 258 ± 115 ppm (pyrrhotite, n=24), 185 ± 97 ppm (pyrite, n=12), 238 ± 38 ppm (chalcopyrite, n=9), 2375 ± 12 ppm (arsenopyrite, n=4), and 360 ± 93 ppm (sphalerite, n=5).

Average concentrations of Au are 293 ± 156 ppm (pyrrhotite, n=29), 297 ± 148 ppm (pyrite, n=14), 294 ± 138 ppm (chalcopyrite, n=4), 266 ± 134 ppm (arsenopyrite, n=14), and 190 ± 95 ppm (sphalerite, n=3). In addition to Bi and Au, concentrations of Co are recorded in many analyzed base metal sulfide grains with the exception of sphalerite and galena (Fig. 2.11C). Arsenopyrite in particular has relatively high Co concentrations with an average of 485 ± 345 ppm and maximum of 1130 ppm (n=17) due to the substitution of Co^{2+} for Fe^{2+} (Clark, 1960; Klemm, 1965). Concentrations of Pb were measured only in a small number of pyrite, pyrrhotite and chalcopyrite grains with concentrations generally below 300 ppm (one exception of pyrite with 430 ppm Pb). Lead is absent in sphalerite whereas arsenopyrite contains up to 857 ppm Pb with an average of 410 ± 186 ppm (Fig. 2.11D). Among the other analyzed trace elements, Ag concentrations in chalcopyrite (average 138 ± 80 ppm, n=11; Fig. 2.11G) and Cr concentrations in arsenopyrite (average 407 ± 168 ppm, n=11) are notable. However, both elements are uncommon or absent in other base metal sulfides. Concentrations of transition metals Ni, V, and Ti are either rare in the analyzed base metal sulfides, have relatively low (<100 ppm) concentrations, or both. Correlations between Bi and Au, Au and Ag, and Au and Co are not observed (Fig. 2.11 E, G, H). A weak positive correlation between Bi and Co exists in pyrrhotite grains (Fig. 2.11F).

Table 2.5. Summary of EPMA data for base metal sulfides. Pyrrhotite and pyrite. Mineral formulae calculated based on one S atom and two S atoms for pyrrhotite and pyrite, respectively. **Abbreviations:** bdl – below detection limit, Max – maximum measured value, Min – minimum measured value, n – number of analyses above detection limit, Std – standard deviation. - indicates not detected.

Mineral and calculated formula	**Pyrrhotite [$Fe_{(1-x)}S$ with x=0.09-0.15]**				
	n	**Average**	**Std**	**Min**	**Max**
S [wt%]	39	39.7	0.34	39.1	40.3
Fe	39	60.8	0.73	59.6	62.0
Cu [ppm]	14	73.5	22.35	42	114
As	4	215	130	115	389
Zn	1	3239		3239	3239
Pb	7	170	38.0	120	218
Au	29	293	156	97	627
Ag	11	72.9	36.7	33	143
Hg	4	121	23.2	103	155
Bi	24	258	115	80	478
Te	8	78.9	18.0	53	104
Se	7	234	111	122	392
Sb	2	61.5	4.95	58	65
Cd	19	93.3	44.6	33	172
Cr	3	274	87.4	173	330
Co	31	147	87.6	33	381
Ni	16	91.9	41.3	42	192
V	11	64.9	30.7	32	114
Ti	13	69.2	30.5	33	153
Total [wt%]	**39**	**100.6**	**0.60**	**99.7**	**101.5**

Mineral and calculated formula	**Pyrite [$Fe_{0.98-1.03}S_2$]**				
	n	**Average**	**Std**	**Min**	**Max**
S [wt%]	21	53.9	0.47	52.9	54.6
Fe	21	46.8	0.49	46.3	48.0
Cu [ppm]	7	110	59.3	45	212
As	3	234	85.7	183	333
Zn	1	1461		1461	1461
Pb	5	173	146	91	430
Au	14	297	148	99	537
Ag	6	63.2	27.1	35	106
Hg	0	-		-	-
Bi	12	185	97.2	82	388
Te	1	56.0		56	56
Se	3	136	68.9	63	200
Sb	0	-		-	-
Cd	7	68.7	35.9	34	142
Cr	5	320	151	168	514
Co	10	132	99.2	46	367
Ni	4	86.0	17.5	70	104
V	7	51.4	17.3	31	76
Ti	8	72.9	33.3	32	118
Total [wt%]	**21**	**100.8**	**0.31**	**100.2**	**101.3**

Table 2.5. *[continued]* Chalcopyrite and arsenopyrite. Mineral formulae calculated based on two S atoms and one S atom for chalcopyrite and arsenopyrite, respectively.

Mineral and calculated formula	**Chalcopyrite [$Cu_{0.99-1.00}Fe_{1.01-1.03}S_2$]**				
	n	**Average**	**Std**	**Min**	**Max**
S [wt%]	11	34.8	0.20	34.5	35.2
Fe	11	30.9	0.24	30.4	31.2
Cu	11	34.4	0.25	33.8	34.7
As [ppm]	1	259		259	259
Zn	0	-		-	-
Pb	2	218	73.5	166	270
Au	4	294	138	205	498
Ag	11	138	80.3	44	296
Hg	0	-		-	-
Bi	9	238	87.7	103	354
Te	2	59.5	27.6	40	79
Se	2	148	23.3	132	165
Sb	1	42.0		42	42
Cd	7	100	44.8	34	159
Cr	1	197		197	197
Co	3	87.3	16.2	77	106
Ni	3	97.3	27.3	68	122
V	3	41.0	13.2	31	56
Ti	1	97.0		97	97
Total [wt%]	**11**	**100.2**	**0.56**	**99.1**	**101.0**

Mineral and calculated formula	**Arsenopyrite [$Fe_{0.96-1.01}As_{0.91-1.01}S$]**				
	n	**Average**	**Std**	**Min**	**Max**
S [wt%]	19	19.9	0.32	19.5	20.8
Fe	19	34.4	0.21	34.1	35.0
As	19	45.5	0.48	44.1	46.1
Cu [ppm]	4	67.5	16.8	49	85
Zn	1	1326		1326	1326
Pb	17	410	186	136	857
Au	14	266	134	110	543
Ag	2	99.5	41.7	70	129
Hg	0	-		-	-
Bi	4	375	112	244	500
Te	6	161	124	53	394
Se	0	-		-	-
Sb	2	126	79.9	69	182
Cd	10	102	42.2	41	165
Cr	11	407	168	231	747
Co	17	485	343	90	1130
Ni	4	58.3	19.4	40	75
V	7	86.1	33.2	48	155
Ti	7	75.1	27.9	36	107
Total [wt%]	**19**	**99.9**	**0.28**	**99.5**	**100.5**

Table 2.5. *[continued]* Sphalerite and galena. Mineral formulae calculated based on one S atom for both sphalerite and galena.

Mineral and calculated formula	Sphalerite $[(Zn_{0.84-0.86}, Fe_{0.13-0.14}, Cd_{0.01})_{\Sigma 0.99-1.00}S]$				
	n	**Average**	**Std**	**Min**	**Max**
S [wt%]	5	33.5	0.15	33.4	33.7
Fe	5	7.85	0.26	7.60	8.25
Zn	5	58.0	0.35	57.4	58.3
Cd	5	1.08	0.04	1.04	1.14
Cu [ppm]	0	-		-	-
As	0	-		-	-
Pb	0	-		-	-
Au	3	190	94.9	100	289
Ag	0	-	-	-	-
Hg	2	242	145	140	345
Bi	5	360	92.5	285	509
Te	0	-		-	-
Se	1	339		339	339
Sb	0	-		-	-
Cr	1	331		331	331
Co	0	-		-	-
Ni	1	81.0		81	81
V	3	45.3	9.61	35	54
Ti	1	62.0		62	62
Total [wt%]	**5**	**100.5**	**0.22**	**100.2**	**100.8**

Mineral and calculated formula	Galena $[(Pb_{0.94-0.97}, Bi_{0.01-0.03}, Ag_{0.00-0.02})_{\Sigma 0.98-0.99}S]$				
	n	**Average**	**Std**	**Min**	**Max**
S [wt%]	7	13.7	0.06	13.6	13.7
Pb	7	84.6	1.01	82.8	85.8
Ag	7	0.49	0.33	0.15	1.09
Bi	7	1.33	0.70	0.60	2.60
Fe [ppm]	7	3565	4342	435	12915
Cu	0	-		-	-
As	1	185		185	185
Zn	2	6906	1422	5901	7912
Au	0	-		-	-
Hg	0	-		-	-
Te	7	765	257	383	1160
Se	7	591	257	284	891
Sb	0	-		-	-
Cd	3	104	64.4	44	172
Cr	7	2632	406	1930	3118
Co	0	-		-	-
Ni	0	-		-	-
V	1	119		119	119
Ti	3	105	28.3	81	136
Total [wt%]	**7**	**101.1**	**0.51**	**100.2**	**101.5**

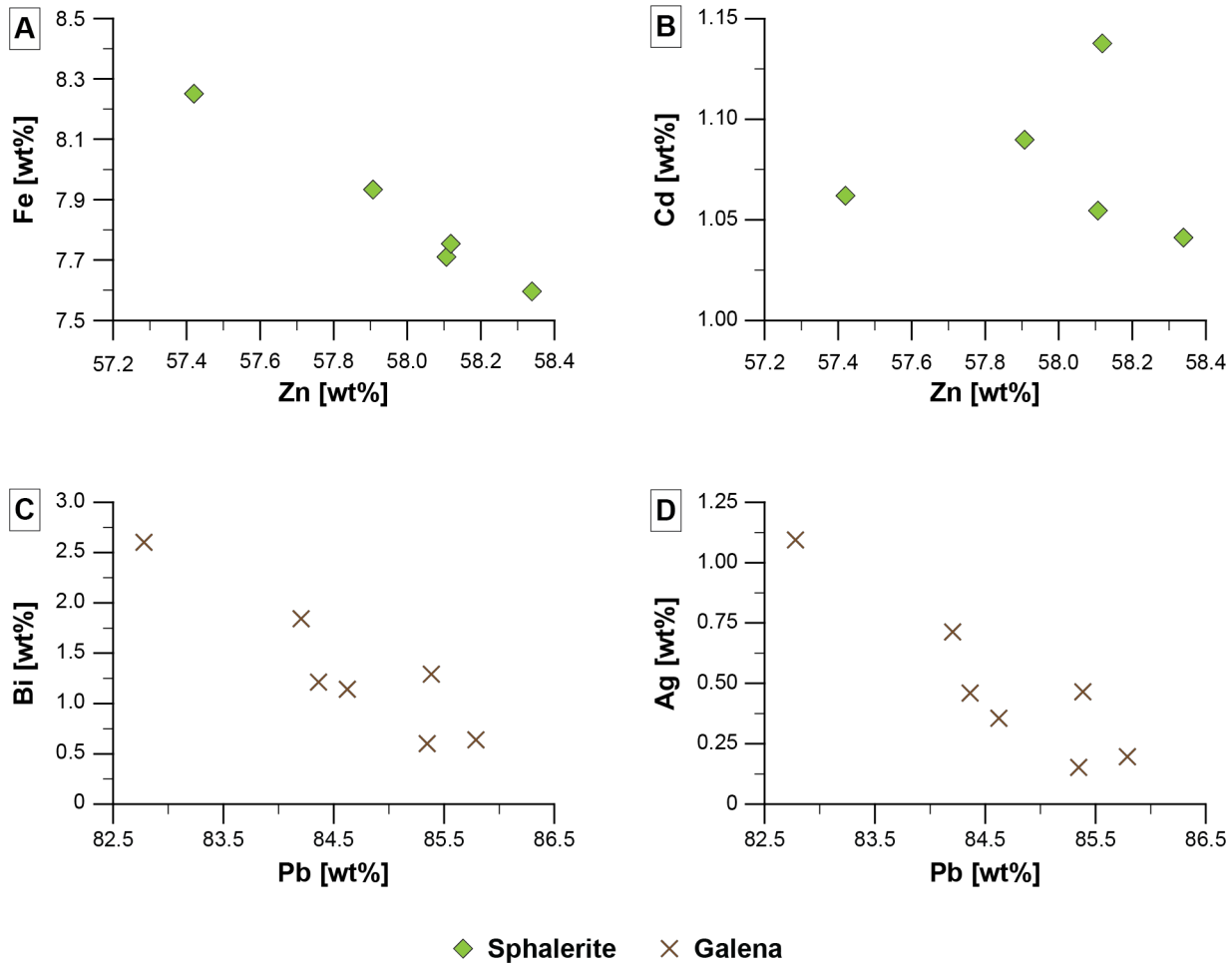

Figure 2.10. Binary plots of substitutions in the cation site in sphalerite and galena. (A) Zn vs Fe. **(B)** Zn vs Cd. **(C)** Pb vs Bi. **(D)** Pb vs Ag.

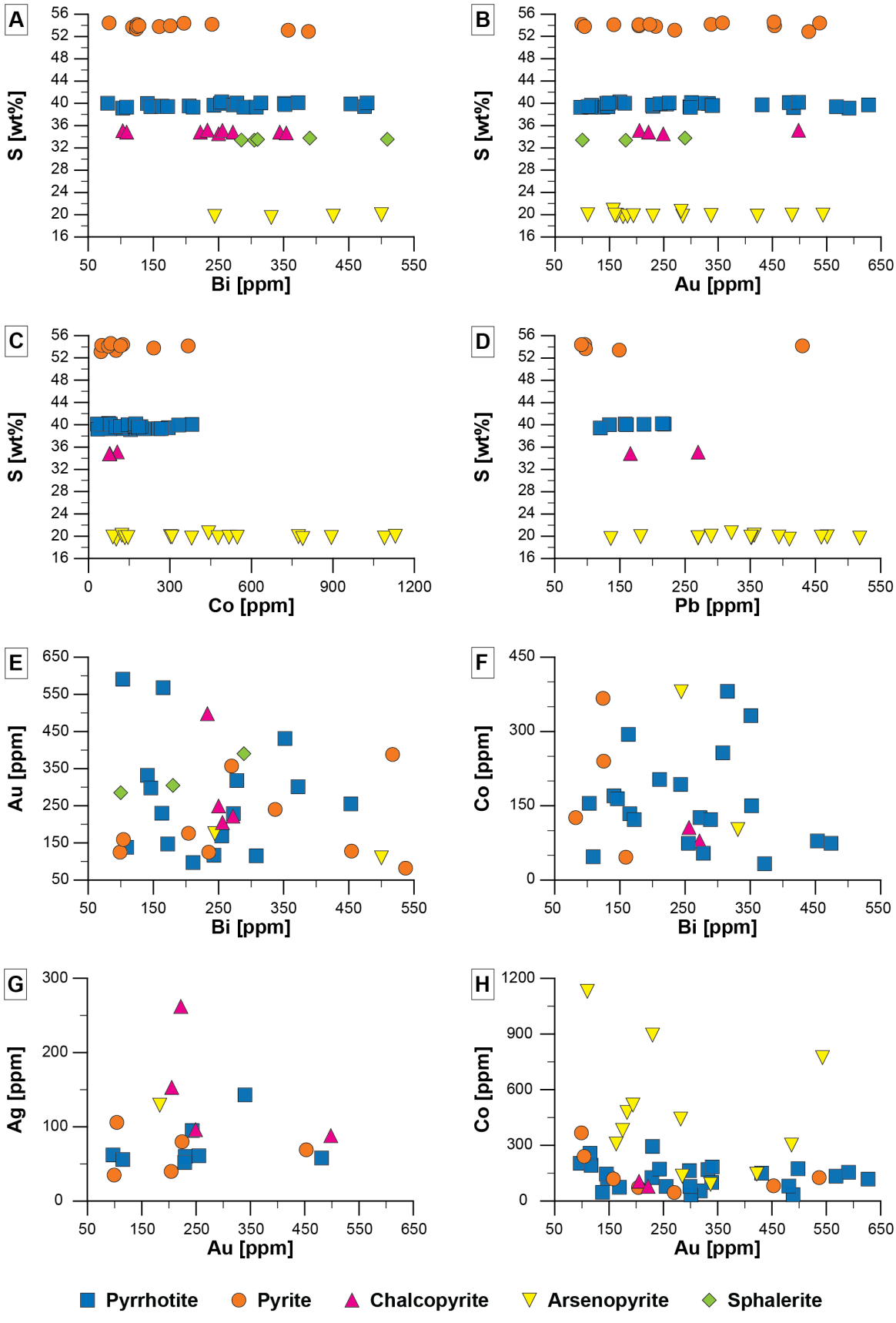
A
S [wt%]
Bi [ppm]
B
S [wt%]
Au [ppm]
C
S [wt%]
Co [ppm]
D
S [wt%]
Pb [ppm]
E
Au [ppm]
Bi [ppm]
F
Co [ppm]
Bi [ppm]
G
Ag [ppm]
Au [ppm]
H
Co [ppm]
Au [ppm]
Pyrrhotite
Pyrite
Chalcopyrite
Arsenopyrite
Sphalerite

Figure 2.11. Binary plots of selected major and trace elements in base metal sulfides. *(previous page)* **(A)** Bi vs S. **(B)** Au vs S. **(C)** Co vs S. **(D)** Pb vs S. **(E)** Bi vs Au. **(F)** Bi vs Co. **(G)** Au vs Ag. **(H)** Au vs Co.

Analyses for Bi-phases, precious metals and quartz are summarized in Table 2.6 and given in detail in Appendix C. Selected trace elements in Bi- and Te-phases are plotted against Bi in Figure 2.12.

Among non-base metal sulfide trace minerals, bismuth chalcogenides dominate proportionally over precious metal phases. Bismuth chalcogenides are minerals of bismuth with tellurium, selenium and/or sulfur and classified into the tetradymite series of Strunz and Nickel (2001). At Hog Mountain, SEM observations reveal native bismuth, bismuth tellurides, and bismuthinite (Figs 2.7 and 2.8). Of these minerals, only native bismuth and bismuth tellurides could be analyzed successfully via EPMA due to grain size restrictions.

The ternary Bi-Te-Ag diagram in Figure 2.12A shows that besides native bismuth, two distinct bismuth chlacogenides occur in the mineralized quartz veins at Hog Mountain. These are hedleyite and an 'unnamed Bi_3Te phase'. Cook et al. (2007) described the complexity that exists within the tetradymite group; compositional variations are expected.

Native bismuth (n=8) has varying Bi contents averaging 99.6 wt%. Three analyses of hedleyite result in a formula of $Bi_{6.85\text{-}7.17}Te_3$ due to relatively wide variations in Bi content (76.8 to 78.2 wt%) at relatively constant Te concentrations of 20 to 20.5 wt%. Hence, the Bi/Te ratio ranges between 3.7 and 3.9. Cook et al. (2007) reported that compositions of hedleyite beyond Bi_7Te_3 are expected in natural systems including an 'unnamed bismuth telluride' with a composition of Bi_3Te. Such a mineral was detected at Hog Mountain and three analyses revealed a composition of 80.7 to 80.9 wt% Bi and 16.8 to 17 wt% Te with a calculated formula of $Bi_{2.90\text{-}}$

$_{2.93}$Te and a Bi/Te ratio of 4.7 to 4.8. Crystallographic data were not performed on this phase and therefore, it cannot be determined if the 'unnamed Bi_3Te phase' is a Bi-rich hedleyite or a separate mineral. In this context, the phase is referred to as an 'unnamed Bi_3Te' phase, although Cook et al. (2007) noted that hedleyite composition does not vary significantly over a certain Bi/Te range within a deposit, but that variations can exist between deposits.

The native bismuth and bismuth telluride phases at Hog Mountain have a wide range of trace element concentrations. In particular, this includes concentrations of several hundred to several thousand ppm of the following: Ag (native bismuth: average 176 ± 109 ppm, n=7; hedleyite: 857 ± 1006 ppm, n=2; Fig. 2.12B); As (native bismuth: 1110 ± 393 ppm, n=8; hedleyite: average 572 ± 290 ppm, n=2; 'unnamed Bi_3Te phase': 778 ± 485 ppm; Fig. 2.12C); Sb ('unnamed Bi_3Te phase': 379 ± 181 ppm, n=5; hedleyite: average 1625 ± 731 ppm, n=2; 'unnamed Bi_3Te phase': 1768 ± 32 ppm, n=3; Fig. 2.12D); and Cr (native bismuth: 1329 ± 651 ppm, n=8; hedleyite: 1522 ± 298 ppm, n=3; 'unnamed Bi_3Te phase': 1182 ± 745 ppm, n=3; Fig. 2.12E). Silver in the 'unnamed Bi_3Te phase' is rare and low with one analysis of 66 ppm (Fig. 2.12B). Other elements at relatively high concentrations in hedleyite and/or 'unnamed Bi_3Te phase' include S with up to 854 ppm in hedleyite, Pb with up to 1087 ppm in hedleyite, and Se with up to 1453 ppm in 'unnamed Bi_3Te phase'. The high trace element concentrations, especially of Sb, Ag, Pb, S, and Se, can be explained by the preferred substitution of Sb, Ag and Pb for Bi, and S and Se for Te (Cook et al., 2007). Gold was detected in only one hedleyite grain (113 ppm) and neither in native bismuth nor the 'unnamed Bi_3Te phase'.

Table 2.6. Summary of EPMA data for Bi, Te and Au phases and quartz. Native bismuth and unnamed bismuth telluride. Mineral formula calculated based on one Te atom for unnamed bismuth telluride. **Abbreviations:** bdl – below detection limit, Max –maximum measured value, Min – minimum measured value, n – number of analyses above detection limit, Std – standard deviation. - not detected.

Mineral and calculated formula	**Native Bismuth [$Bi_{0.96-0.99}$]**					**Mineral and calculated formula**	**Unnamed Bismuth Telluride [$Bi_{2.90-2.93}Te$]**				
	n	**Average**	**Std**	**Min**	**Max**		**n**	**Average**	**Std**	**Min**	**Max**
Bi [wt%]	8	99.6	0.98	98.0	100.6	Bi [wt%]	3	80.8	0.13	80.7	80.9
Te	2	0.62	0.83	0.03	1.21	Te	3	16.9	0.13	16.8	17.0
Au [ppm]	0	-		-	-	Au [ppm]	0	-		-	-
Ag	7	176	109	46	304	Ag	1	66.0		66	66
Hg	2	219	84.9	159	279	Hg	0	-		-	-
S	6	107	80.0	24	213	S	3	200	212	66	445
Fe	7	2448	2473	252	7172	Fe	3	4835	6544	208	9462
Cu	0	-		-	-	Cu	0	-		-	-
As	8	1110	393	657	1729	As	3	778	485	373	1315
Zn	2	5804	2197	4250	7357	Zn	0	-		-	-
Pb	0	-		-	-	Pb	3	564	375	253	981
Se	5	322	154	151	507	Se	3	880	538	386	1453
Sb	5	379	181	180	571	Sb	3	1768	31.7	1744	1804
Cd	8	274	77.9	137	366	Cd	3	176	65.6	113	244
Cr	8	1329	651	465	2480	Cr	3	1182	745	377	1847
Co	2	37.0	2.83	35	39	Co	1	33.0		33	33
Ni	0	-		-	-	Ni	1	37.0		37	37
V	1	55.0		55	55	V	1	84.0		84	84
Ti	2	111	49.5	76	146	Ti	2	98.0	49.5	63	133
Total [wt%]	**8**	**100.5**	**1.28**	**98.5**	**101.8**	**Total [wt%]**	**3**	**98.6**	**0.41**	**98.4**	**99.1**
						Bi/Te	**3**	**4.77**	**0.03**	**4.74**	**4.80**

Table 2.6. *[continued]* Hedleyite and hessite. Mineral formulae calculated based on three Te atoms and one Te atom for hedleyite and hessite, respectively.

Mineral and calculated formula	**Hedleyite [$Bi_{6.85-7.17}Te_3$]**					**Mineral and calculated formula**	**Hessite [$Ag_{2.00-2.06}Te$]**				
	n	**Average**	**Std**	**Min**	**Max**		**n**	**Average**	**Std**	**Min**	**Max**
Bi [wt%]	3	77.3	0.78	76.8	78.2	Ag wt%	3	62.7	1.08	61.4	63.3
Te	3	20.3	0.30	20	21	Te	3	36.5	0.31	36.3	36.8
Au [ppm]	1	113		113	113	Au [ppm]	1	305		305	305
Ag	2	857	1006	146	1568	Hg	2	200	86.3	139	261
Hg	0	-		-	-	Bi	3	325	73.9	240	369
S	3	351	443	18	854	S	3	3007	4074	339	7696
Fe	2	8195	8208	2391	13999	Fe	3	1490	1124	620	2759
Cu	0	-		-	-	Cu	0	-		-	-
As	2	572	290	367	777	As	0	-		-	-
Zn	0	-		-	-	Zn	3	10905	7095	4919	18742
Pb	2	670	590	253	1087	Pb	2	329	327	98	561
Se	2	845	724	333	1357	Se	0	-		-	-
Sb	2	1625	731	1108	2142	Sb	3	2246	30.5	2216	2277
Cd	2	229	242	58	400	Cd	2	187	119	103	271
Cr	3	1522	298	1319	1864	Cr	3	1822	173	1721	2021
Co	1	48.0		48	48	Co	1	37.0		37	37
Ni	2	102	65.1	56	148	Ni	2	83.0	58.0	42	124
V	2	104	84.1	45	164	V	2	160	59.4	118	202
Ti	0	-		-	-	Ti	1	39.0		39	39
Total [wt%]	**3**	**98.7**	**0.62**	**98.1**	**99.3**	**Total [wt%]**	**3**	**101.1**	**0.06**	**101.1**	**101.2**
Bi/Te	**3**	**3.81**	**0.10**	**3.74**	**3.92**	**Ag/Te**	**3**	**1.72**	**0.02**	**1.69**	**1.74**

Table 2.6. *[continued]* Electrum and quartz. Quartz composition of 99.9 wt% SiO_2 was assumed prior to analysis.

Mineral and calculated formula	**Electrum [$(Au_{0.82-0.84}, Ag_{0.14-0.15})_{\Sigma 0.98}$]**			
	n	**Average**	**Std**	**Min**	**Max**
Au wt%	2	90.6	1.21	89.7	91.4
Ag	2	8.70	0.56	8.31	9.10
Hg [ppm]	2	1619	902	981	2256
Bi	2	8210	598	7787	8633
Te	0	-	-	-	-
S	2	662	48.1	628	696
Fe	0	-	-	-	-
Cu	1	68.0		68	68
As	0	-	-	-	-
Zn	0	-	-	-	-
Pb	0	-	-	-	-
Se	0	-	-	-	-
Sb	0	-	-	-	-
Cd	1	156		156	156
Cr	2	2296	391	2020	2573
Co	1	44.0		44	44
Ni	1	43.0		43	43
V	0	-	-	-	-
Ti	2	84.0	11.31	76	92
Total [wt%]	**2**	**100.6**	**0.45**	**100**	**101**
Au/Ag	**2**	**10.4**	**0.81**	**9.9**	**11.0**

Mineral and formula	**Quartz SiO_2=99.9 wt%**				
	n	**Average**	**Std**	**Min**	**Max**
S [ppm]	9	103	99.9	35	358
Fe	7	716	634	178	1611
Cu	5	112	151	34	380
As	0	-	-	-	-
Zn	0	-	-	-	-
Pb	4	88.0	41.4	52	148
Au	7	153	38.7	108	216
Ag	5	54.7	35.4	30	117
Hg	6	265	93.4	137	383
Bi	6	152	108	55	309
Te	4	72.6	53.2	30	144
Se	0	-	-	-	-
Sb	1	269		269	269
Cd	3	43.5	12.5	35	58
Cr	5	71.9	45.0	38	150
Co	1	44.8		45	45
Ni	4	59.5	28.0	34	86
V	8	53.6	26.7	29	109
Ti	7	69.4	34.0	39	125
Total [wt%]	**21**	**0.09**	**0.07**	**0.02**	**0.27**

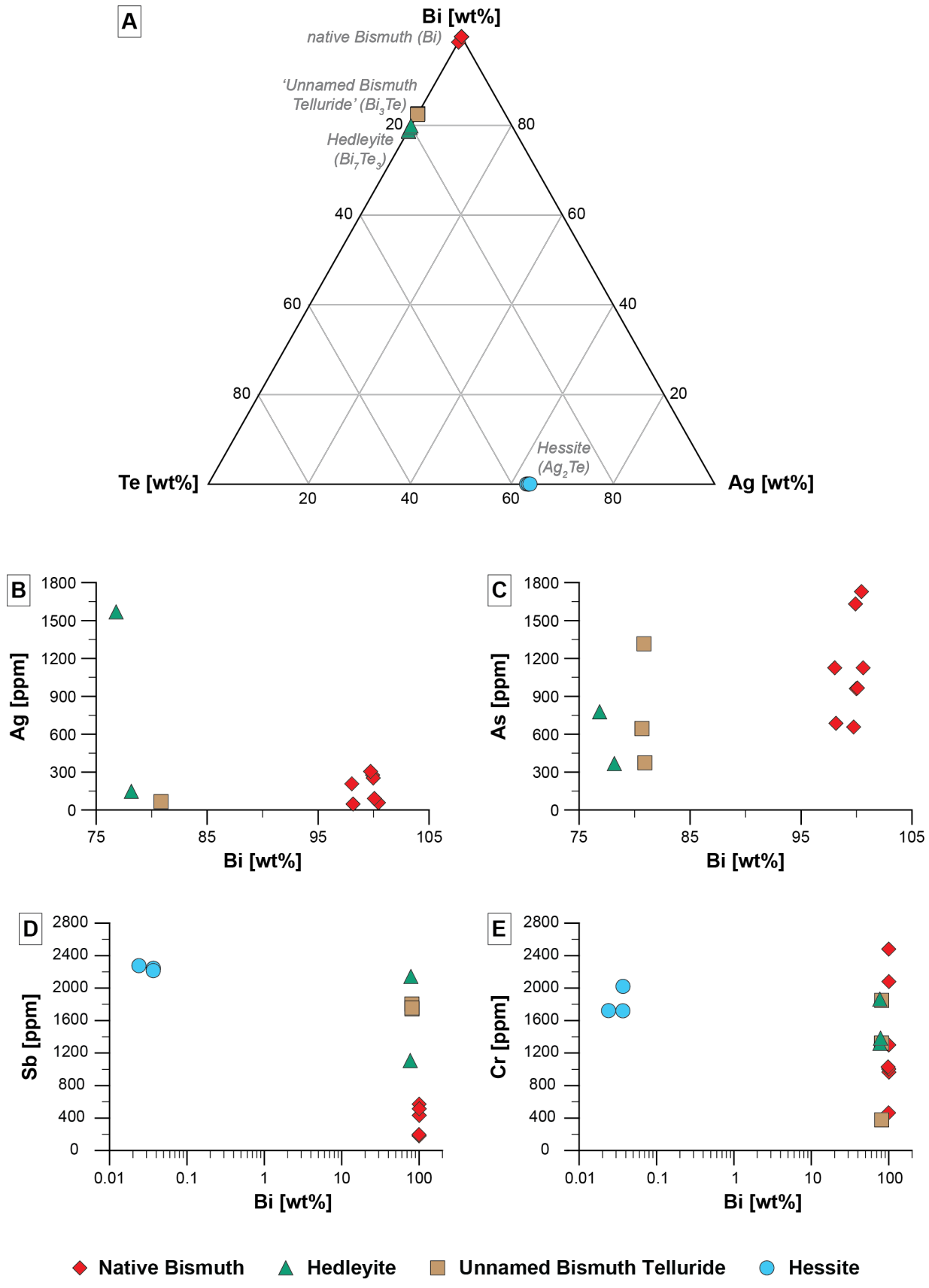
A
Bi [wt%]
native Bismuth (Bi)
'Unnamed Bismuth Telluride' (Bi_3Te)
Hedleyite (Bi_7Te_3)
Hessite (Ag_2Te)
Te [wt%]
Ag [wt%]
20
40
60
80
B
Ag [ppm]
Bi [wt%]
C
As [ppm]
Bi [wt%]
D
Sb [ppm]
Bi [wt%]
E
Cr [ppm]
Bi [wt%]
Native Bismuth
Hedleyite
Unnamed Bismuth Telluride
Hessite

Figure 2.12. Selected major and trace element plots for Bi-Te-Ag phases. *(previous page)* **(A)** Ternary composition plot of Bi-Te-Ag. **(B)** Bi vs Ag. Hessite is not plotted, because Ag is not a major component. **(C)** Bi vs As. Hessite is not plotted, because As is not a major component. **(D)** Bi vs Sb. **(E)** Bi vs Cr.

Hessite is stoichiometrically homogeneous and has a calculated mineral formula of $Ag_{2.00-2.06}Te$ with an average of 62.7 wt% Ag and 36.5 wt% Te (n=3; Fig. 2.12A). Notable trace element concentrations are Sb (average 2246 ± 31 ppm, n=3; Fig. 2.12D) and Cr (average 1822 ± 173 ppm, n=3; Fig. 2.12E). The analyzed grains are < 20μm and spatially close to sphalerite resulting in S, Fe and Zn concentrations of several thousand ppm.

Gold at Hog Mountain occurs as native gold, electrum and maldonite. Successful EPMA analyses were done on only two grains that have an electrum composition of 90.6 ± 1.2 wt% Au and 8.7 ± 0.6 wt% Ag with an Au/Ag ratio of 9.9 to 11 (Table 2.6). Trace elements in electrum generally are not common and low in abundance (< 100 ppm) with the exceptions of Hg (average 1619 ± 902 ppm, n=2), Bi (average 8210 ± 598 ppm, n=2), Cr (average 2296 ± 391 ppm, n=2) and S (average 662 ± 48 ppm, n=2; Table 2.5).

Trace elements were analyzed in vein quartz to investigate whether any significant enrichments occurred. Results for 21 quartz analyses are presented in Table 2.6. In general, only a few grains show detectable amounts of trace elements, which commonly average below 300 ppm. The highest trace element value is Fe with up to 1611 ppm. Gold, Bi and Hg have average concentrations of 153 ± 39 ppm (n=7), 152 ± 108 ppm (n=6), and 265 ± 93 ppm (n=6), respectively. Silver and transition metal (Cr, Co, Ni, V, Ti) concentrations are < 100 ppm and commonly close to the detection limit.

2.6.2 SIMS

Results for 33 SIMS analyses on pyrrhotite (n=13), pyrite (n=10), chalcopyrite (n=6), and arsenopyrite (n=4) are provided in Table 2.6 and shown in Figure 2.13. The selected samples (Table 2.4) are from mineralized quartz veins with moderate to high Au grades (4173, 4199), mineralization on the quartz vein–tonalite contact with a very low Au grade (4185; Fig. 2.5), and an arsenopyrite veinlet with a very low Au grade (4185).

The $\delta^{34}S$ values of sulfide minerals fall within two groups: (1) average $\delta^{34}S_{sulfide}$ = 7.7 ± 0.9 ‰, ranging from 5.2 to 9.0 ‰ (n=26); and (2) average $\delta^{34}S_{sulfide}$ = 12.9 ± 1.4 ‰, ranging from 11.6 to 15.2 ‰ (n=7; Fig. 2.13A). Group 1 includes pyrrhotite, pyrite and chalcopyrite in quartz veins with moderate to high Au grades (4173, 4199), whereas group 2 includes the samples with very low Au grades (pyrrhotites from 4185 and 4195 at the vein-tonalite contact and arsenopyrite from a veinlet).

The sulfur isotopic composition of pyrrhotite is heterogeneous with an average $\delta^{34}S$ of 9.4 ± 2.8 ‰ ranging between 7.3 to 15.2 ‰ (Fig. 2.13B, Table 2.6). In contrast, pyrite (average $\delta^{34}S$ = 7.1 ± 1.0 ‰ with a range of 5.2 to 8.4 ‰), chalcopyrite (average $\delta^{34}S$ = 8.2 ± 0.7 ‰ with a range of 6.9 to 8.9 ‰), and arsenopyrite (average $\delta^{34}S$ = 11.9 ± 0.3‰ with a range of 11.6 to 12.3 ‰) are fairly homogeneous in their sulfur isotopic composition (Fig. 2.13B).

Table 2.7. Sulfur isotopic composition for analyzed base metal sulfides. Abbreviations: Apy – arsenopyrite, Ccp – chalcopyrite, Max – maximum measured value, Min – minimum measured value, n – number of analyses, Po – pyrrhotite, Py – pyrite, SEM – standard error mean, Std – standard deviation, VCDT – Vienna Canyon Diablo Troilite.

Sample No	Spot	$\delta^{34}S$ [‰ VCDT]	SEM
	Pyrrhotite (n=13)		
4194	Po1	7.3	0.8
4194	Po2	7.9	0.5
4194	Po3	7.3	0.4
4194	Po4	7.5	0.6
4199	Po5	8.5	0.4
4199	Po5b	8.5	0.3
4199	Po6	8.3	0.2
4199	Po7	9.0	0.4
4199	Po8	7.4	0.5
4199	Po8b	8.1	0.7
4185	Po9	13.8	0.3
4185	Po9b	15.2	0.4
4185	Po10	13.8	0.5
	Average	***9.4***	
	Std	***2.8***	
	Median	***8.3***	
	Min	***7.3***	
	Max	***15.2***	
	Arsenopyrite (n=4)		
4194	Apy1	12.0	0.5
4194	Apy2	11.6	0.2
4194	Apy3	12.3	0.2
4194	Apy4	11.6	0.3
	Average	***11.9***	
	Std	***0.3***	
	Median	***11.8***	
	Min	***11.6***	
	Max	***12.3***	

Sample No	Spot	$\delta^{34}S$ [‰ VCDT]	SEM
	Pyrite (n=10)		
4169	Py1	5.2	0.5
4169	Py2	6.9	0.3
4169	Py3	6.9	0.9
4169	Py4	6.7	0.8
4169	Py4a	6.4	0.4
4169	Py4b	7.1	0.4
4169	Py4c	6.9	0.2
4194	Py1	8.3	0.7
4194	Py2	8.4	0.6
4194	Py2b	8.1	0.5
	Average	***7.1***	
	Std	***1.0***	
	Median	***6.9***	
	Min	***5.2***	
	Max	***8.4***	
	Chalcopyrite (n=6)		
4194	Ccp1	8.1	0.3
4194	Ccp1b	8.9	0.4
4194	Ccp2	8.5	0.3
4199	Ccp3	7.8	0.3
4199	Ccp3b	8.8	0.5
4199	Ccp4	6.9	0.3
	Average	***8.2***	
	Std	***0.7***	
	Median	***8.3***	
	Min	***6.9***	
	Max	***8.9***	

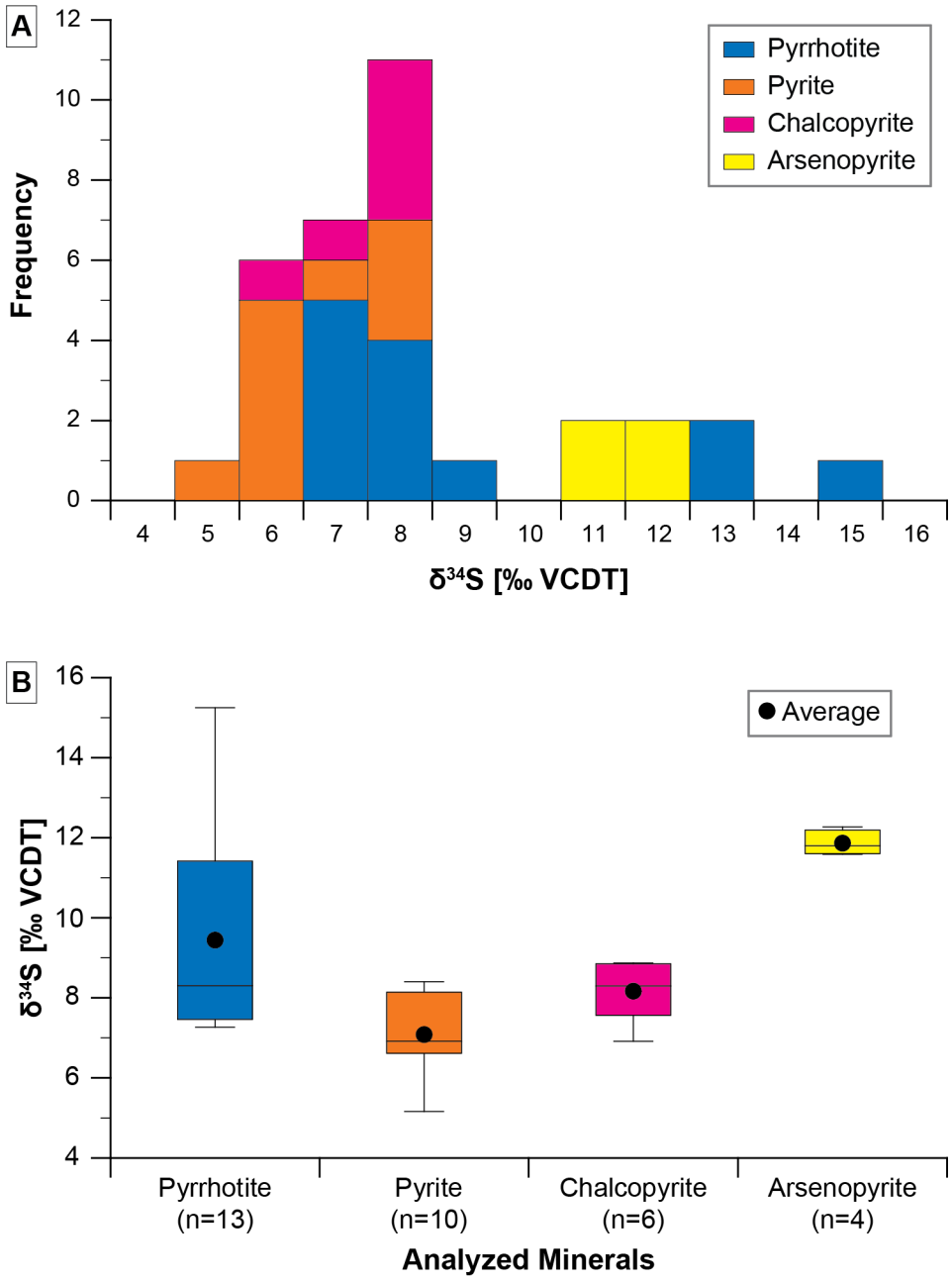

Figure 2.13. Sulfur isotopic composition for base metal sulfides in mineralized veins. (A) Histogram of $\delta^{34}S$ values of analyzed base metal sulfides. **(B)** Box-whisker plot of $\delta^{34}S$ values of analyzed base metal sulfides. **Abbreviations:** n – number of analyses, VCDT – Vienna Canyon Diablo Troilite

2.7 Discussion

The stratigraphic, ore mineralogical, geochemical and isotopic observations outlined above provide insights within the context of the following: (1) the most closely associated deposit type for Hog Mountain – orogenic gold versus reduced intrusion-related gold; (2) the hydrothermal fluid conditions responsible for the formation of mineralized quartz veins at Hog Mountain; (3) the mechanisms responsible for the precipitation of Au; (4) the origin of sulfur and possible indications for the origin of metals; and finally, (5) the genesis of the mineralized veins at Hog Mountain in a regional context.

2.7.1 Deposit Type

Although many Phanerozoic orogenic gold deposits are hosted within metasedimentary rocks, they can also be intrusion-hosted including the Charters Towers deposits in the Lachland Fold belt, Australia (Goldfarb et al., 2005) and the Mokrsko and Jilové deposits in the Bohemian Massif, Czech Republic (Zachariáš et al., 2013, 2014). In the last two decades, a deposit model for intrusion related, gold-only deposits has been postulated (Thompson and Newberry, 2000; Lang, 2001; Hart, 2005, 2007) based on observations in the Tintina Province in the Yukon and Alaska, where Cretaceous intrusions show low-grade gold mineralization within sheeted quartz veins and with a distinct outward metal zoning commonly in close spatial relation to W ± Sn deposits (Hart et al., 2002; Hart, 2005; Mair et al., 2006). This deposit class is referred to as reduced intrusion-related gold (RIRG) type (e.g., Thompson and Newberry, 2000; Lang, 2001; Hart, 2005, 2007). This model, however, stirred a discussion on mineralized veins hosted within intrusions that had been previously classified as orogenic gold deposits (e.g., Donlin Creek, Ebert et al., 2000,

2003; Goldfarb et al., 2004). The main characteristics of both orogenic gold and RIRG deposits is summarized in Table 2.8. Both deposit types share characteristics, which makes distinguishing between them often difficult (Hart and Goldfarb, 2005). Nevertheless, assigning a deposit to a certain model has direct and economic implications on exploration and impacts the understanding of its genesis. Therefore, it is of great importance to evaluate the characteristics of both models in the light of the studied deposit. The characteristics of the mineralized veins at Hog Mountain (this study; Green and Lesher, 1989; Stowell et al., 1989, 1996) are compared to those that have been accepted for orogenic gold and RIRG deposits in Table 2.8.

Green et al. (1987) and Stowell et al. (1989, 1996) both classified Hog Mountain and the coeval mineralized veins of the adjacent Goldville district as orogenic gold deposits. The host tonalite is peraluminous to weakly metaluminous, silica-rich (66.1-74.7 wt%), does not have magnetite (i.e., belongs to the ilmenite series), is rather small (< 0.3 mi^2 surface area), and intruded into sediments away from active continental margins (Green and Lesher, 1989). These characteristics of the host rock are very similar to RIRG deposits (Hart et al., 2002; Hart 2005, 2007; Hart and Goldfarb, 2005). However, no metal zoning is reported around the tonalite, veins extend to depth and are not restricted to the cupola and or carapace of the pluton, single veins with local splay and horsetail textures dominate (Park, 1935; M. Whitney, personal communication 2019), and no Sn ± W deposits occur in close vicinity that are genetically related to the Hog Mountain pluton. The Alabama tin belt around Rockford, Alabama, occurs ca. 25 miles southwest of Hog Mountain; however, tin deposits occur in veins and pegmatites within granitoids of the Pickneyville complex that includes the Elkahatchee quartz diorite and Rockford granite, and is one of the largest intrusions within the eastern Blue Ridge (EBR) and Alabama (Gault, 1945; Wampler et al., 1970; Neathery and Reynolds, 1973).

Tectonic setting, metamorphic grade of the host tonalite, post-peak metamorphism mineralization, and a significant age difference between intrusion and the mineralized veins are more supportive of the orogenic gold model than a RIRG affinity of Hog Mountain (Table 2.8). Furthermore, the hydrothermal fluid conditions that resulted in the ore mineral assemblage documented in this study and by others at Hog Mountain (Ahlrichs, 1982a, b, 1983; Stowell et al., 1996) are consistent with metamorphic fluids that form orogenic gold deposits. This is discussed in more detail below. The Au-Bi-Te mineral assemblage is similar to both orogenic gold and RIRG deposits and is not an unambiguous distinguishing characteristic.

Although the mineralized veins at Hog Mountain show characteristics that are attributed to both orogenic gold and RIRG deposits, the most distinguishing features between both models (i.e., timing of mineralization relative to intrusion, metal zoning including close relation to Sn ± W deposits, and vein morphology) strongly support an orogenic gold model over an RIRG deposit type.

Table 2.8. Comparison of orogenic gold deposits, RIRG deposits and mineralized quartz veins at Hog Mountain. Characteristics for both ore deposit types compiled from Groves et al. (1998), Goldfarb et al. (2005), Hart and Goldfarb (2005), Hart (2007), Goldfarb and Groves (2015), and references therein. Characteristics for Hog Mountain from Green and Lesher (1987), Stowell et al. (1989, 1996, 2015), Smith (2017), and this study.

Characteristic	Orogenic gold deposits	Reduced intrusion-related gold deposits	Mineralized veins at Hog Mountain, AL
Tectonic setting	• Deformed continental margin of mostly allochthonous terranes	• Well inboard of inferred or recognized convergent plate boundaries	• Crustal thickening due to allochthonous thrusting upon continental margin during collisional Alleghanian orogeny
Age	• Archean to Cenozoic	• Dominantly Mesozoic (Tintina Gold Province, Yukon and Alaska) • Fewer Paleozoic examples other than Devonian-Carboniferous • Pre-Cambrian?	• Phyllites: Middle Ordovician (Minimum deposition age: 460 Ma) • Tonalite: 384 ± 32 Ma (upper Devonian) • Mineralization: Late Pennsylvanian during Alleghanian orogeny
Timing of mineralization	• Significantly younger than host rocks • Post-peak metamorphism (≥ 10 Ma) • Host intrusions significantly older than mineralization	• Very late tectonic and post-regional metamorphic peak • Tens to hundreds of Ma after regional peak metamorphism • ≤ 2 Ma after intrusion	• Several 10's of Ma younger than tonalite and > 100 Ma younger than surrounding metasedimentary rocks • Post-peak metamorphism
Formation depth	• Shallow to middle upper crust: 3-15 km • P = 1-5 kbar	• Shallow to middle upper crust: 4-6 km with variations of <1 km to > 8km • P = 0.5-3.5 kbar	• Upper middle crust: ca. 15 km • P = 5.5 ± 1.1 kbar

Table 2.8. *[continued]*

Characteristic	Orogenic gold deposits	Reduced intrusion-related gold deposits	Mineralized veins at Hog Mountain, AL
Host rock(s)	• Meta-volcanic rocks of greenstone belts (dominant in Archean) • Metasedimentary rocks, deep-water turbidite sequences (dominant in Phanerozoic) • Tonalite and granitoid bodies (all ages but minor) of variable composition and size	• Reduced (ilmenite series), metaluminous to lesser peraluminous highly felsic (granite, monzonite, granodiorite, tonalite) intrusions • SiO_2 = 64-72 wt% • No magnetite or hematite, but ilmenite • High volatile content • Small cylindrical shaped plutons of < 1 mi^2 surface area • Intrusion into siliciclastic to carbonaceous (meta-) sedimentary units	• Peraluminous tonalite of ilmenite series • SiO_2: 66.1-74.7 wt% • Ilmenite only Fe-oxide • Small, elongated pluton of <0.3 mi^2 surface area • Intrusion into phyllites (deep-water turbidites)
Metamorphic grade of host rocks	• Commonly greenschist to amphibolite facies	• Dominantly sub-greenschist to greenschist facies • Occasionally amphibolite facies	• Upper greenschist facies (tonalite) to amphibolite facies (phyllite)
Vein morphology	• Variable: Large veins, vein arrays, saddle reefs, sheeted veins, dominantly steep dipping veins (≥ 60˚)	• Sheeted veins in cupola and/or carapace of intrusion	• Dominantly coherent single veins that locally splay or horsetail • Minor zones of thinly sheeted veins in close vicinity to main coherent veins • Veins extend through tonalite into phyllite with average dip of 60˚

Table 2.8. *[continued]*

Characteristic	Orogenic gold deposits	Reduced intrusion-related gold deposits	Mineralized veins at Hog Mountain
Ore mineral assemblage	• Simple base metal mineralogy (pyrite – pyrrhotite ± arsenopyrite) with traces of chalcopyrite – sphalerite – galena • Native gold, electrum • Trace Bi ± Te ± As ± B ± Sb ± W phases	• Simple base metal assemblage of dominantly arsenopyrite – pyrrhotite ± pyrite and locally löllingite • No magnetite or hematite • Typical Au-Bi-Te ± W ± Mo ± As assemblage	• Dominant pyrrhotite with minor to trace pyrite – arsenopyrite and trace chalcopyrite ± sphalerite ± galena • Moderate to relatively high-grade samples: Traces of native bismuth, Bi-chalcogenides (hedleyite, unnamed Bi_3Te, bismuthinite) in close spatial relationship with electrum – native gold ± maldonite • Barren samples: Trace hessite with sphalerite and galena
Proximal alteration	• Varying alteration envelopes depending on host rock composition and metamorphic grade • In equilibrium with host rock mineralogy (e.g. carbonate alteration in dolomitic host rocks) • Common: Mica – carbonate – pyrite	• Neither extensive nor intensive • Limited to thin selvages adjacent to veins • K-feldspar replacement or pervasive carbonate replacement of mafic minerals • Adjacent sericite ± pyrite ± carbonate assemblage overprinting plagioclase and mafic minerals common	• Chlorite – sericite ± carbonate ± pyrite alteration envelopes of varying thickness (< ½ in up to 4 in)

Table 2.8. *[continued]*

Characteristic	Orogenic gold deposits	Reduced intrusion-related gold deposits	Mineralized veins at Hog Mountain
Metal zoning	• Consistent mineralogy over large vertical depth • Cryptic lateral and vertical mineral zoning	• Strong district scale metal zoning • Au-Bi-Te±W to Au-As±W±Sb to As-Sb-Au to Ag-Pb-Zn • Nearby W-Sn mineralization associated with intrusion, skarn mineralization	• No metal zoning with depth or outwards into tonalite and surrounding phyllite
Hydrothermal fluid conditions	• T = 200 – 400˚C, up to 600˚C • pH: near neutral • Reduced: Below hematite-magnetite buffer • Relatively high H_2S: 0.01 – 0.36 mol% • Moderate to rich in CO_2: X_{CO2} = 0.1-0.25 • Low to moderate salinity: 3 – 12 wt% NaCl eq. with Na > K >> Ca, Mg • P = 1-5 kbar • Variable $CH_4 \pm N_2$ concentrations	• T = 200 – 400˚C or > 350˚C • Reduced: At or below quartz-fayalite-magnetite buffer • Carbonic-rich • Variable salinity: < 5 to > 30 wt% NaCl eq. • Very minor $CH_4 \pm N_2$ concentrations	• T = 200 – 400˚C • pH: near neutral • Reduced: At or below pyrrhotite-pyrite-magnetite buffer • Relatively high H_2S • Moderate to high CO_2 • Low to moderate salinity: 0 – 7 wt% NaCl eq. • P ≤ 5.5 ± 1.1 kbar • f_{Te2} significant to form individual tellurides

The Paleozoic, igneous rock-hosted Mokrsko-West and Jilové deposits in the crystalline Bohemian Massif, Czech Republic, also have ambiguous characteristics that overlap with both orogenic gold and RIRG deposit features (Zachariáš et al., 2013, 2014). The Mokrsko-West gold deposit is hosted within 354 Ma tonalite, is dominated by arsenopyrite – pyrrhotite with minor löllingite and traces of Au-Bi-Te-S assemblages, has no significant alteration, and occurs in close proximity to Sn-W deposits (Zachariáš et al., 2014). The Jilové deposit is more geologically complex; hosted by Neoproterozoic metavolcanic rocks and dikes of 355 to 335 Ma, it is dominated by pyrite with minor arsenopyrite and traces of pyrrhotite, magnetite, native arsenic and Bi-Te-S-Au assemblages (Zachariáš et al., 2013). Mineralization age overlaps with intrusions at both deposits. Zachariáš et al. (2013, 2014) postulated an orogenic origin for both ore deposits, however, since they were formed by dominantly metamorphic fluids that originated from the Neoproterozoic basement during the Carboniferous Variscan orogeny as evidenced by their structural, geochemical, and isotope data.

2.7.2 Hydrothermal Fluid Conditions

Hydrothermal fluids play a fundamental role in the formation of ore deposits and their physico-chemical conditions directly control the metals that can be transported (Seward and Barnes, 1997; Seward et al., 2013) and hence, what ore deposit type is formed. In orogenic gold deposits, hydrothermal fluid conditions (Table 2.8) including temperature, pH, redox, H_2S and CO_2 content, salinity, and pressure have been determined from fluid inclusion data, mineral assemblages and geochemistry of natural orogenic ore deposits, and from experimental data (e.g. Yardley and Graham, 2002; Goldfarb et al., 2005; Goldfarb and Groves, 2015; Jébrak and Marcoux, 2015). The data are equivocal and wide ranges exist within some parameters.

The hydrothermal fluids that formed the mineralized veins at Hog Mountain had a temperature below 450 ºC and above 200 ºC. Stowell et al. (1996) determined the peak-metamorphic temperatures within the tonalite at 450 ± 50 ºC based on biotite-garnet thermometry. This temperature is in accordance with the regional metamorphic conditions of upper greenschist to amphibolite facies metamorphism for the EBR (Guthrie and Lesher, 1989; Massey and Moecher, 2005). However, hydrothermal fluid temperatures must have been lower than peak metamorphic temperatures since the quartz veins at Hog Mountain crystallized after the peak of metamorphism (Stowell et al., 1996). This is explained by Stuwe's (1998) "deep later" model in which ascending hydrothermal fluids precipitate metals into retrograde metamorphosed host rocks near the brittle-ductile transition (Groves et al., 1998) commonly resulting in vein-deposit ages that are at least 10 Ma younger than the peak of metamorphism. Unfortunately, the age of metamorphism and mineralization at Hog Mountain is poorly constrained with an assumed metamorphic age of 321 Ma (Ar-Ar age on sheared muscovite in quartz vein; Whitmore, 2018) to 294 ± 16 Ma (cooling Ar-Ar age of muscovite in alteration zone in tonalite; Stowell et al., 1996). This hinders a clear timeline for metamorphic and vein-deposition events at Hog Mountain. Lower fluid temperatures are constrained by the occurrence of sphalerite, galena, and hessite, which all are late stage trace phases (Fig. 2.9); the transport of Zn, Pb and Ag is preferred at temperatures of 300 to 200˚C (Seward, 1976, 1984; Lydon, 1988). Stowell et al. (1996) determined minimum fluid temperatures of 335 ± 40 ºC based on stable isotope geothermometry of quartz and calcite within mineralized veins. These temperatures fall within the assumed temperature range of 400 to 200 ºC based on ore assemblage and metal transport conditions and are also in accordance with the general fluid temperature range for orogenic ore deposits (T = 220 to 450 ºC; Groves et al., 2003; Goldfarb et al., 2005).

Ore-forming fluids in orogenic gold deposits have a near neutral pH (e.g. Goldfarb et al., 2005; Pokrovski et al., 2015) since Au transport by thio-complexes is preferred under these conditions (Seward, 1973; Stefánsson and Seward, 2004; Pokrovski et al., 2015). The ore assemblage at Hog Mountain also supports a near neutral hydrothermal fluid pH since most metals (Fe, Cu, As, Bi, Au, Te) favor transport under such conditions (e.g., Wood et al., 1987; Seward and Barnes, 1997; Wood and Samson, 1998; Williams-Jones et al., 2009). Although alteration is limited to thin envelopes around the mineralized quartz veins, the common chlorite – sericite ± carbonate ± pyrite alteration also reflects near neutral fluid conditions (Mikucki and Ridley, 1993; Hannington et al., 1999). The trace occurrence of sphalerite, galena and hessite, which are indicative of more acidic fluid conditions due to the favored transport of Zn, Pb, and Ag at lower pH (Lydon, 1988, Reed and Palandri, 2006), represent a late stage fluid input at lower temperature and pH than the main fluid event that formed the dominant base metal assemblage with traces of Bi-phases and Au (Fig. 2.9). This late stage fluid event is not associated with Au transport or Fe-sulfide deposition since no spatial relationship is observed of Zn-Pb-Ag phases with either Au or pyrrhotite. Therefore, the late stage fluid input is minor and it is unclear why the fluid conditions changed at the end of the mineral deposition at Hog Mountain, although increased interaction with the tonalite has been suggested (Sha and Lesher, 1990).

Redox conditions in ore-forming fluids of orogenic gold deposits have been described as reduced and below the hematite-magnetite buffer (Phillips and Powell, 1993; Phillips and Evans, 2004) since CO_2-rich fluids (X_{CO2} = 0.1 to 0.25; Ridley and Diamond, 2000), which are common in orogenic gold formation, favor the transport of Au as thio-complexes near neutral pH (Phillips and Evans, 2004). While this study does not present fluid inclusion data, the reduced nature of the fluids is displayed by the dominant occurrence of pyrrhotite and minor to trace arsenopyrite

requiring the system to have been at or below the pyrrhotite-pyrite-magnetite buffer. The transport of arsenic is favored as a hydroxide complex and under reduced conditions; pyrrhotite is commonly deposited with or soon after initial arsenopyrite precipitation in reduced systems (Heinrich and Eadington, 1986). This relationship is also observed at Hog Mountain where arsenopyrite occurs either within or is cross-cut by pyrrhotite. Trace Bi-Te-phases, hedleyite and unnamed Bi_3Te have Bi/Te ratios > 1 that preferably form under reduced fluid conditions at the pyrrhotite-pyrite-magnetite buffer as well (Afifi et al., 1988a; Ciobanu et al., 2005). However, the Fe concentration in sphalerite (7.60 to 8.25 wt%) is more indicative of the hematite-magnetite buffer (Scott and Barnes, 1971; Czamanske, 1974) and underscores the changing fluid conditions that deposited trace sphalerite, galena and hessite along the tonalite-quartz vein contact at a late stage. Stowell et al. (1996) reported moderate to high CO_2 concentrations in secondary fluid inclusions from Hog Mountain, supporting the carbonic-rich character observed in orogenic gold deposits from the Neo-Archean to the Proterozoic (Garofalo et al., 2014).

Hydrothermal ore fluids in orogenic gold systems have significant H_2S with varying concentrations between 0.01-0.36 mol% based on fluid inclusion data (Goldfarb and Groves, 2015). Additionally, hydrothermal fluids have low to weakly moderate salinity (3-7 wt% NaCl eq. with Na > K > Ca, Mg; e.g., Diamond and Ridley, 2000; Groves et al., 2003; Goldfarb et al., 2005; Yardley and Cleverley, 2015), since most of the fluids originate from metasedimentary rocks that were originally formed in deep-seated marine environments (turbidite sequences; Phillips, 1993; Pitcairn et al., 2006; Tomkins, 2010; Yardley and Cleverley, 2015) that were diluted by the release of bound water during diagenesis and metamorphism and a lack of recharge by surface waters (Yardley and Graham, 2002). The relatively high H_2S concentration and low salinity in hydrothermal fluids favor the transport of Au as thio-complexes despite fluid temperatures > 300

ºC (Seward, 1973; Stefánsson and Seward, 2004; Williams-Jones et al., 2009; Pokrovski et al., 2015). This has been proposed as a dominant Au transport process in many orogenic gold deposits (e.g., Goldfarb et al., 1988; Kontak and Smith, 1993) and is also supported by the trace occurrence of common sulfides of metals that prefer chloride-transport (Cu, Zn, Pb, Ag) such as chalcopyrite, sphalerite, galena and Ag-phases. This is observed at Hog Mountain as well. Stowell et al. (1996) reported salinity ranges within fluid inclusions from mineralized quartz veins between 0 to 7 wt% NaCl eq. with higher salinities in later stage fluid inclusions. This increase is explained by Sha and Lesher (1990) as progressively more extensive interaction of fluids with the tonalitic wall rock, which likely resulted in the late stage precipitation of sphalerite, galena and hessite along tonalite-quartz vein contacts.

Hydrothermal fluids forming orogenic gold deposits are commonly deposited at depths of 3-15 km, equivalent to pressures of 1-5 kbar (Groves et al, 2003; Goldfarb et al., 2005). Stowell et al. (1996) constrained the metamorphic peak pressure for the Hog Mountain tonalite at 5.5 ± 1.1 kbar. However, pressures under which ore deposition occurred are likely lower since the deposition occurred both post-peak and during retrograde metamorphism (Stowell et al., 1989, 1996; Stuwe, 1998). Therefore, the emplacement of mineralized quartz veins at Hog Mountain occurred at $P < 5.5 \pm 1.1$ kbar at upper crustal levels, consistent with orogenic gold deposit formation (e.g., Goldfarb et al., 2005; Goldfarb and Groves, 2015).

Even though the hydrothermal fluids responsible for the formation of Au-bearing quartz veins at Hog Mountain reflect the typical physico-chemical conditions of ore fluids forming orogenic gold deposits in regard to temperature, pH, redox state, H_2S and CO_2 content, salinity, and pressure, it is necessary to emphasize that the fluids had also a f_{Te2} high enough to allow for

the deposition of tellurides rather than only the substitution of Te^{2-} for S^{2-} in sulfides (Afifi, 1988a, b; Brueckner et al., 2016).

2.7.3 Gold Precipitation Mechanism

The precipitation of Au in orogenic gold systems has been attributed to three processes: (1) sulfidation of wall rocks with high Fe/(Fe+Mg) ratios that result in the destabilization of Au-transporting thio-complexes (Philips and Groves, 1984; Böhlke, 1988); (2) changes in the redox state and/or pH of the hydrothermal fluid due to CO_2 and K metasomatism resulting in the breakdown of Au-transporting thio-complexes (McCuaig and Kerrich, 1988; Böhlke, 1989); and (3) fluid unmixing into vapor- and fluid-rich phases due to pressure fluctuations of ascending hydrothermal fluids resulting in the partitioning of H_2S into the vapor phase and Au in the fluid resulting in Au precipitation due to non-available complex-forming ligands (Loucks and Mavrogenes, 1999). The first two processes are related to hydrothermal fluid – wall rock interaction and have been postulated as the main Au precipitation processes in orogenic gold deposits for a wide range of host rocks (e.g., Böhlke, 1989; Zachariáš et al., 2014; Fabricio-Silva et al., 2019) including Hog Mountain (Green et al., 1987; Stowell et al., 1989, 1996; Sha and Lesher, 1990).

Over the last almost two decades, a fourth Au precipitation process has been postulated for Bi-Te-Au-bearing hydrothermal systems including skarns (Meinert, 2000; Stormont, Tasmania, Australia; Cockerton and Tomkins, 2012), transition porphyry-epithermal deposits (Larga, Romania; Cook and Ciobanu, 2004), volcanogenic massive sulfide deposits (Escanaba Trough, East Pacific; Törmänen and Koski, 2005), and orogenic gold deposits (Maldon, Lachlan Fold Belt, Australia; Ciobanu et al., 2010). This model is referred to as the "liquid bismuth collector model"

(Douglas et al., 2000) or "hydrothermal assisted collector model" (Tooth et al., 2011). Melts of Bi, Bi-Au and/or Bi-Te form directly from the hydrothermal fluid if fluid temperatures are above the respective melting points of the involved phases (melting $T_{native\ bismuth}$ = 271 ºC, melting $T_{native\ Bi\text{-}maldonite}$ = 241 ºC, melting $T_{native\ bismuth\text{-}hedleyite}$ = 266 ºC; Elliott, 1965; Okamoto and Massalski, 1983; Okamoto and Tanner, 1990) and metal complexes transporting Bi, Au, and/or Te become insufficient due to changes in fluid chemistry (Ciobanu et al., 2005; Tooth et al., 2008). The resulting metal melts can co-exist with fluids undersaturated in Au but will scavenge Au from the fluid due to its preferred partitioning into Bi(±Te) melts despite the presence of thio- or chloro-complexes in the fluid (Okamoto and Massalski, 1983; Okamoto and Tanner, 1990; Tooth et al., 2008, 2011). This Au scavenging by Bi- and Bi-Te melts can occur simultaneously with Bi(±Te) melt formation or after melt droplets are formed (Ciobanu et al., 2005; Tooth et al., 2011).

The scavenging of Au by Bi(±Te) melts is proposed as the dominant Au precipitation process in mineralized quartz veins at Hog Mountain because of: (1) the sole association of Au-phases (electrum, native gold, maldonite) with Bi- and Bi-Te phases including native bismuth, hedleyite, and unnamed Bi_3Te; and (2) droplet-like or sub-round shape is dominant amongst the observed Bi-Te-Au±S phases. The preferred association of Au-phases with native bismuth and bismuth tellurides is difficult to explain by fluid – wall rock interaction or boiling because the host tonalite is reduced and will not significantly alter the redox state of the fluid; intrusions in orogenic gold systems are favorable physical traps for fluids but less important chemically, especially if they are close to equilibrium with the ascending fluids (Goldfarb et al., 2005). A decrease in fluid pH by carbonate precipitation in alteration envelopes may have played a subordinate role; however, the observed alteration envelopes are thin and carbonates are rare. Significant changes in pH due to CO_2 metasomatism affecting Au precipitation are more significant in carbonaceous

rocks hosting orogenic quartz veins (McCuaig and Kerrich, 1988). Boiling is excluded at Hog Mountain, since veins are not brecciated and the fluid inclusions studied by Stowell et al. (1996) do not show signs of phase separation.

The Au scavenging model is preferred also because it aligns with the paragenesis of the observed ore minerals at Hog Mountain. In many Bi-Te-Au-bearing orogenic gold deposits, Bi-Te-Au phases have been attributed to late stage hydrothermal fluids (Goldfarb et al., 2005; Voudouris et al., 2013; Morávek 1971 in Zachariáš, 2013). However, deposition of Bi-, Bi-Te- and Au-phases takes place over almost the entire life span of the hydrothermal system because these phases also occur within pyrrhotite and on its margins. The presence of Bi-Au±Te within early to later stage fluids is also documented in the common trace concentrations, particularly of bismuth and gold in most base metal sulfides at Hog Mountain, although the fluids were undersaturated in these phases relative to the produced melts. Tooth et al. (2011) suggested that oxidized fluid conditions must be present to form Bi melts that scavenge gold from fluids because Bi is dominantly transported as a Bi(III)hydroxide complex (Wood et al., 1987; Skirrow and Walshe, 2002) and only the reduction of fluids due to wall rock interaction would force the formation of bismuth melt. However, the fluid conditions at Hog Mountain were reduced as outlined above. On the other hand, Skirrow and Walshe (2002) proposed that bismuth can nevertheless be transported in reduced fluid as a $Bi_2S_2(OH)_2$ complex, which is very sensitive to changes in temperature (Tòrmänen and Koski, 2005). Hence, only a slight, even local decrease in fluid temperature by just a few tens of degrees Celsius could have forced Bi out of the fluid to form a melt since fluid temperatures were above its melting point of 271 ºC. It should be noted, though, that thermodynamic data on Bi behavior in hydrothermal fluids is extremely scarce and

our knowledge is based on a few studies and thermodynamic interpolation; hence, hypothesizing about Bi behavior during changing fluid conditions is difficult.

Symplectitic exsolution or decomposition textures involving native bismuth, gold and maldonite are not observed in the quartz veins at Hog Mountain; native bismuth and bismuth tellurides with native gold and electrum are more common. Gold scavenged by Bi melts will solidify below 241 ºC into maldonite ($AuBi_2$) and native bismuth (Elliot, 1965; Okamoto and Masalsski, 1983). However, maldonite will further decompose into native gold and bismuth below 116˚C (Nakrasov, 1996). Therefore, the absence of symplectitic decomposition textures involving maldonite, native bismuth and native gold at Hog Mountain indicates the almost complete dissolution of maldonite into native bismuth and gold at temperatures below 116 ºC due to slow cooling. Moreover, the presence of electrum with up to 10 wt% Ag in Bi-Te assemblages strongly suggests that Ag was also scavenged by Bi(±Te) melts in addition to Au.

Aside from Au scavenging, textures of Bi-Te-Au minerals at Hog Mountain also support the remobilization of these phases after precipitation. Small droplets of native bismuth with and without bismuth tellurides and/or bismuthinite are frequently observed as trails along quartz grain boundaries, within quartz and along micro-cracks in pyrrhotite (Figs. 2.7E, G, and 2.8E). Additionally, Au-phases are partly associated with these trails or occur between quartz crystals as elongated, vermicular grains with Bi-phases (Figs. 2.7E, F and 2.8E). The remobilization or liberation of Bi-Au phases by post-mineralization events (e.g. vein crystallization, syn- or epigeneitic metamorphism and/or deformation; Romberger; 1986; Marshall et al., 1998) has been proposed for orogenic gold deposits by Mumin et al. (1994) and Dubé et al. (2003, 2004). Goldfarb et al. (2005) stated that the long periods of epi-genetic deformation and uplift associated with orogenic gold deposits also favor remobilization and deformation of Bi-Te-Au phases. Tomkins

(2007), Tomkins and Mavrogenes (2002), and Tomkins et al. (2004, 2007) showed that ore assemblages of low-melting point chalcophile elements (LCME; Frost et al., 2002) including Bi-Te-Au phases can be remobilized internally when both a favorable sulfide assemblage and melt network exist. However, metamorphic grades of the tonalitic host rock during vein formation did not reach the temperatures and pressures that would favor remobilization under upper amphibolite to granulite facies conditions described by those authors. Instead, Bi-Te-Au remobilization must have been syn-depositional in the mineralized veins at Hog Mountain since Bi-Te-Au deposition continued from an early stage that favored conditions in which Bi(±Te) melts formed while veins still crystallized. This allowed for the movement of droplets within and between quartz during continuous Au scavenging. Remobilization related to deformation occurring after mineralization cannot be excluded, since local deformation events D_4 to D_6 are reported for the area (Guthrie and Lesher, 1989).

Bismuthinite rims around native bismuth are common and can be explained by the dissolution of bismuthinite from Bi melts due to retrograde reactions upon cooling (Brown and Nesbitt, 1987). This is because S-rich melts that favor bismuthinite formation do not occur and the melting point for bismuthinite (T = 775 ˚C; Lin et al., 1996) exceeds fluid temperatures of ore-forming fluids at Hog Mountain (i.e., T = 200-400 ˚C).

The relatively high bismuth concentration in galena reflects fluid conditions that did not favor Bi melt formation from the hydrothermal fluid as the temperature required to transport Pb is below the melting point of native bismuth. Instead, bismuth was transported as an aqueous complex and incorporated into galena with Ag by coupled substitution (van Hook, 1960; Blackburn and Schwendeman, 1977; Foord and Shawe, 1989; Renock and Becker, 2011). It is noteworthy that Bi-enriched galena has no spatial relation to Au-phases and no gold was detected

by EMPA. This suggests that this late stage fluid was not able to deposit gold as separate phase by Au scavenging via Bi(±Te) melts or within sulfides by the breakdown of thio-complexes due to fluid – wall rock interaction.

2.7.4 Origin of Sulfur and Metals

2.7.4.1 Sulfur

The sulfur composition of orogenic gold deposits varies widely with $\delta^{34}S$ values as low as -20 ‰ and as high as +25 ‰ (Goldfarb and Groves, 2015); most deposits show a sulfur isotopic composition of 0 to +10 ‰ (Kerrich, 1987; Golding et al., 1990, Nesbitt, 1991). This range is attributed either to the metasedimentary and/or metavolcanic rocks from which the fluids originated or a magmatic component including mantle and/or lamprophyres (e.g., Kontak et al., 1990; Kontak and Kyser, 1995; Goldfarb et al., 2007; Zacharias et al., 2013, 2014; Groves and Santosh, 2015). Therefore, the sulfur isotopic composition of sulfides in orogenic gold deposits can provide information about the source region of sulfur and metals found in mineralized veins. Today, the most accepted sulfur source for Phanerozoic orogenic gold deposits are metamorphic fluids formed by the devolatilization of either fine-grained, reduced sediments or mafic rocks (e.g., Pitcairn et al., 2006; Philips and Powel, 2010; Tomkins, 2010; Yardley and Cleverley, 2015).

Sulfur isotopic composition of sulfides in mineralized veins at Hog Mountain show two distinct populations with values of 7.7 ± 0.9 ‰ (Group 1) for Au-bearing quartz veins and 12.9 ± 1.4 ‰ (Group 2) for barren arsenopyrite veinlets and base metal mineralization on mono-mineralic quartz vein-tonalite contacts. The values of Group 1 overlap with $\delta^{34}S$ values of pyrrhotite ($\delta^{34}S$ = 9.0 and 9.9 ‰) reported by Stowell et al. (1996). The same authors measured the sulfur isotopic composition for unaltered tonalite and the surrounding phyllites of the Wedowee Group with values of 10.2 to 11.3 ‰ and 18.6 ‰, respectively. They concluded that the fluid source for

pyrrhotite at Hog Mountain were the metasedimentary rocks of the Wedowee Group with a potential input from the tonalitic wall rock. The metasedimentary rocks of the Wedowee Group are also the assumed sulfur source in this study because (1) the tonalite is several tens of million years older than the quartz veins and in relative equilibrium with the fluids, subduing an isotopic exchange and (2) the tonalite is spatially limited whereas mineralized quartz veins are laterally and vertically extensive with coeval gold mineralization also occuring in Wedowee phyllites of the adjacent Goldville district. The range in sulfur isotopic composition is instead explained by changes in the redox state of the hydrothermal fluid depositing pyrrhotite, pyrite, and chalcopyrite with Bi-Te-Au phases. The sulfur isotopic composition of Group 2 sulfides is restricted to vein textures that are the minority within the tonalite: massive arsenopyrite veinlets crosscut by minor pyrrhotite-chalcopyrite and chalcopyrite-sphalerite-galena mineralization on contacts between tonalite and mono-mineralic quartz veins. Both styles are barren of gold and assumingly formed at a late stage by lower temperature, more acidic hydrothermal fluids. Despite the higher $\delta^{34}S$ values of arsenopyrite and pyrrhotite in these vein textures compared to the predominant Group 1 mineral assemblage, metasedimentary rocks are also attributed to be the sulfur source for Group 2 sulfides. These higher values are explained by more oxidized fluid conditions and the lack of any viable source (e.g., meteoric water) that could have affected the sulfur isotopic composition. The estimated deposition depth of the veins was too deep for significant infiltration of meteoric water at the time of mineralization and neither the tonalite nor the veins show pervasive weathering.

Pitcairn et al. (2006) and Tomkins (2010) both showed that S liberated via devolatilization of fine-grained turbidites at the brittle-ductile transition (greenschist to amphibolite facies conditions) is the predominant, if not sole, sulfur source for orogenic gold deposits hosted in metasedimentary terranes. Sulfur in these metasedimentary source rocks originated from the

break-down of Fe-sulfides formed syngenetic within the metasedimentary rocks upon sedimentation and diagenesis (Tomkins et al., 2010). Goldfarb et al. (1997) and Chang et al. (2008) pointed out that the sulfur isotopic composition of Phanerozoic sediment-hosted orogenic gold deposits is a function of time. Sediment-hosted orogenic gold deposits commonly have $\delta^{34}S$ values that are 15 ‰ on average lighter than seawater sulfate at the time of sediment deposition (Chang et al., 2008; Fig. 2.14). Seawater, therefore, was postulated as the original sulfur source for diagenetic pyrite in the sediments that provided hydrothermal fluids for orogenic gold deposits via devolatilization at moderate metamorphic conditions.

In Figure 2.14, the sulfur isotopic composition of this study is compared to other orogenic deposits and RIRG deposits worldwide. Hog Mountain weakly overlaps with the proposed $\delta^{34}S$ curve (light grey) for sediment-hosted orogenic gold deposits at the time of phyllite sedimentation in the Middle Ordovician. This is because the curve of Chang (2008) is solely based on selected sediment-hosted deposits and shows variations of > 25 ‰ from the original seawater sulfate curve of Claypool et al. (1980; medium grey curve on right), especially in the early to middle Paleozoic. Orogenic gold deposits hosted in igneous rocks (Mokrsko and Jilové deposits) have $\delta^{34}S$ values that are generally between 0 to 10 ‰ and overlap with the results of this study. Despite the overlap of $\delta^{34}S$ values of sulfides from Hog Mountain with both sediment-hosted and igneous-rock hosted orogenic gold deposits (Fig. 2.14), the regional geology (dominant metasedimentary rocks, coeval gold mineralization in the adjacent Goldville district) favors strongly the input of S from the Middle Ordovician metasedimentary rocks of the Wedowee Group over the small, reduced Hog Mountain tonalite. Sulfur isotopic compositions of RIRG deposits strongly resemble a magmatic sulfur composition or is even lighter; a magmatic sulfur source has been proposed for this deposit

type (Goldfarb et al., 2005; Hart, 2007). Values of > 0‰ in RIRG deposits are usually attributed to several sulfur sources including sediments of the wall rock (Kontak and Kyser, 2011).

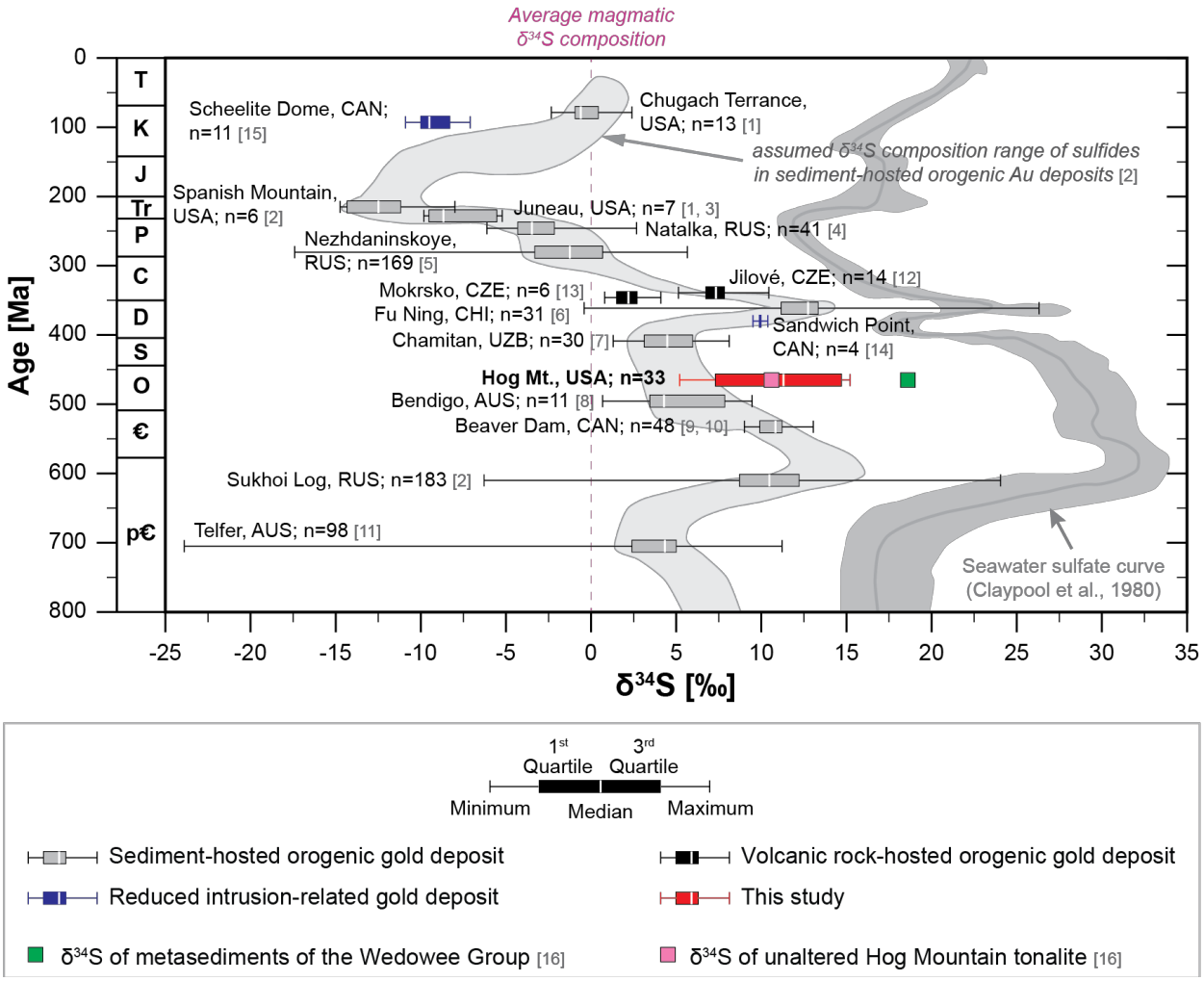

Figure 2.14. Sulfur isotopic composition of orogenic gold deposits and RIRG deposits over geologic time. Sediment-hosted orogenic gold deposits mimic the seawater sulfate curve of Claypool et al. (1980; medium grey curve on right) by a difference of 10-30 ‰ (light grey curve in center). Sulfides from Hog Mountain are plotted at the time of sediment deposition (phyllite formation) in the Middle Ordovician since they are the sulfur source for the mineralization in the later formed quartz veins. Igneous rock-hosted orogenic deposits commonly have $\delta^{34}S$ values < 10‰, whereas RIRG deposits are close to or < 0 ‰. Note: Sandwich Point (RIRG) has a contamination of magmatic derived fluids with surrounding metasedimentary rocks resulting in more positive values. The dashed magenta line depicts average magmatic $\delta^{34}S$. Modified from Chang et al. (2008). **References:** [1] Goldfarb et al. (1997), [2] Chang et al. (2008), [3] Goldfarb et al. (1991), [4] Eremin et al. (1994), [5] Bortnikov et al. 1998, [6] Cromie and Zaw (2003), [7] Bortnikov et al. 1996, [8] Bierlein, 2004; [9] Kontak and Smith, 1989, [10] Sangster (1992), [11] Rowins et al. (1996), [12] Zachariáš et al. (2013), [13] Zachariáš et al. (2014), [14] Kontak and Kyser (2011), [15] Mair et al. (2006), [16] Stowell et al. (1996). **Abbreviations:** AUS – Australia, CAN – Canada, CHI – China, CZE – Czech Republic, n – number of analyses, RUS – Russia, USA – United States of America, UZB – Uzbekistan.

2.7.4.2 Metals

Deciphering the origin of metals, and especially gold, in hydrothermal ore deposits has important genetic and exploration implications. In orogenic gold deposits, sulfur and metals are assumed to have the same origin even if metals of the epithermal suite (Ag, As, Bi, Hg, Sb, Se, Te) are present (Pitcairn et al., 2006; Goldfarb and Groves, 2015); metals of the epithermal suite and Au are commonly assigned to a magmatic origin (i.e., mantle, dikes, intrusion) in hydrothermal ore deposits (e.g., Sillitoe et al., 1996; Heinrich and Candela, 2013). However, Goldfarb et al. (2005) pointed out that metal leaching is not a common process for ascending hydrothermal fluids and the role of intrusions adjacent to or hosting orogenic gold deposits is highly debated (e.g., Kerrich, 1983, 1991; Goldfarb et al., 2005; Goldfarb and Groves, 2015 and references therein). In the mass balance model applied to purely sediment-hosted orogenic gold deposits in the Otago and Alpine schists of New Zealand, Pitcairn et al. (2006) showed that metasedimentary source rocks could provide the amount of epithermal suite metals observed in orogenic gold deposits of this region via devolatilization during prograde greenschist to amphibolite facies metamorphism. Törmänen and Koski (2005) hypothesized that elevated Bi concentrations in the massive sulfide deposit of the Escanaba Trough, East Pacific are related to overlying sediments that may have provided the Bi. Large et al. (2011) showed that diagenetic pyrite within turbidites can incorporate a wide range of metals including Te, which is then released into hydrothermal fluids upon the breakdown of pyrite under greenschist to amphibolite facies conditions. Therefore, metasedimentary source rocks that provided S during pyrite breakdown under prograde metamorphic conditions are also the probable source for metals such as Au, Bi, Te, As, Sb, and Ag in orogenic gold deposits, including Hog Mountain.

2.7.5 Genesis of the Hog Mountain Gold Deposit

The formation of orogenic gold deposits in the southernmost Appalachians within the EBR including the mineralized quartz veins at Hog Mountain are closely tied to: (1) sedimentation of deep-water turbidites in the Middle Ordovician in the peri-Laurentian realm; (2) the intrusion of tonalitic melts into the Middle Ordovician sediments during the Neoacadian orogeny; and (3) metamorphism/deformation during the Pennsylvanian-Permian Alleghanian orogeny. The turbiditic sediments provided the sulfur and metals whereas the tonalite performed as a physical trap for ascending ore-forming fluids rather than a source of sulfur or metals. During the Alleghanian orogeny, the peri-Laurentian realm with Blue Ridge and Inner Piedmont was thrusted upon the eastern Laurentian margin. During this latter event, the turbiditic sediments of the EBR were metamorphosed and devolatilized during prograde greenschist to amphibolite facies conditions along the brittle-ductile boundary. The released hydrothermal S- and metal-transporting fluids ascended under retrograde greenschist to amphibolite facies conditions as reduced, nearly neutral, relatively H_2S- and CO_2-rich, low saline fluids with respectable f_{Te2}. The fluids travelled along pre-existing faults and deposited metals at upper crustal levels within the tonalite during one continuous fluid event. Base metal precipitation may have been caused by fluid – wall rock interaction; however, Au precipitated via scavenging by Bi(±Te) melts that formed directly from the fluids at temperatures above their melting point (> 271˚C) due to the instability of Bi-transporting $Bi_2S_2(OH)$-complex. The Bi-Te-Au droplets were then remobilized during vein crystallization along and within quartz and pyrrhotite. Late stage, weakly oxidized, more acidic, moderately saline fluid deposited sphalerite-galena-chalcopyrite ± pyrrhotite as trace veins at tonalite – mono-mineralic quartz vein contacts with $\delta^{34}S$ compositions slightly higher than the

main fluid event. This final fluid event was minor and represents the fast-waning stage of the hydrothermal system at Hog Mountain.

The orogenic gold deposit at Hog Mountain formed during crustal thickening of an allochthonous terrane similar to the formation of orogenic gold deposits in Alaska (e.g. Juneau; Goldfarb et al., 1997), in the Meguma Province (e.g. Beaver Dam; Kontak and Smith, 1993) and the Bohemian Massif (e.g. Mokrsko deposit; Zacharias et al., 2014) during collisional orogenies.

2.8 Conclusions

The mineralized quartz veins at Hog Mountain were investigated for their mineralogy, mineral chemistry, and stable isotope geochemistry to constrain ore assemblage, hydrothermal fluid conditions, sources of both sulfur and metals, and genesis. Additionally, the classification of Hog Mountain as orogenic gold deposit was re-evaluated. The following conclusions are supported by this multi-faceted study.

- The ore mineral assemblage within the mineralized quartz veins (pyrrhotite – pyrite – chalcopyrite – arsenopyrite ± sphalerite ± galena ± native bismuth – hedleyite – 'unnamed Bi_3Te phase' ± bismuthinite ± native gold – electrum with <10 wt% Ag ± maldonite ± hessite) deposited from reduced, nearly neutral, relatively H_2S- and CO_2-rich, low saline fluids with relatively high f_{Te2} at 400-200 ºC at upper crustal levels. Late stage, slightly more reduced, acidic, moderately saline, low temperature fluids deposited the majority of sphalerite, galena, and hessite present at tonalite – mono-mineralic vein contacts.

- Sulfur and metals originated from the metasedimentary rocks in which the tonalite intruded via devolatilization and pyrite break down at prograde greenschist to amphibolite facies conditions. Metal leaching from the tonalite or an external fluid source is excluded.
- Gold precipitation occurred via scavenging by Bi(±Te) melts that formed directly from the reduced fluids at T > 271 ºC almost during the entire duration of the active hydrothermal system. Droplets were remobilized syngenetic along micro-cracks in pyrrhotite, within quartz and along quartz grain boundaries. Sulfides formed from late stage, low temperature fluids and incorporated Bi±Au in their lattice; no Au precipitation occurred.
- Despite being hosted in a reduced intrusion and having a Bi-Te-Au assemblage, Hog Mountain is an orogenic gold deposit.
- The formation of mineralized quartz veins at Hog Mountain is related to the Alleghanian orogeny and the closure of the Rheic Ocean, which resulted in the formation of Pangea. The collisional nature under which Hog Mountain formed is consistent with well documented observations in other orogenic gold deposits hosted in Phanerozoic metasedimentary and meta-igneous rocks.

References

Afifi, A.M., Kelly, W.C., and Essene, E.J., 1988a, Phase relations among tellurides, sulfides and oxides: I. Thermochemical data and calculated equilibria: Economic Geology, v. 83, p. 377-394.

Afifi, A.M., Kelly, W.C., and Essene, E.J., 1988b, Phase relations among tellurides, sulfides and oxides: II. Applications to telluride-bearing ore deposits: Economic Geology, v. 83, p. 395-404.

Ahlrichs, J.W., 1982a, Petrographic examination of selected surface samples from the Hog Mountain area, Alabama: Newmont Exploration Limited, Unpublished Memorandum, 9 p.

Ahlrichs, J.W., 1982b, Petrographic examination of specimens from the Hog Mountain gold project and toward the Dutch Bend mine, Alabama: Newmont Exploration Limited, Unpublished Memorandum, 12 p.

Ahlrichs, J.W., 1983, Petrographic examination of two drill core specimens from hole HM-1 at the Hog Mountain gold prospect, Alabama: Newmont Exploration Limited, Unpublished Memorandum, 7 p.

Aleinikoff, J.N., Zartman, R.E., Walter, M., Rankin, D.W., Lyttle, P.T., and Burton, W.C., 1995, U-Pb ages of metarhyolites of the Catoctin and Mount Rogers formations, central and southern Appalachians: Evidence for two phases of Iapetan rifting: American Journal of Science, v. 295, p. 428- 454.

Allard, G.O., and Whitney, J.A., 1994, Geology of the Inner Piedmont, Carolina Terrane, and Modoc Zone in northeast Georgia: Georgia Department of Natural Resources, Environmental Protection Division, Georgia Geological Survey, Project Report 20, 36 p.

Barton, Jr., P.B., and Bethke, P.M., 1987, Chalcopyrite disease in sphalerite: pathology and epidemiology: American Mineralogist, v. 72, p. 451-476.

Bierlein, F.P., Arne, D.C., and Cartwright, I., 2004, Stable isotope (C, O, S) systematics in alteration haloes associated with orogenic gold mineralization in the Victorian gold province, SE Australia: Geochemistry: Exploration, Environment, Analysis, v. 4, p. 191-211.

Blackburn, W.H., and Schwendeman, J.F., 1977, Trace-element substitution in galena: Canadian Mineralogist, v. 15, p. 365-373.

Böhlke, J.K., 1988, Carbonate-sulfide equilibria and "stratabound" disseminated epigenetic gold mineralization: A proposal based on examples from Alleghany, California, U.S.A: Applied Geochemistry, v. 3, p. 499-516.

Böhlke, J.K., 1989, Comparison of metasomatic reactions between a common CO_2–rich vein fluid and diverse wall rocks: Intensive variable, mass transfers, and Au mineralization at Alleghany, California: Economic Geology, v. 84, p. 291-327.

Bortnikov, N.S., Gamyanin, G.N., Alpatov, V.A., Naumov, V.B., Nosik, L.P., and Mironova, O.F., 1998, Mineralogo-geokhimicheskiye osobennosti i usloviya obrazovaniya Nezhdaninskogo mestorozhdeniya zolota (Sakha-Yakutiya, Rossiya). Mineralogical-geochemical features and formation conditions of the Nezhdaninskoye gold deposit, Sakha-Yakutia, Russia: Geologiya Rudnykh Mestorozhdeniy, v. 40, p. 137-156.

Bortnikov, N.S., Prokof'yev, V.Y., and Razdolina, N.V., 1996, Genezis zolotokvartsevogo mestorozhdeniya Charmitan (Uzbekistan). Genesis of Charmitan quartz gold ores, Uzbekistan: Geologiya Rudnykh Mestorozhdeniy, v. 38, p. 238-257.

Brown, I.J., and Nesbitt, B.E., 1987, Gold-copper-bismuth mineralization in hedenbergitic skarn, Tombstone Mountains, Yukon: Canadian Journal of Earth Sciences, v. 24, p. 2362-2372.

Brueckner S.M., Piercey S.J., Layne G.D., and Piercey G., 2015, Variations of sulfur isotope signatures in sulfides from the metamorphosed Ming Cu(–Au) volcanogenic massive sulfide deposit, Newfoundland Appalachians, Canada: Mineralium Deposita, v. 50, p. 619-640.

Brueckner, S.M, Piercey, S.J., Pilote, J.-L., Layne, G.D., and Sylvester, P.J., 2016, Mineralogy and mineral chemistry of the metamorphosed and precious metal-bearing Min deposit, Canada: Ore Geology Reviews, v. 72, p. 914-939.

Chang, Z.-S., Large, R.R., and Maslennikov, V., 2008, Sulfur isotopes in sediment-hosted orogenic gold deposits—evidence for an early timing and a seawater sulfur source: Geology, v. 36, p. 971-974.

Clark, L. A., 1960, The Fe–As–S system: phase relations and applications: Economic Geology, v. 55, p. 1345-1381.

Clark, S.H.B., 2008, Geology of the Southern Appalachian Mountains: U.S. Geological Survey Scientific Investigations Map 2830, 1 two-sided sheet. https://pubs.usgs.gov/sim/2830/.

Claypool, G.E., Holser, W.T., Kaplan, I.R., Sakai, H., and Zak, I., 1980, The age curves of sulfur and oxygen isotopes in marine sulfate and their mutual interpretation: Chemical Geology, v. 28, p. 199-260.

Ciobanu, C.L., Cook, N.J., and Pring, A., 2005, Bismuth tellurides as gold scavengers, in Mao, J., and Bierlein, F.P., eds., Mineral deposit research: Meeting the global challenge, Proceedings of the 8th Biennial SGA Meeting, Beijing, China, 18-21 August, 2005: Springer, p. 1383-1386, doi: 10.1007/3-540-27946-6_352.

Ciobanu, C.L., Birch, W.D., Cook, N.J., Pring, A., and Grundler, P.V., 2010, Petrogenetic significance of Au–Bi–Te–S associations: the example of Maldon, Central Victorian gold province, Australia: Lithos, v. 116, p. 1-17.

Cockerton, A.B.D., and Tomkins, A.G., 2012, Insights into the liquid bismuth collector model through analysis of the Bi-Au Stormont skarn prospect, northwest Tasmania: Economic Geology, v. 107, p. 667-682.

Cook, N.J., and Ciobanu, C.L., 2004, Bismuth tellurides and sulfosalts from the Larga hydrothermal system, Metaliferi Mts., Romania: Mineralogical Magazine, v. 68, p. 301-321.

Cook, N.J., Ciobanu, C.L., Wagner, T. and Stanley, C.J., 2007, Minerals of the system Bi-Te-Se-S related to the tetradymite archetype: Review of classification and compositional variation: Canadian Mineralogist, v. 45, p. 665-708, doi: 10.2113/gscanmin.45.4.665.

Cook, N.J., Ciobanu, C.L., Pring, A., Skinner, W., Shimizu, M., Danyushevsky, L., Saini-Eidukat, B., and Melcher, F., 2009, Trace and minor elements in sphalerite: A LA-ICPMS study: Geochimica et Cosmochimica Acta, v. 73, p. 4761-4791, doi: 10.1016/j.gca.2009.05.045.

Craig, J.R., and Vokes, F.M., 1993, The metamorphism of pyrite and pyritic ores: An overview: Mineralogical Magazine, v. 57, p. 3-18.

Cromie, P.W., and Zaw, K., 2003, Geological setting, nature of ore fluids and sulfur isotope geochemistry of the Fu Ning Carlin-type gold deposits, Yunnan Province, China: Geofluids, v. 3, p. 133-143.

Czamanske, G.K., 1974, The FeS content of sphalerite along the chalcopyrite-pyrite-bornite sulfur fugacity buffer: Economic Geology, v. 69, p. 1328-1334.

DiBenedetto, F., Bernardini, G.P., Costagliola, P., Plant, D. and Vaughan, D.J., 2005, Compositional zoning in sphalerite crystals: American Mineralogist, v. 90, p. 1384-1392, doi:10.2138/am.2005.1754.

Douglas, N., Mavrogenes, J., Hack, A., and England, R., 2000, The liquid bismuth collector model: An alternative gold deposition mechanism [abs.]: Geological Society of Australia, Australian Geological Convention, 15th, Sydney, Abstracts, p. 135.

Dubé, B., Williamson, K., and Malo, M., 2003, Gold mineralization within the Red Lake mine trend: example from the Cochenour-Willams mine area, Red Lake, Ontario, with new key information from the Red Lake mine and potential analogy with the Timmins camp: Geological Survey of Canada, Current Research 2003-C21, 15 p.

Dubé, B., Williamson, K., McNicoll, V., Malo, M., Skulski, T., Twomey, T., and Sanborn-Barrie, M., 2004, Timing of gold mineralization in the Red Lake gold camp, northwestern Ontario, Canada: New constraints from U-Pb geochronology at the Goldcorp High-grade zone, Red Lake mine and at the Madsen mine: Economic Geology, v. 99, p. 1611-1641.

Ebert, S.W., Baker, T., and Spencer, R.J., 2003, Fluid inclusion studies at the Donlin Creek gold deposit, Alaska: Possible evidence for reduced porphyry-Au to sub-epithermal transition:

Society for Geology Applied to Mineral Deposits, Proceedings of the Seventh Biennial Meeting, Athens, August 24–28, p. 263-266.

Ebert, S., Miller, L., Petsel, S., Dodd, S., Kowalczyk, P., Tucker, T.L., and Smith, M.T., 2000, Geology, mineralization, and exploration at the Donlin Creek project, southwestern Alaska: British Columbia and Yukon Chamber of Mines, Special Volume 2, p. 99-114.

Elliot, R.P., 1965, Constitution of binary alloys: 1st supplement, New York, McGraw Hill, 877 p.

Eremin, R.A., Voroshin, S.V., Sidorov, V.A., Shakhtyrov, V.G. and Pristavko, V.A., 1994, Geology and genesis of the Natalka gold deposit, Northeast Russia: International Geology Review, v. 36, p. 1113-1138.

Fabricio-Silva, W., Rosière, C.A., and Brùhn, B., 2019, The shear zone-related gold mineralization at the Turmalina deposit, Quadrilátero Ferrífero, Brazil: structural evolution and the two stages of mineralization: Mineralium Deposita, v. 54, p. 347-368, doi: 10.1007/s00126-018-0811-7.

Foord, E.E., and Shawe, D.R., 1989, The Pb–Bi–Ag–Cu-(Hg) chemistry of galena and some associated sulfosalts — a review and some new data from Colorado, California and Pennsylvania: Canadian Mineralogist, v. 27, p. 363.

Frost, B.R., Mavrogenes, J.A., and Tomkins, A.G., 2002, Partial melting of sulfide deposits during medium- and high-grade metamorphism: Canadian Mineralogist, v. 40, p. 1-18.

Garofalo, P.S., Fricker, P.S., Gunther, M.B., Bersani, D., and Lotticci, P.P., 2014, Physical–chemical properties and metal budget of gold-transporting hydrothermal fluids in orogenic deposits, in Garofalo, P.S., and Ridley, J.R., eds., Gold-transporting

Hydrothermal Fluids in the Earth's Crust: Geological Society Special Publication 402, p. 71-102.

Gault, H.R., 1945, Petrography, structures, and petrofabrics of the Pinckneyville quartz diorite, Alabama: Geological Society of America Bulletin, v. 56, p. 181-246.

Goldfarb, R.J., and Groves, D.I., 2015, Orogenic gold: Common or evolving fluid and metal sources through time: Lithos, v. 233, p. 2-26.

Goldfarb, R.J., Leach, D.L., Pickthorn, W.J., and Paterson, C.J., 1988, Origin of lode-gold deposits of the Juneau gold deposit, southeast Alaska: Geology, v. 16, p. 440-443.

Goldfarb, R.J., Newberry, R.J., Pickthorn, W.J., and Gent, C.A., 1991, Oxygen, hydrogen, and sulfur isotope studies in the Juneau gold belt, southeastern Alaska: Constraints on the origin of hydrothermal fluids: Economic Geology, v. 86, p. 66-80.

Goldfarb, R.J., Miller, L.D., Leach, D.L., and Snee, L.W., 1997, Gold deposits in metamorphic rocks of Alaska: Economic Geology Monographs 9, p. 151-190.

Goldfarb, R.J., Ayuso, R., Miller, M.L., Ebert, S.W., Marsh, E.E., Petsel, S.A., Miller, L.D., Bradley, D., Johnson, C., and McClelland, W., 2004, The Late Cretaceous Donlin Creek deposit, southwestern Alaska-controls on epizonal formation: Economic Geology, v. 99, p. 643-671.

Goldfarb, R.J., Bake, T., Dubé, B., Groves, D.I., Hart, C.J.R., and Gosselin, P., 2005, Distribution, character, and genesis of gold deposits in metamorphic terranes: Economic Geology, 100th Anniversary Volume, p. 407-450.

Goldfarb, R.J., Hart, C.J.R., Davis, G., and Groves, D.I., 2007, East Asian gold—deciphering the anomaly of Phanerozoic gold in Precambrian cratons: Economic Geology, v. 102, p. 341-346.

Golding, S.D., Groves, D.I., McNaughton, N.J., Mikucki, E.J., and Sang, J.-H., 1990, Source of ore fluid and ore components—sulfur isotope studies: Geology Department and University Extension 20, University of Western Australia Publication, p. 259-262.

Groves, D.I., 1993, The crustal continuum model for late-Archaean lode-gold deposits of the Yilgarn Block, Western Australia: Mineralium Deposita, v. 28, p. 366-374.

Groves, D.I., and Santosh, M., 2015, The giant Jiaodong gold province: The key to a unified model for orogenic gold deposits?: Geoscience Frontiers, v. 73, p. 1-9, doi: 10.1016/j.gsf.2015.08.002.

Groves, D.I., Goldfarb, R.J., Gebre-Mariam, M., Hagemann, S.G., and Robert, F., 1998, Orogenic gold deposits: A proposed classification in the context of their crustal distribution and relationship to other gold deposit types: Ore Geology Reviews, v. 13, p. 7-27, doi: 10.1016/S0169-1368(97)00012-7.

Groves, D.I., Goldfarb, R.J., Robert, F., and Hart, C.J.R., 2003, Gold deposits in metamorphic belts: Overview of current understanding, outstanding problems, future research, and exploration significance: Economic Geology, v. 98, p. 1-29.

Green, N.L., and Lesher, C.M., 1989, Mineralogy and geochemistry of the Hog Mountain Pluton, Northern Alabama Piedmont: Alabama Geological Survey Bulletin, v. 136, p. 133-158.

Green, N.L., Sinha, A.K., and Lesher, C.M., 1987, Gold associated with retrograde shear zones: An Alleghanian episode of mineralization in the southern Appalachians: Geological Society of America, Abstracts with Programs, v. 21: A277.

Guthrie, G.M., and Dean, L., 1989, Geology of the New Site 7.5 Minute Quadrangle, Tallapoosa County and Clay County, Alabama: Geological Survey of Alabama Quadrangle Series Map 9, 41 p.

Guthrie, G.M., and Lesher, C.M., 1989, Geologic setting of lode gold deposits in the northern Piedmont and Brevard zone, Alabama: Alabama Geological Survey Bulletin, v. 136, p. 11-32.

Hannington, M.D., Poulson, K.H., Thompson, J.F.H., and Sillitoe, R.H., 1999, Volcanogenic gold in the massive sulfide environment: Reviews in Economic Geology, v. 8, p. 325-351.

Hart, C.J.R., 2005, Classifying, distinguishing and exploring for intrusion-related gold systems: The Gangue: Newsletter of the Geological Association of Canada Mineral Deposits Division, v. 87, p. 4-9.

Hart, C.J.R., 2007, Reduced intrusion-related gold systems, in Goodfellow, W.D., ed., Mineral deposits of Canada: A Synthesis of Major Deposit Types, District Metallogeny, the Evolution of Geological Provinces, and Exploration Methods: Geological Association of Canada, Mineral Deposits Division, Special Publication No. 5, p. 95-112.

Hart, C.J.R., and Goldfarb, R.J., 2005, Distinguishing intrusion-related from orogenic gold systems: Proceedings of the 2005 New Zealand Minerals Conference, Auckland, November 13–16, p. 125-133.

Hart, C.J.R., McCoy, D., Goldfarb, R.J., Smith, M., Roberts, P., Hulstein, R., Bakke, A.A., and Bundtzen, T.K., 2002, Geology, exploration and discovery in the Tintina gold province, Alaska and Yukon: Society of Economic Geologists, Special Publication 9, p. 241-274.

Hatcher, R.D. Jr., 1972, Developmental model for the Southern Appalachians: Geological Society of America Bulletin, v. 83, 2735–2760. doi: 10.1130/0016-7606.

Hatcher, R.D. Jr., 1987, Tectonics of the southern and central Appalachian internides: Annual Reviews in Earth and Planetary Science, v. 5, p. 337-362.

Hatcher, R.D. Jr., 2002, Alleghanian (Appalachian) orogeny, a product of zipper tectonics: Rotational transpressive continent-continent collision and closing of ancient oceans along irregular margins: Geological Society of America Special Paper, v. 364, p. 199-208.

Hatcher, R.D. Jr., 2010, The Appalachian orogen: A brief summary: Geological Society American Memoir, v. 206, p. 1-19.

Hatcher, R.D. Jr., Acker, L.L., Bryan, J.G., and Godfrey, S.O., 1979, The Hayesville Thrust of the central Blue Ridge of North Carolina and nearby Georgia: A pre-metamorphic, poly-deformed thrust and cryptic suture within the Blue Ridge thrust sheet: Geological Society of America, Abstract with Programs, v.11, p. 181.

Hatcher, R.D. Jr., Bream, B.R., and Merschat, A.J., 2007, Tectonic map of the Southern and Central Appalachians: A tale of three orogens and a complete Wilson cycle, in Hatcher, R.D., Carlson, M.P., McBride, J.H., and Martínez Catalán, J.R., eds., 4-D Framework of Continental Crust, Geological Society of America Memoir v. 200, p. 595-632.

Heinrich, C.A., and Candela, P.A., 2013, Fluids and ore formation in the Earth's crust, in Holland, H., and Turekian, K., eds., Treatise on Geochemistry, v. 13, Elsevier Ltd., p. 29-57.

Heinrich, C.A., and Eadington, P. J., 1986, Thermodynamic predictions of the hydrothermal chemistry of arsenic, and their significance for the paragenetic sequence of some cassiterite-arsenopyrite-base metal sulfide deposits: Economic Geology, v. 81, p. 511-529, doi: 10.2113/gsceconfeo.81.3.511

Hibbard, J.P., 2004, The Appalachian orogeny, in van der Pluijm, B.A., and Marska, S., eds., Earth Structure, W.B Norton & Co. 2nd ed., p. 582-592.

Hibbard, J., van Staal, C., and Miller, B., 2007, Links between Carolinia, Avalonia, and Ganderia in the Appalachian peri-Gondwanan Realm, in Sears, J., Harms, T. and Evenchick, C., eds., Whence the Mountains? Inquiries into the Evolution of Orogenic Systems: A Volume in Honor of Raymond A. Price: Geological Society of America Special Paper, v. 433, p. 291-311, doi:10.1130/2007.2433(14).

Hibbard, J., van Staal, C.R. and Rankin, D.W., 2010, Comparative analysis of the geological evolution of the Northern and Southern Appalachian orogen: Late Ordovician–Permian, in Tollo, R.P., Bartholomew, M.J., Hibbard, J.P. and Karabinos, P.M., eds., From Rodinia to Pangea: The Lithotectonic Record of the Appalachian Region, Geological Society of America Memoir 206, p. 51-69.

Holm-Denoma, C.S., and Ras, R., 2010, Bimodal volcanism as evidence for Paleozoic extensional accretionary tectonism in the southern Appalachians: Geological Society of America Bulletin, v. 122, p. 1220-1234, doi: 10.1130/B30051.1.

Jébrak, M., and Marcoux, É., 2015, Geology of mineral resources: Mineral Deposits Division of the Geological Association of Canada, 668 p.

Klemm, D.D., 1965, Synthesen und Analysen in den Dreiecks-diagrammen FeAsS–CoAsS–NiAsS und FeS_2–CoS_2–NiS_2: Neues Jahrbuch Mineralogische Abhandlungen, v. 103, p. 205-255.

Kerrich, R., 1983, Geochemistry of gold deposits in the Abitibi Greenstone Belt: Canadian Institute of Mining and Metallurgy Special Volume 27, 75 p.

Kerrich, R., 1987, Stable isotope geochemistry of Au–Ag vein deposits in metamorphic rocks, in Kyser, T.K., ed., Stable Isotope Geochemistry of Low Temperature Fluids: Mineralogical Association of Canada Short Course, v. 13, p. 287-336.

Kerrich, R., 1991, Mesothermal gold deposits: a critique of genetic hypotheses, in Robert, F., Sheahan, P.A., and Green, S.B., eds., Greenstone Gold and Crustal Evolution: Geological Association of Canada, NUNA Conference Volume, p. 13-31.

Kontak, D.J., and Kerrich, R., 1995, Geological and geochemical studies of a metaturbidite-hosted lode gold deposit—the Beaver Dam deposit, Nova Scotia—II. Isotopic studies: Economic Geology, v. 90, p. 885-901.

Kontak, D.J., and Kyser, K., 2011, A fluid inclusion and isotopic study of an intrusion-related gold deposit (IRGD) setting in the 380 Ma South Mountain Batholith, Nova Scotia, Canada: evidence for multiple fluid reservoirs: Mineralium Deposita, v. 46, p. 337-363, doi: 10.1007/s00126-011-0331-1.

Kontak, D.J., and Smith, P.K., 1989, Sulfur isotopic composition of sulfides from the Beaver Dam and other Meguma-Group-hosted gold deposits, Nova Scotia: implications for genetic models: Canadian Journal of Earth Sciences, v. 26, p. 1617-1629.

Kontak, D.J., and Smith, P.K., 1993, A metaturbidite-hosted lode gold deposit: The Beaver Dam deposit, Nova Scotia. I. Vein paragenesis and mineral chemistry: The Canadian Mineralogist, v. 331, p. 471-522.

Kontak, D.J., Smith, P.K., Kerrich, R., and Williams, P.F., 1990, Integrated model for Meguma Group lode gold deposits, Nova Scotia, Canada: Geology, v. 18, p. 238-241.

Kontoniemi, O., and Ekdahl, E., 1990, Tonalite-hosted early Proterozoic gold deposit at Osikonmäki, southeastern Finland: Bulletin of the Geological Society of Finland, v. 62, p. 61-70, doi:10.17741/bgsf/62.1.003.

Kozdon, R., Kita, N. K., Huberty, J. M., Fournelle, J. H., Johnson, C. A. and Valley, J. W., 2010, *In situ* sulfur isotope analysis of sulfide minerals by SIMS: Precision and accuracy, with application to thermometry of ~3.5Ga Pilbara cherts. Chemical Geology, v. 275, p. 243-253, doi: 10.1016/j.chemgeo.2010.05.015.

Krouse, H.R., and Coplen, T.B., 1997, Reporting of relative sulfur isotope-ratio data: Pure and Applied Chemistry, v. 69, p. 293-295

Lang, J.R., and Baker, T., 2001, Intrusion-related gold systems: the present level of understanding: Mineralium Deposita, v. 36, p. 477-489.

Large, R.R., Bull, S.W., Maslennikov, V.V., 2011, A carbonaceous sedimentary source-rock model for Carlin-type and orogenic gold deposits: Economic Geology, v. 106, p. 331-358.

Lin, J.C., Sharma, R.C., and Chang, Y.A., 1996, The Bi–S (bismuth–sulfur) system: Journal of Phase Equilibria, v. 17, p. 132-139.

Lindgren, W., 1922, A suggestion for the terminology of certain mineral deposits: *Economic Geology*, v. 17, p. 292-294, doi:10.2113/gsecongeo.17.4.292.

Lindgren, W., 1933, Mineral Deposits. McGraw-Hill, New York, 4th edition, 196 p.

Lesher, C.M., Cook, R.B. and Dean, L.S., eds., 1989, Gold deposits of Alabama. Alabama Geological Survey Bulletin 136, 229 p.

Loucks, R.R., and Mavrogenes, J.A., 1999, Gold solubility in supercritical hydrothermal brines measured in synthetic fluid inclusions: Science, v. 284, p. 2159-2163, doi: 10.1126/science.284.5423.2159

Lydon, J.W., 1988, Volcanogenic massive sulfide deposits Part 2: Genetic models: Geoscience Canada, v. 15, p. 43-65.

Mair, J.L., Goldfarb, R.J., Johnson, C.A., Hart, C.J.R., and Marsh, E.E., 2006, Geochemical constraints on the genesis of the Scheelite Dome intrusion-related gold deposit, Tombstone gold belt, Yukon, Canada: Economic Geology, v. 10, p. 523-553.

Marshall, B., and Gilligan, L.B., 1987, An introduction to remobilization: Information from ore-body geometry and experimental considerations: Ore Geology Reviews, v. 2, p. 87-131, doi: 10.106/0169-1368(87)90025-4.

Marshall, B., Vokes, F.M., and Larocque, A.C.L., 1998, Regional metamorphic remobilization: Upgrading and formation of ore deposits: Reviews in Economic Geology, v. 11, p. 19-38.

Massey, M.A., and Moecher, D.P., 2005, Deformation and metamorphic history of the Western Blue Ridge–Eastern Blue Ridge terrane boundary, southern Appalachian Orogen: Tectonics, v. 24, TC5010, 18 p., doi: 10.1029/2004TC001643.

McClellan, E.A., Steltenpohl, M.G., Thomas, C. and Miller, C.F., 2007, Isotopic age constraints and metamorphic history of the Talladega Belt: New evidence for timing of arc magmatism and terrane emplacement along the southern Laurentian margin: The Journal of Geology, v. 115, p. 541-561, doi: 10.1086/519777.

McCuaig, T.C., and Kerrich, R., 1998, P-T-t-deformation-fluid characteristics of lode gold deposits: Evidence from alteration systematics: Ore Geology Reviews, v. 12, p. 381-454.

McDivitt, J.A., Kontak, D.J., Lafrance, B., and Robichaud, L., 2018, Contrasting fluid chemistries, alteration characteristics, and metamorphic timing relationships recorded in hybridized orebodies of the Missanabie-Renabie gold district, Archean Wawa subprovince, Ontario, Canada: Economic Geology, v. 113, p. 397-420, doi:10.5382/econgeo.2018.4555.

Meinert, L.D., 2000, Gold in skarns related to epizonal intrusions: Reviews in Economic Geology, v. 13, p. 347-375.

Mikucki, E.J., and Ridley, J.R., 1993, The hydrothermal fluid of Archaean lode-gold deposits at different metamorphic grades: Compositional constraints from ore and wallrock alteration assemblages: Mineralium Deposita, v. 28, p. 469-481.

Miller, B.V., Fetter, A.H., and Stewart, K.G., 2006, Plutonism in three orogenic pulses, Eastern Blue Ridge Province, southern Appalachians. Geological Society of America Bulletin, v. 118, p. 171-184, doi: 10.1130/B25580.1.

Morávek, P., 1971, Ore-deposits structure and mineralization of the Jílové goldmining district: Sb. Geol. Věd (Geol.), v. 13, p. 1–170.

Müller, W., Dallmeyer, R.D., Neubauer, F., and Thöni, M., 1999, Deformation-induced resetting of Rb/Sr and $^{40}Ar/^{39}Ar$ mineral systems in a low-grade, polymetamorphic terrane (Eastern

Alps, Austria): Journal of the Geological Society, v. 156, p. 261-278, doi: 10.1144/gsjgs.156.2.0261.

Mumin, A.H., Fleet, M.E., and Chryssoulis, S.L., 1994, Gold mineralization in As-rich mesothermal gold ores of the Bogosu-Prestea mining district of the Ashanti gold belt, Ghana—remobilization of "invisible" gold: Mineralium Deposita, v. 29, p. 445-460.

Murphy, J.B., and Nance, R.D., 2002, Sm–Nd isotopic systematics as tectonic tracers: an example from West Avalonia in the Canadian Appalachians: Earth Science Reviews, v. 59, p. 77-100.

Nekrasov, I.Y., 1996, Geochemistry, mineralogy and genesis of gold deposits: Brookfield, Vermont, A.A. Balkema, 329 p.

Nance, R.D., and Murphy, J.B., 1994, Contrasting basement isotopic signatures and the palinspastic restoration of peripheral orogens: example from the Neoproterozoic Avalonian–Cadomian belt: Geology, v. 22, p. 617-620.

Nance, R.D., and Murphy, J.B., 1996, Basement isotopic signatures and Neoproterozoic paleogeography of Avalonian–Cadomian and related terranes in the circum-North Atlantic, in: Nance, R.D., and Thompson, M.D., eds., Avalonian and Related Peri-Gondwanan Terranes of the Circum-North Atlantic, Geological Society of America Special Paper, v. 304, p. 333-346.

Nance, R.D., Guitiérrez-Alonso, G., Keppie, J.D., Linnemann, U., Murphy, J.B., Quesada, C., Strachan, R.A., and Woodcock, N.H., 2012, Evolution of the Rheic Ocean: Gondwana Research, v. 17, p. 194-222, doi:10.1016/j.gr.2009.08.001.

Neathery, T.L., and Reynolds, J.W., 1973, Stratigraphy and metamorphism of the Wedowee Group; a reconnaissance: American Journal of Science, v. 273, no. 8, p. 723-741.

Neathry, T.L., and Reynolds, J.W., 1975, Geology of the Lineville East, Ofelia, Wadley North and Mellow Valley quadrangles, Alabama: Alabama Geological Survey Bulletin 109, 120 p.

Nesbitt, B.E., 1991, Phanerozoic gold deposits in tectonically active continental margins, in Foster, R.P., ed., Gold Metallogeny and Exploration: Blackie and Sons Ltd., Glasgow, p. 104-132.

Nyquist, L. E., Wooden, J., Bansal, B., Wiesmann, H., McKay, G., and Bogard, D. D., 1979, Rb-Sr age of the Shergotty achondrite and implications for metamorphic resetting of isochron ages: Geochimica et Cosmochimica Acta, v. 43, p. 1057-1074.

Okamoto, H., and Massalski, T.B., 1983, The Au-Bi (gold-bismuth) system: Bulletin of Alloy Phase Diagrams, v. 4, p. 401-407.

Okamoto, H., and Tanner, L.E., 1990, Bi–Te (bismuth–tellurium), in Massalski, T.B., and Okamoto, H., eds., Binary Alloy Phase Diagrams. ASM International, Materials Park, Ohio, p. 800-801.

Park, C.F., 1935, Hog Mountain gold district, Alabama: Alabama Geological Survey, Miscellaneous Paper 90, 19 p.

Phillips, G.N., 1993, Metamorphic fluids and gold: Mineralogical Magazine, v. 57, p. 365-374.

Phillips, G.N., and Evans, K.A., 2004, Role of CO_2 in the formation of gold deposits: Nature, v. 429, p. 860-863.

Phillips, G.N., and Groves, D.I., 1984, Fluid access and fluid-wall rock interaction in the genesis of the Archaean gold-quartz vein deposit at Hunt mine, Kambalda, Western Australia, in

Foster, R. P., ed., Gold ’82—the geology, geochemistry and genesis of gold deposits: Rotterdam, Balkema, p. 389-416.

Phillips, G.N., and Powell, R., 1993, Link between gold provinces: Economic Geology, v. 88, p. 1084-1098.

Phillips, G.N., and Powell, R., 2010, Formation of gold deposits—a metamorphic devolatilization model: Journal of Metamorphic Geology, v. 28, p. 689-718.

Pitcairn, I.K., Teagle, D.A.H., Craw, D., Olivo, G.R., Kerrich, R., and Brewer, T.S., 2006, Sources of metals and fluids in orogenic gold deposits: Insights from the Otago and Alpine Schists, New Zealand: Economic Geology, v. 101, p. 1525-1546, doi:10.2113/gsecongeo.101.8.1525.

Pokrovski, G.S., Kokh, M.A., Guillaume, D., Borisova, A.Y., Gisquet, P., Hazemann, J.L., Lahera, E., Del Net, W., Proux, O., Testemale, D., Haigis, V., Joncheière, R., Seitsonen, A.P., Ferlat, G., Vuilleumier, R., Saitta, A.M., Boiron, M.C., and Dubessy, J., 2015, Sulfur radical species form gold deposits on Earth: Proceedings of the National Academy of Sciences, v. 112, p. 13484-13489.

Rankin, D.W., 1975, The Continental margin of eastern North America in the southern Appalachians: The opening and closing of the Proto-Atlantic ocean: American Journal of Science, v. 275, p. 298-336.

Reed, M.H., and Palandri, J., 2006, Sulfide mineral precipitation from hydrothermal fluids: Reviews in Mineralogy and Geochemistry, v. 61, p. 609-631.

Renock, D., and Becker, U., 2011, A first principles study of coupled substitution in galena: Ore Geology Reviews, v. 42, p. 71-83, doi: 10.1016/j.oregeorev.2011.04.001.

Ridley, J.R., and Diamond, L.W., 2000, Fluid chemistry of orogenic lode gold deposits and implications for genetic models: Reviews in Economic Geology 13, p. 141-162.

Romberger, S.B., 1986, The solution chemistry of gold applied to the origin of hydrothermal deposits: Canadian Institute of Mining and Metallurgy Special Volume 38, p. 168–186.

Rowins, S.M., Groves, D.I., McNaughton, N.J., Palmer, M.R., and Eldridge, C.S., 1996, A reinterpretation of the role of granitoids in the genesis of Neoproterozoic gold mineralization in the Telfer dome, Western Australia, Economic Geology, v. 92, p. 133-160.

Sangster, A.L., 1992, Light stable isotope evidence for a metamorphogenic orogen for bedding-parallel, gold-bearing veins in Cambrian flysch, Meguma Group, Nova Scotia: Exploration and Mining Geology, v. 1, p. 69-79.

Saunders, J., Steltenpohl, M., and Cokk, R.B., 2013, Gold exploration and potential of the Appalachian Piedmont of eastern Alabama: SEG Newsletter, v. 94, p. 1, 12-17.

Scott, S.D., and Barnes, H.L., 1971, Sphalerite geothermometry and geobarometry: Economic Geology, v. 66, p. 653-669.

Seward, T.M., 1973, Thio complexes of gold and the transport of gold in hydrothermal ore solution: Geochimica et Cosmochimica Acta, v. 37, p. 379-399.

Seward, T.M., 1976, The stability of chloride complexes of silver in hydrothermal solutions up to 350°C: Geochimica et Cosmochimica Acta, v. 40, p. 1329-1341.

Seward, T.M., 1984, The formation of lead(II) chloride complexes to 300°C: A spectrophotometric study: Geochimica et Cosmochimica Acta, v. 48, p. 121-134.

Seward, T.M., and Barnes, H.L., 1997, Metal transport by hydrothermal ore fluids, in Barnes, H. L., ed., Geochemistry of hydrothermal ore deposits, 3rd ed., New York, Wiley & Sons, p. 435-486.

Seward, T.M., Williams-Jones, A.E., and Migdisov, A.A., 2013, The Chemistry of Metal Transport and Deposition by Ore-Forming Hydrothermal Fluids, in Holland, H., and Turekian, K., eds., Treatise on Geochemistry, v. 13, Elsevier Ltd., p. 29-57.

Sha, P., and Lesher, C.M., 1990, Microthermometry of fluid inclusions in auriferous quartz veins, Goldville district, northern Piedmont, Alabama: Georgia Geological Survey Bulletin 117, p. 18-31.

Sillitoe, R.H., Hannington, M.D., and Thompson, J.F.H., 1996, High sulfidation deposits in the volcanogenic massive sulfide environment: Economic Geology, v. 91, p. 204-212.

Skirrow, R.G., and Walshe, J.L., 2002, Reduced and oxidized Au-Cu-Bi iron oxide deposits of the Tennant Creek inlier, Australia: An integrated geologic and chemical model: Economic Geology, v. 97, p. 1167-1202.

Smith, V.J., 2017, Tectonic evolution of the Wedowee and Emuckfaw Groups of the southern Blue Ridge of east central Alabama: Geological Society of America Southeastern Section Meeting, *Abstracts with Programs, v.* 49, doi: 10.1130/abs/2017SE-290991.

Stefánsson, A., and Seward, T.M., 2004, Gold(I) complexing in aqueous sulfide solutions to 500°C at 500 bar: Geochimica et Cosmochimica Acta, v. 68, p. 4121-4143.

Steltenpohl, M.G., ed., 2005, New perspectives on southernmost Appalachian terranes, Alabama and Georgia: Alabama Geological Society 42nd Annual Field Trip Guidebook, 212 p.

Stowell, H.H., and Lesher, C.M., 1990, Thermobarometry of synmetaomorphic gold deposits, Goldville district, northern Piedmont, Alabama: Georgia Geological Survey Bulletin 117, p. 1-17.

Stowell, H.H., Guthrie, G.M., and Lesher, C.M., 1989, Metamorphism and gold mineralization in the Wedowee Group, Goldville district, northern Piedmont, Alabama: Alabama Geological Survey Bulletin 136, p. 133-58.

Stowell, H.H., Lesher, C.M., Green, N.L., Sha, P., Guthrie, G.M., Sinha, A.K., 1996, Metamorphism and gold mineralization in the Blue Ridge, southernmost Appalachians: Economic Geology, v. 91, p. 1115-44.

Stowell, H., Parker, K.O., and Madden, J., 2015, Neoacadian and Alleghanian intrusion, metamorphism, and gold mineralization in the eastern Blue Ridge: Alabama Geological Society Field Trip Guide, 52nd Annual Field Trip December 10-12, 2015, 55 p.

Stuwe, K., 1998, Tectonic constraints on the timing relationships of metamorphism, fluid production and gold-bearing quartz vein emplacement: Ore Geology Reviews, v. 13, 219-228.

Strunz, H., and Nickel, E., 2001, Strunz Mineralogical Tables: Chemical Structural Classification System, 9th ed., Schweizerbart'sche Verlagsbuchhandlung, Stuttgart, Germany.

Thomas, W.A., 1991, The Appalachian-Ouachita rifted margin of southeastern North America: Geological Society America Bulletin, v. 103, p. 415-431.

Thompson, J.F.H., and Newberry, R.J., 2000, Gold deposits related to reduced granitic intrusions: Society of Economic Geologists Reviews 13, p. 377-400.

Tohver, E., van der Pluijm, B.A., Scandolâra, J.E., and Essene, E.J., 2005, Late Mesoproterozoic deformation of SW Amazonia (Rondônia, Brazil): Geochronological and structural evidence for collision with Southern Laurentia: The Journal of Geology, v. 113, p. 309-323, doi:10.1086/428807.

Tomkins, A.G., 2007, Three mechanisms of ore re-mobilization during amphibolite facies metamorphism at the Montauban Zn-Pb-Au-Ag deposit: Mineralium Deposita, v. 42, p. 627-637.

Tomkins, A.G., 2010, Window of metamorphic sulfur liberation in the crust: implications for gold deposit genesis: Geochimica et Cosmochimica Acta, v. 74, p 3246-3259.

Tomkins, A.G., and Mavrogenes, J.A., 2002, Mobilization of gold as a polymetallic melt during pelite anataxis at the Challenger deposit, southern Australia: A metamorphosed Archean gold deposit: Economic Geology, v. 97, p. 1249-1271.

Tomkins, A.G., Pattison, D.R.M., and Zaleski, E., 2004, The Hemlo gold deposit, Ontario: An example of melting and mobilization of a precious metal-sulfosalt assemblage during amphibolite facies metamorphism and deformation: Economic Geology, v. 99, p. 1063-1084.

Tomkins, A.G., Pattison, D.R.M., and Frost, B.R., 2007, On the initiation of anataxis: Journal of Petrology, v. 48, p. 511-535.

Tooth, B., Brugger, J., Ciobanu, C., and Liu, W., 2008, Modeling of gold scavenging by bismuth melts coexisting with hydrothermal fluids: Geology, v. 36, p. 815-818.

Tooth, B., Ciobanu, C.L., Green, L., O'Neill, B., and Brugger, J., 2011, Bi-melt formation and gold scavenging from hydrothermal fluids: An experimental study: Geochimica et Cosmochimica Acta, v. 75, p. 5423-5443, doi: 10.1016/j.gca.2011.07.020

Tòrmänen, T.O., and Koski, R.A., 2005, Gold enrichment and the Bi–Au association in pyrrhotite-rich massive sulfide deposits, Escanaba Trough, Southern Gorda Ridge: Economic Geology 100, p. 1135-1150.

Tull, J.F., 1978, Structural development of the Alabama Piedmont northwest of the Brevard zone: American Journal of Science, v. 278, p. 442–-460.

Tull, J.F, Barineau, C.I., Mueller, P.A., and Wooden, J.L., 2007, Volcanic arc emplacement onto the southernmost Appalachian Laurentian shelf: Characteristics and constraints. Geological Society America Bulletin, v. 119, p. 261-274, doi: 10.1130/B25998.1.

van Hook, H.J., 1960, The ternary system AgS_2–Bi_2S_3–PbS: Economic Geology, v. 55, p. 759-788.

van Staal, C.R., 2007, Pre-Carboniferous tectonic evolution and metallogeny of the Canadian Appalachians, in Goodfellow, W.D., ed., Mineral deposits of Canada: A synthesis of major deposit-types, district metallogeny, the evolution of geological provinces, and exploration methods: Geological Association of Canada, Mineral Deposits Division, v. 5, p. 793-818.

van Staal, C.R., and Barr, S.M., 2012, Lithospheric architecture and tectonic evolution of the Canadian Appalachians and associated Atlantic margin, in Percival, J.A., Cook, F.A., and Clowes, R.M., eds., Tectonic Styles in Canada: The LITHOPROBE perspective, Geological Association of Canada Special Paper 49, p. 41-95.

van Staal, C.R., Whalen, J.B., Valverde-Vaquer, P., Zagorevski, A., and N. Rogers, N., 2009, Pre-Carboniferous, episodic accretion-related, orogenesis along the Laurentian margin of the northern Appalachians: Geological Society Special Publication, v. 327, p. 271-316.

Voudouris, P.C., Spry, P.G., Mavrogonatos, C., Sakellaris, G.A., Bristol, S.K., Melfos, V., and Fornadel, A.P., 2013, Bismuthinite derivatives, lillianite homologues, and bismuth sulfotellurides as indicators for gold mineralization in the Stanos shear-zone related deposit, Chaldiki, northern Greece: Canadian Mineralogist, v. 51, p. 119-14, doi: 10.3749/canmin.51.1.119.

Wagner, S. L., Stewart, K. and Metcalf, K., 2012, Crustal-scale shortening structures beneath the Blue Ridge Mountains, North Carolina, USA: Lithosphere, v. 4, p. 242-256, doi: 10.1130/L184.1.

Wampler, J.M., Neathery, T.L., and Bentley, R.D., 1970, Age relations in the Alabama Piedmont, IN Bentley, R.D., and Neathery, T.L., eds., Geology of the Brevard fault zone and related rocks of the Inner Piedmont of Alabama: Alabama Geological Society Annual Field Trip Guidebook, December 4-5, 1970, no. 8, p. 81-90.

Whitmore, J.P., 2018, Geology of the Milltown Alabama 7.5" quadrangle and $^{40}Ar/^{39}Ar$ geochronology of muscovite from the rocks of the east central Alabama Piedmont: Unpublished M.Sc. thesis, Auburn University, 74 p.

Williams, H., 1979, The Appalachian orogeny in Canada: Canadian Journal of Earth Sciences, v. 16, p. 792-807.

Williams-Jones, A.E., Bowell, R.J., and Migdisov, A.A., 2009, Gold in solution: Elements, v. 5, p. 281-287.

Wood, S.A., and Samson, S.I., 1998, Solubility of ore minerals and complexation of ore metals in hydrothermal solutions, in Richards, J.P., and Larson, P.B., ed., Techniques in hydrothermal ore deposits geology: Reviews in Economic Geology 10, p. 33-80.

Wood, S.A., Crerar, D.A., and Borcsik, M.A., 1987, Solubility of the assemblage pyrite-pyrrhotite-magnetite-sphalerite-galena-gold-stibnite-bismuthinite-argentite-molybdenite in H_2O-NaCl-CO_2 solutions from 200º to 350ºC: Economic Geology, v. 82, p. 1864-1887.

Yardley, B.W., and Cleverley, J.S., 2015, The role of metamorphic fluids in the formation of ore deposits: Geological Society, London, Special Publications, v. 393, p. 117-134.

Yardley, B.W., and Graham, J.T., 2002, The origins of salinity in metamorphic fluids: Geofluids, v. 2, p. 249-256.

Zachariáš, J., Žák, K., Pudilová, M., and Snee, L.W., 2013, Multiple fluid sources/pathways and severe thermal gradients during formation of the Jílové orogenic gold deposit, Bohemian Massif, Czech Republic: Ore Geology Reviews, v. 54, p. 81-109, doi: 10.1016/j.oregeorev.2013.02.012.

Zachariáš, J., Morávek, P., Gadas, P., and Pertoldová, J., 2014, The Mokrsko-West gold deposit, Bohemian Massif, Czech Republic: Mineralogy, deposit setting and classification: Ore Geology Reviews, v. 58, p. 238-263, doi:10.1016/j.oregeorev.2013.11.005.

Appendix

Appendix A: Stratigraphic Columns and Gold Grades of Selected Drill Holes

Figure A.1. Stratigraphic sections of drill holes HM-58, HM-71, HM-83, HM-114, HM-122, and HM-130 showing the relationship between tonalite, cross-cutting veins, and older phyllite of the Wedowee Group. Veins show different degrees of mineralization (unmineralized, weakly mineralized and well mineralized) and dominantly contain quartz with traces of silicates ± calcite ± sulfides (vein class 2 after Stowell et al., 1989, 1996) or are mono-mineralic (vein class 1 after Stowell et al., 1989, 1996). Composite veins of quartz and carbonate ± silicates ± sulfides (vein classes 2 and 3 after Stowell et al., 1989, 1996) are rare. All of the following stratigraphic columns follow the legend below.

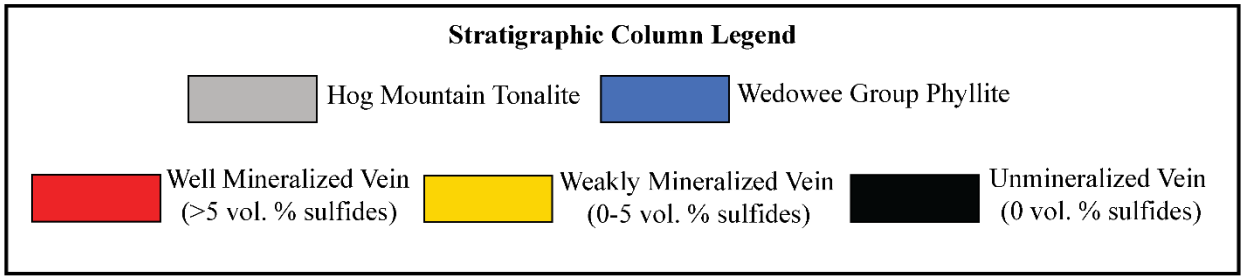

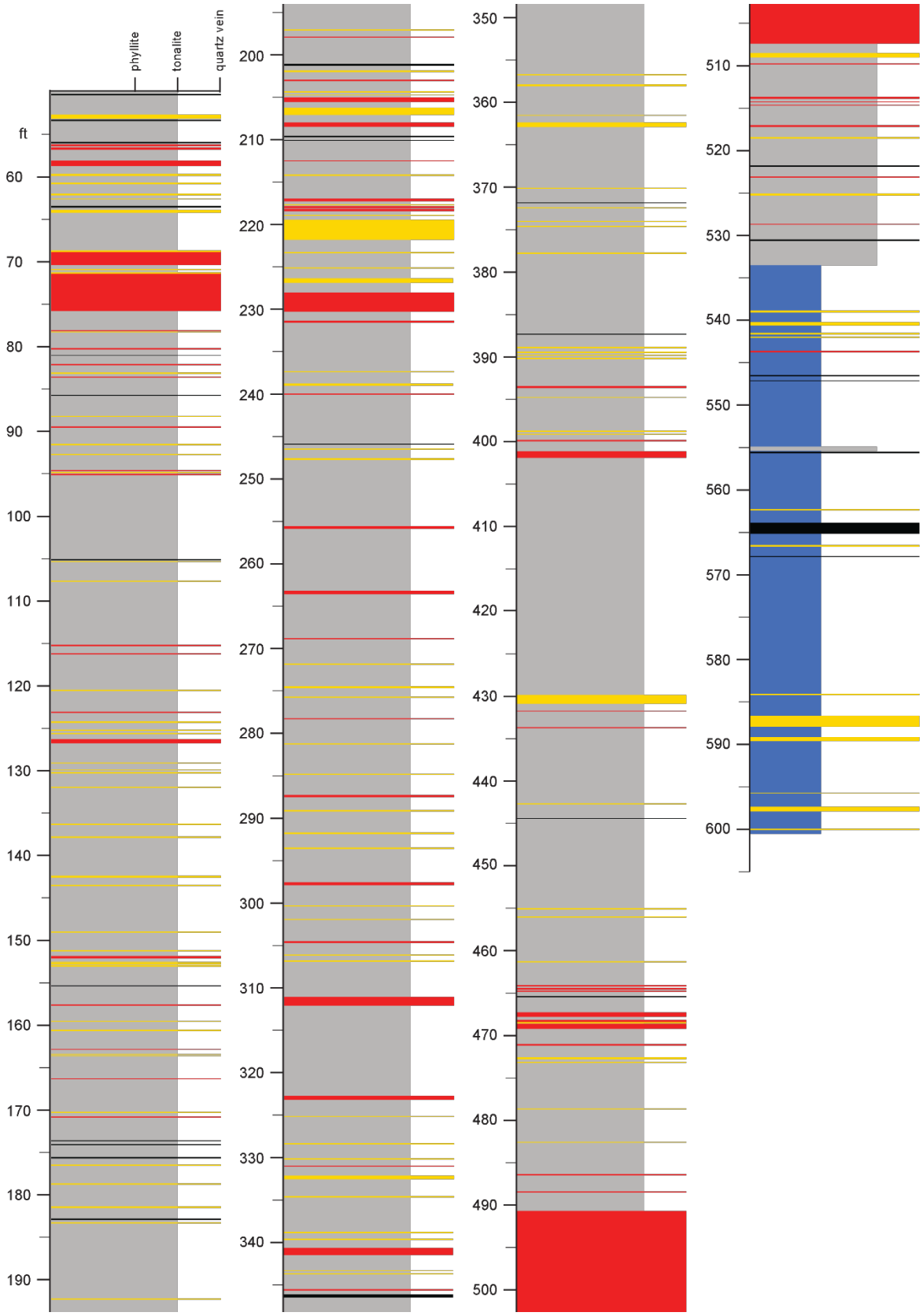

Figure A.1. (A) HM-58**.**

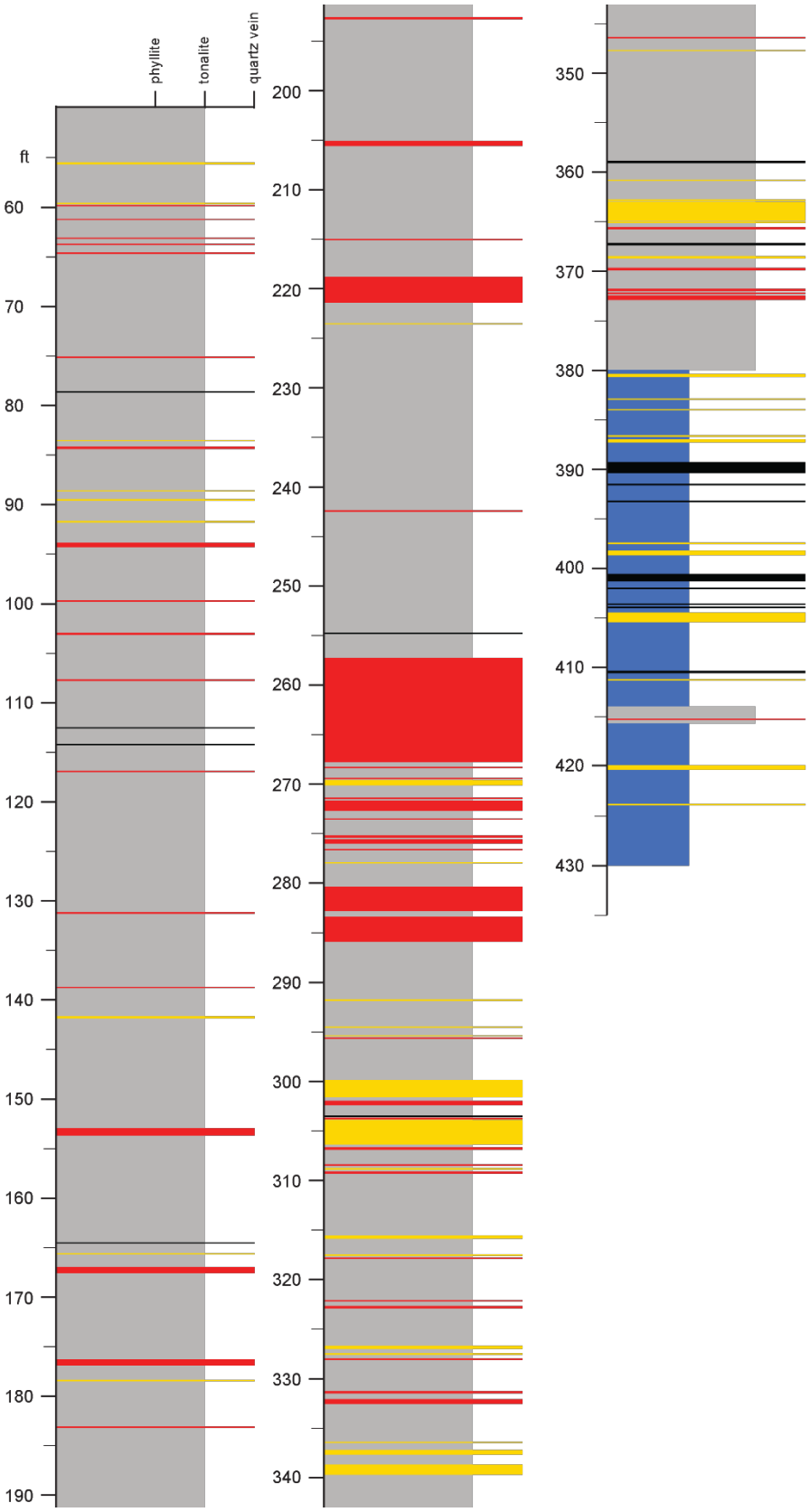

Figure A.1. *[continued]* **(B)** HM-71.

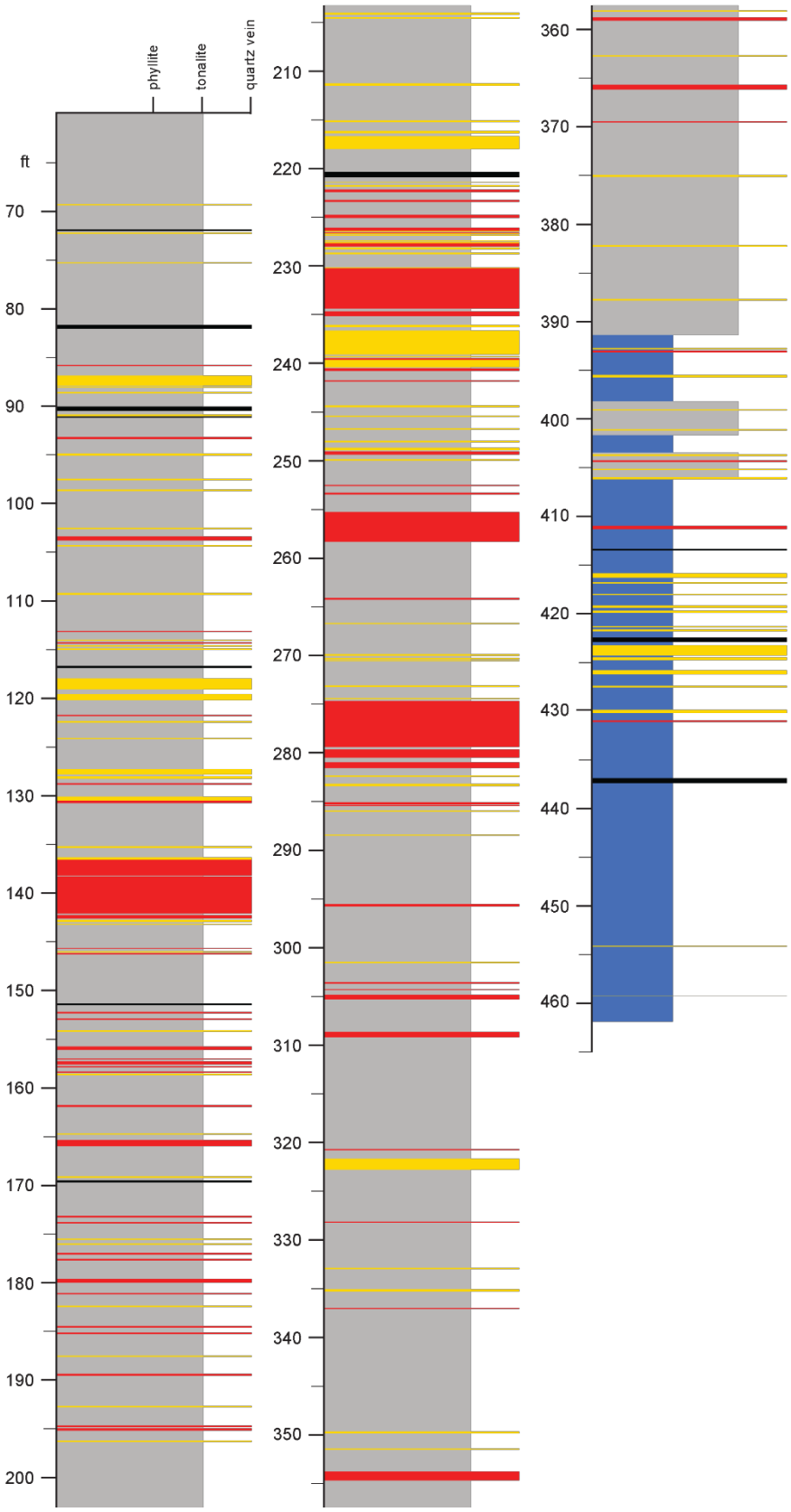

Figure A.1. *[continued]* **(C)** HM-83.

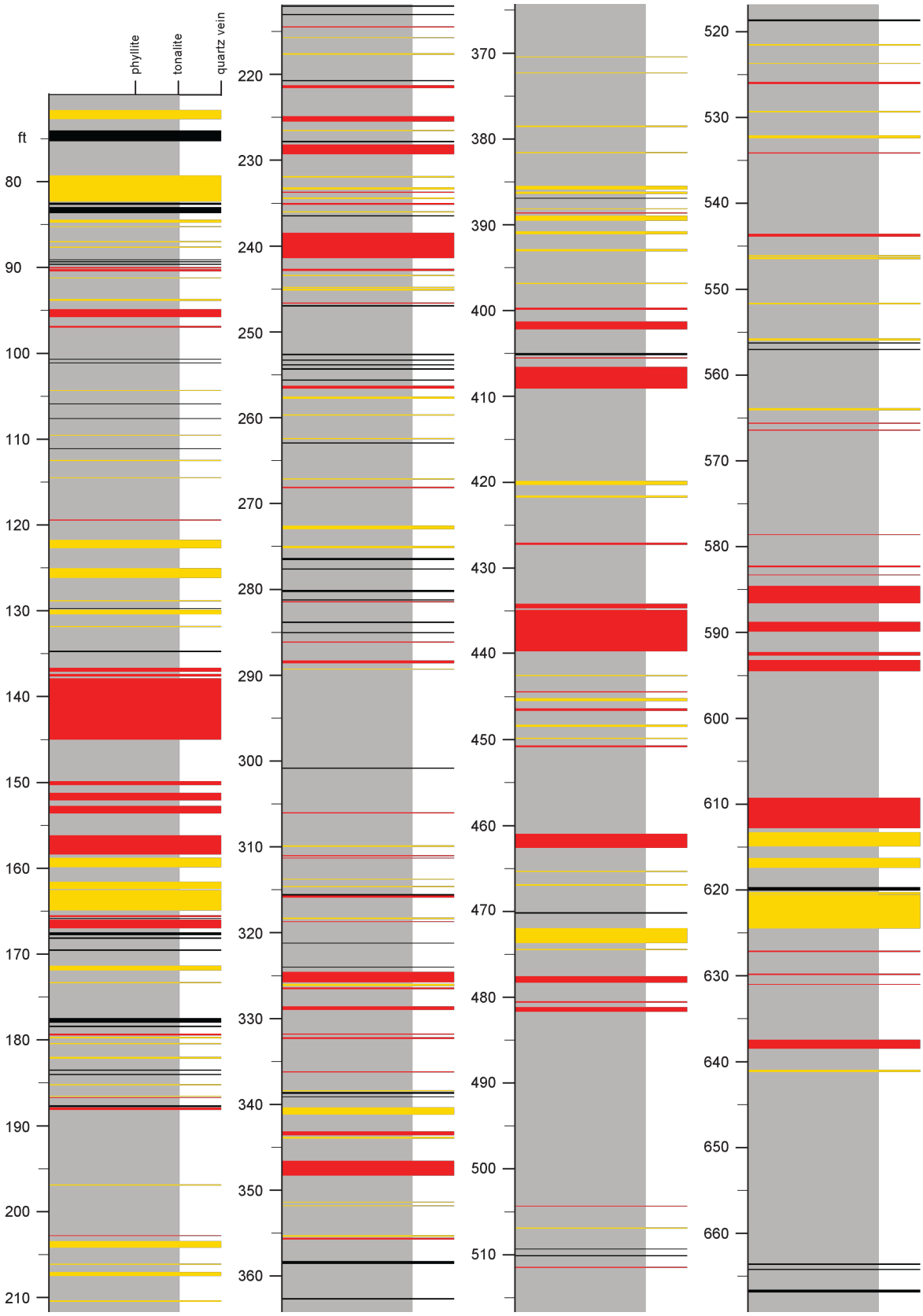

Figure A.1. *[continued]* **(D)** HM-114.

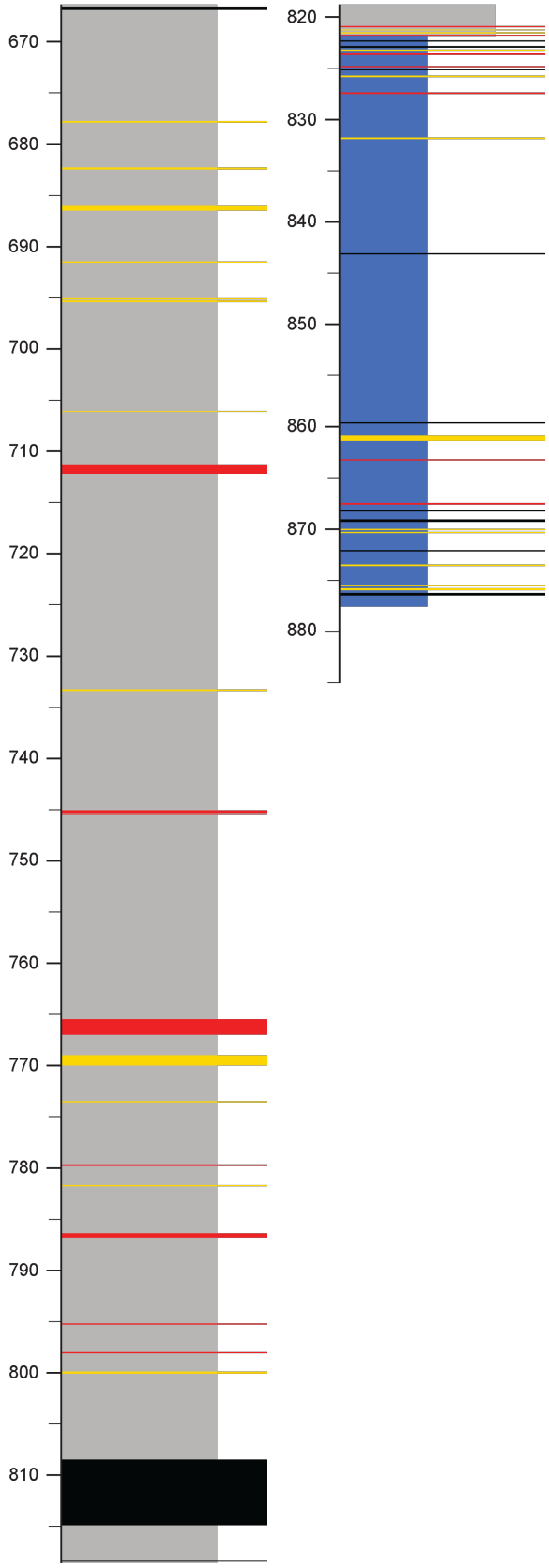

Figure A.1. *[continued]* **(D)** HM-114.

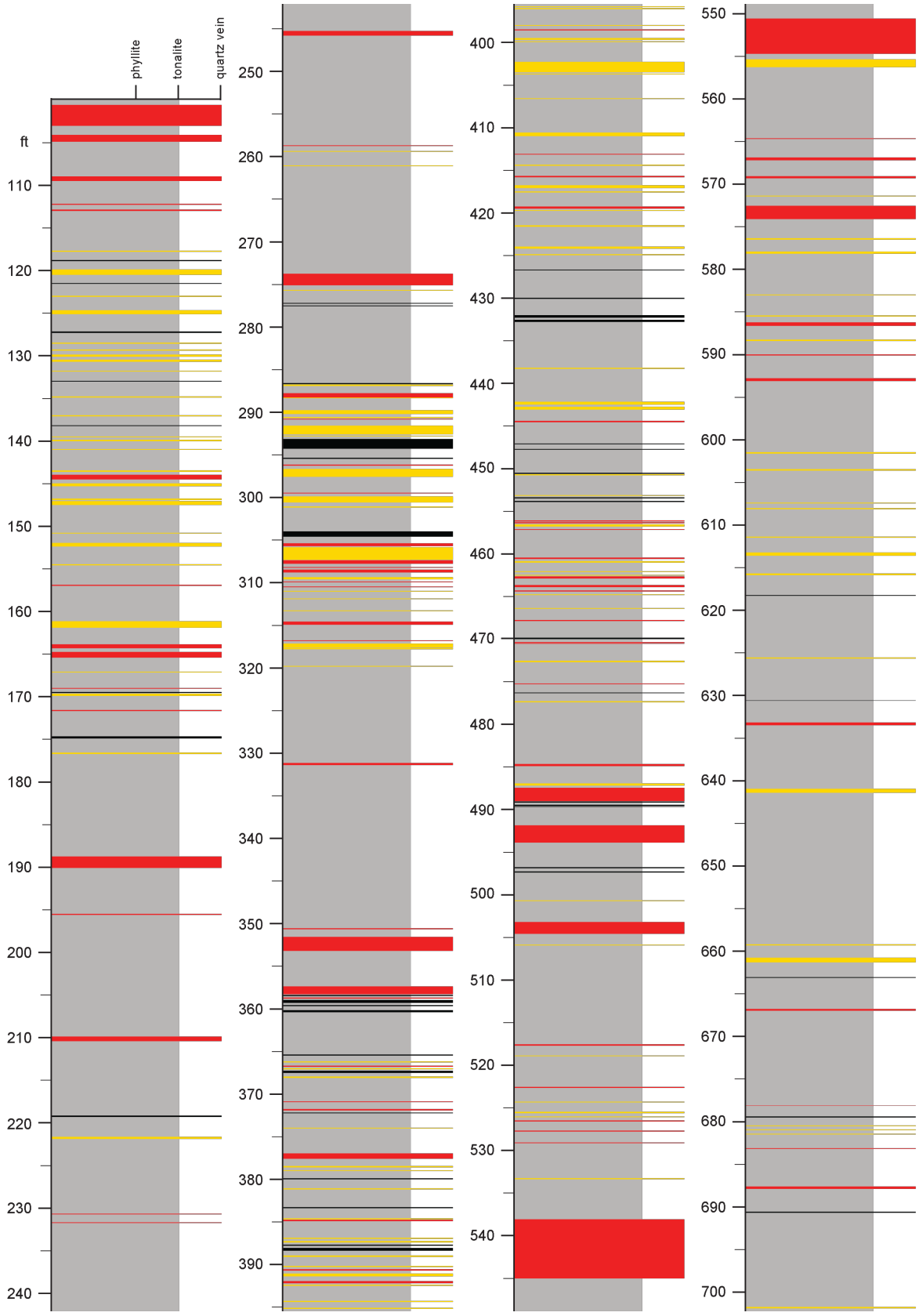

Figure A.1. *[continued]* **(E)** HM-122.

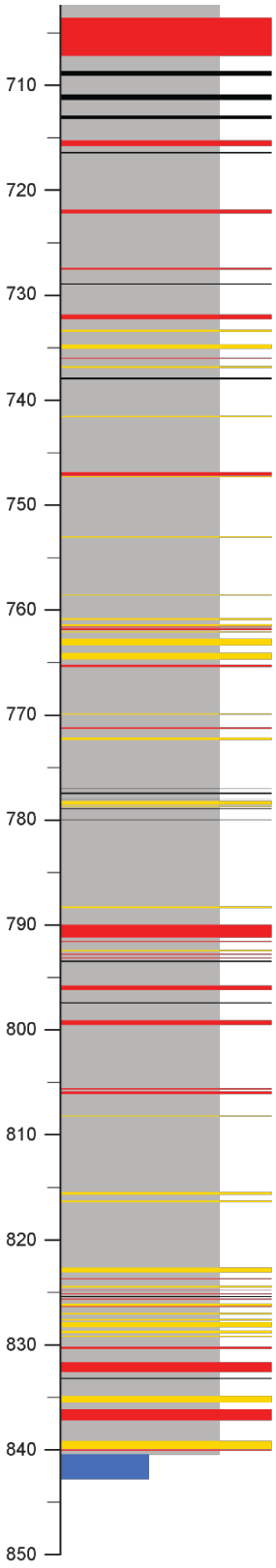

Figure A.1. *[continued]* **(E)** HM-122.

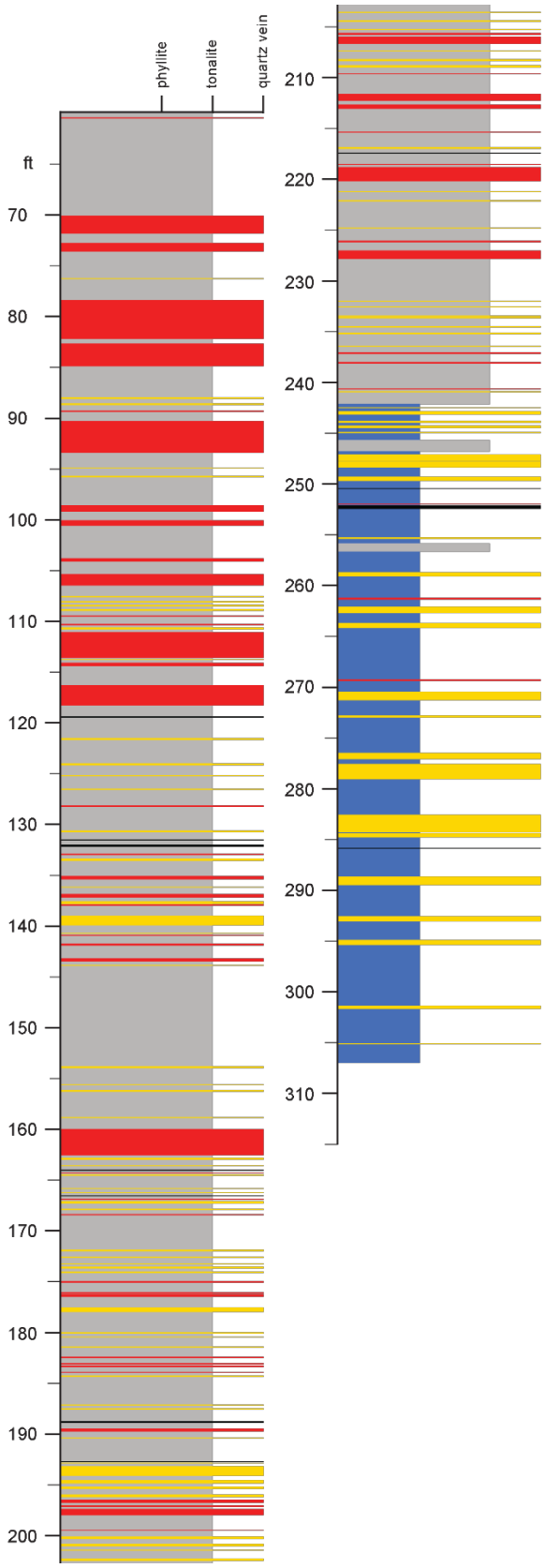

Figure A.1. *[continued]* **(F)** HM-130.

Table A.1. Average Au grades in oz/t for selected drill holes. Abbreviations: HM – Hog Mountain, Max – maximum value, MIN – minimum value, n – number of Analyses, oz/t – ounces per ton, Std – standard deviation. Data from Wellborn Mining LLC.

Drill hole	HM-58	HM-71	HM-83	HM-114	HM-122	HM-130
n	117	84	93	171	169	59
Average [oz/t]	0.02	0.04	0.02	0.04	0.02	0.07
Std	0.05	0.178	0.03	0.20	0.06	0.32
Min	0	0	0	0	0	0
Max	0.36	1.57	0.23	2.21	0.45	2.44

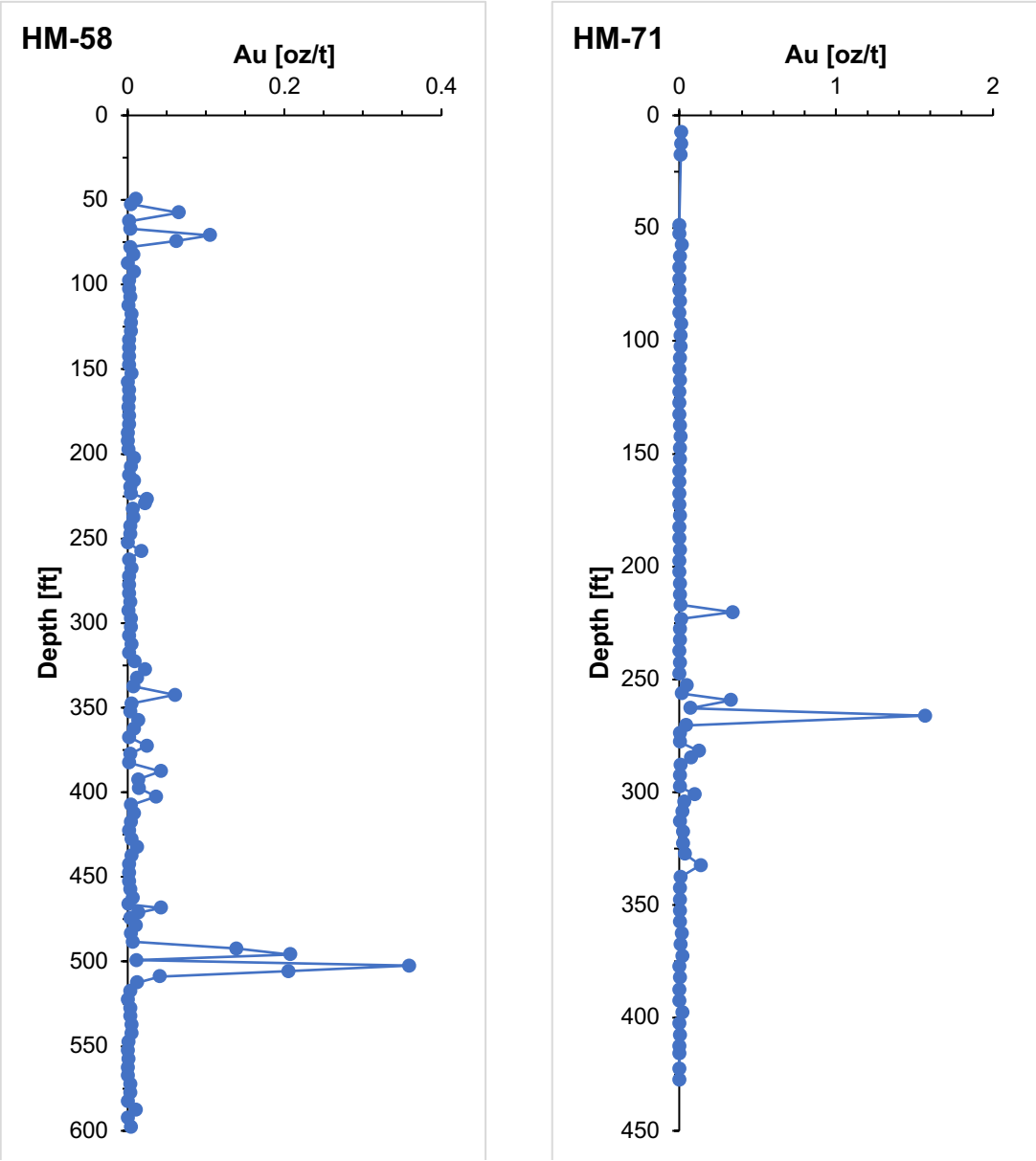

Figure A.2. Gold grade versus depth. HM-58 (left) and HM-71 (right).

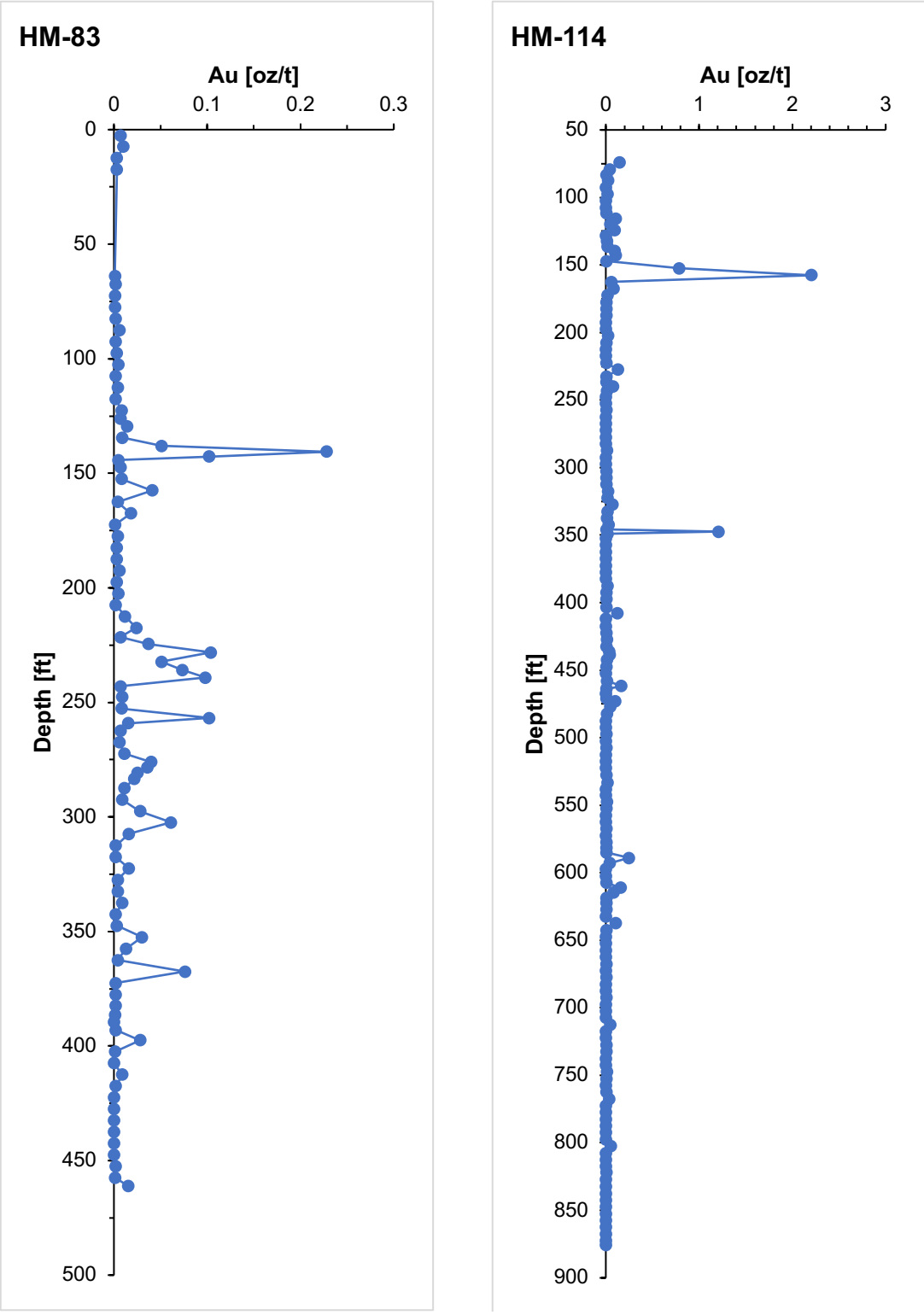

Figure A.2. *[continued]* HM-83 (left) and HM-114 (right).

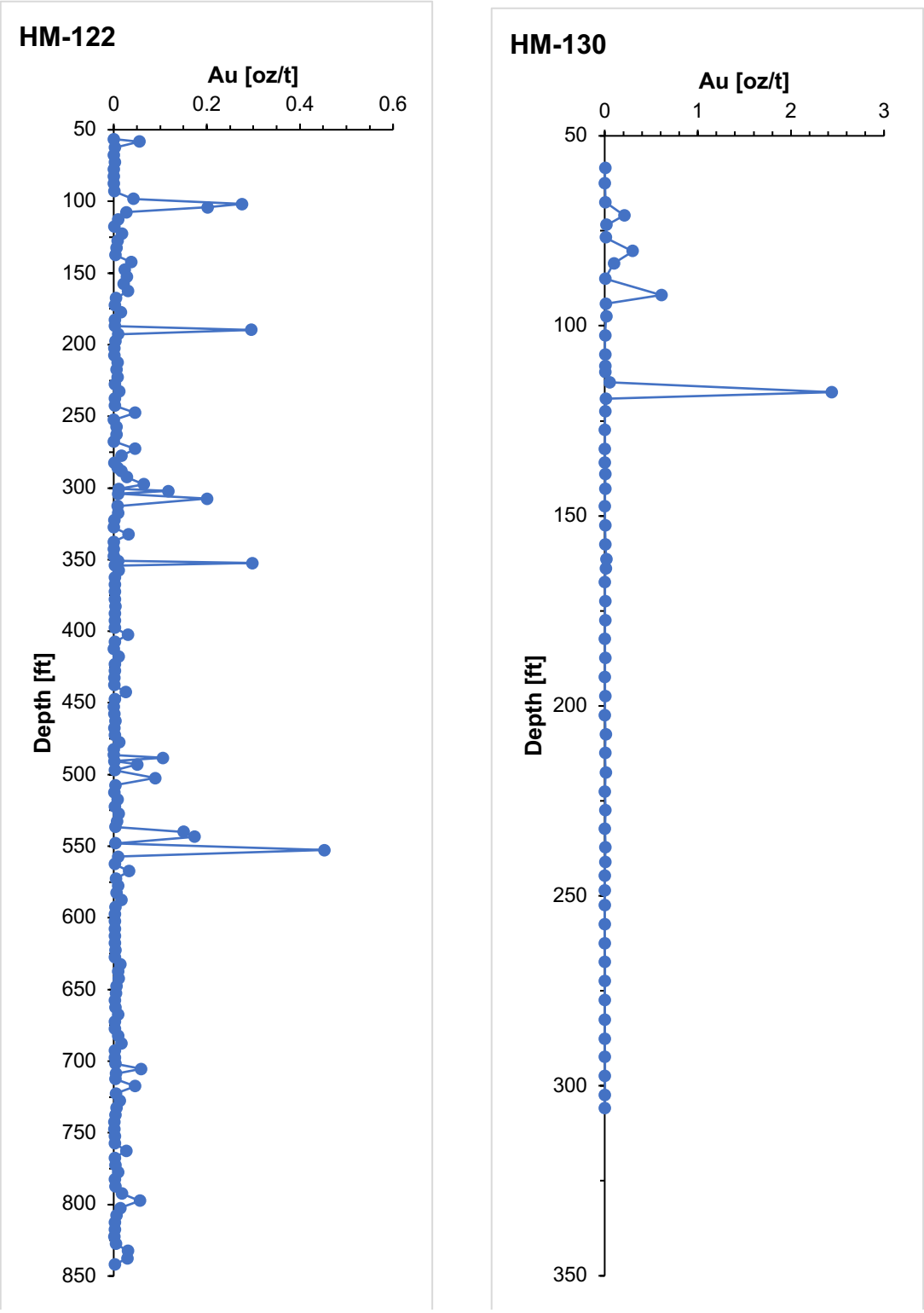

Figure A.2. *[continued]* HM-122 (left) and HM-130 (right).

Appendix B: Sample List

Table B.1. List of thin section samples collected for this study. Abbreviations: Apy – arsenopyrite, Bi_3Te – 'unnamed Bi_3Te phase', Bis – bismuthinite, Ccp – chalcopyrite, El – electrum, EPMA – electron microprobe analysis, ft – feet, Gn – galena, Hed – hedleyite, Hess – hessite, Mal – maldonite, N/A – not analyzed, native Au – native gold, native Bi – native bismuth, No. – number, oz/t – ounce per ton, Po – pyrrhotite, Py- pyrite, Qtz – quartz, RL – reflected light microscopy, SEM – scanned electron microscopy, SIMS – secondary ion mass spectrometry, Sp – sphalerite., Unknowns – unidentified phases (Bi±Te±Au±S phases), ✓ - analyzed.

Sample No.	Start Depth [ft]	End Depth [ft]	Lithology	Comment	Au grade [oz/t]	Ore mineralogy	RL	SEM	EMPA	SIMS
				HM-122						
4151	274.55	274.70	Qtz vein	Po + Py ± Ccp stringer	0.05	Po > Py >> Unknowns	✓	✓		✓
4152	302.50	302.65	Qtz vein	Disseminated Po ± Py	0.12	Po > Ccp	✓			
4153	306.05	306.20	Qtz vein-tonalite contact	Massive Po, Ccp + Py stringer	0.22	Po >> Py > Ccp	✓			
4154	352.25	352.40	Qtz vein	Massive Po + Py + Ccp	0.30	Po >> Py > Ccp >> Unknowns	✓			
4155	357.75	357.90	Qtz vein	Po ± Ccp + Apy stringer	0.01	Po >> Ccp > Py >> Apy > Unknowns	✓			
4156	370.25	370.45	Tonalite	Zoned xenolith with garnets	0.00	N/A				
4157	393.10	393.20	Qtz vein	Po + Ccp + Apy + Sp stringer	0.00	Po >> Ccp > Py >> Apy >> Sp	✓			
4158	444.50	444.70	Qtz vein	Po + Sp + Gn stringer	0.03	N/A				
4159	544.50	545.00	Qtz vein	Po + Sp ± Py stringer	0.17	Po > Py >> Ccp >> Sp	✓			
4160	552.40	552.55	Qtz vein	Po + Py + Ccp ± Sp stringer	0.54	Po >> Py > Ccp >> Sp	✓	✓		
4161	553.65	553.85	Qtz vein	Po + Py + Ccp ± Sp stringer	0.54	Po > Py > Ccp >> Unknowns	✓			
4162	796.10	796.20	Qtz vein	Po + Ccp + Py stringer	0.06	N/A				

Table B.1. *[continued]*

Sample No.	Start Depth [ft]	End Depth [ft]	Lithology	Comment	Au grade [oz/t]	Ore mineralogy	RL	SEM	EMPA	SIMS
				HM-114						
4163	156.92	157.30	Qtz vein	Po + Py stringer	2.22	Py >> Po > Sp	✓			
4164	156.60	156.69	Qtz vein	Po ± Py stringer	2.22	Py >> Po > Ccp >> Hed ~ Bi_3Te > native Bi > El ~ native Au	✓	✓	✓	
4165	257.70	257.90	Qtz vein	Qtz breccia with calcite	0.01	Py >> Ccp	✓			
4166	347.75	347.85	Qtz vein	Po stringer	1.21	Po >> Py > Ccp >> Unknowns	✓			
4167	434.30	434.65	Qtz vein	Qtz breccia with calcite and sulfides	0.00	N/A				
4168	593.80	593.90	Qtz vein	Massive Po with Po + Py stringers and disseminated Ccp	0.04	Po >> Ccp > Py >> Unknowns	✓			
HM-71										
4169	219.00	219.10	Qtz vein	Po + Ccp + Py stringer	0.34	Po >> Py > Ccp >> Sp > Hed ~ Bi_3Te ~ native Bi > Bis ~ El ~ native Au > Mal	✓	✓		✓
4170	220.10	220.20	Qtz vein	Po + Ccp + Py stringer	0.34	Po >> Py >> Unknowns	✓			
4171	270.15	270.25	Qtz vein	Brecciated qtz and calcite with Po + Py stringers	0.33	Po >> Py > Ccp >> Unknowns	✓			
4172	265.85	265.95	Qtz vein	massive Po	1.57	Po > Py >> Ccp > Unknowns	✓	✓		
4173	267.10	267.20	Qtz vein	Po + Ccp + Sp	1.57	Po >> Py > Ccp >> Sp > Hed ~ Bi_3Te > native Bi > El ~ native Au > Bis ~ Mal	✓	✓	✓	
4174	282.40	282.50	Qtz vein	Po + Ccp + Py stringer	0.13	Po >> Ccp > Py >> Unknowns	✓			
4175	231.40	231.50	Qtz vein	Po stringer with entire vein	0.14	Po >> Py >> Ccp	✓			

Table B.1. *[continued]*

Sample No.	Start Depth [ft]	End Depth [ft]	Lithology	Comment	Au grade [oz/t]	Ore mineralogy	RL	SEM	EMPA	SIMS
				HM-83						
4176	141.15	141.25	Qtz vein	Po stringer	0.23	Po > Py > Ccp >> Unknowns	✓			
4177	226.30	226.40	Qtz vein	Po + Py + Ccp stringer	0.10	Po >> Ccp > Py >> Unknowns	✓			
4178	226.55	226.65	Qtz vein	Po + Py + Ccp stringer on contact with selvage	0.10	Po > Py >> Ccp >> Unknowns	✓			
4179	235.70	235.80	Qtz vein	Po + Py + Ccp stringer	0.07	Po >> Py > Ccp	✓			
4180	256.80	256.90	Qtz vein	Po + Ccp stringers	0.10	Po >> Py > Ccp >> Unknowns	✓			
4181	303.65	303.75	Qtz vein	Po + Py stringers on upper selvage	0.06	Po > Py >> Ccp >> Sp >> Unknowns	✓			
4182	365.75	366.10	Qtz vein	Po + Ccp + Py stringers	0.08	Po > Py >> Unknowns	✓			
4183	72.35	72.45	Qtz vein	Po stringer and disseminated Po	0.11	Po > Py >> Ccp >> Unknowns	✓			
4184	74.25	74.35	Qtz vein	Vuggy Po + Py, disseminated Po, and Po + Py + Ccp stringers	0.06	Po >> Py > Ccp >> Apy	✓			
				HM-58						
4185	80.00	80.45	Qtz vein	Po + Py + Sp +Apy + Ccp	0.01	Py > Sp > Apy > Po > Gn >> Ccp > native Bi > Hess > Hed ~ Bi_3Te	✓	✓	✓	✓
4186	389.45	389.55	Qtz vein	Po + Py + Ccp stringers on contacts with selvage	0.04	Po > Py >> Ccp	✓			
4187	341.20	341.30	Qtz vein	Po + Py + Ccp stringer	0.06	Py > Po >> Sp > Unknowns	✓			
4188	490.85	490.95	Qtz vein	Po + Py + Ccp stringers, massive Po	0.14	Po > Py >> Ccp	✓			

Table B.1. *[continued]*

Sample No.	Start Depth [ft]	End Depth [ft]	Lithology	Comment	Au grade [oz/t]	Ore mineralogy	RL	SEM	EMPA	SIMS
				HM-58 *[continued]*						
4189	494.20	494.30	Qtz vein	Po + Py + Ccp stringers, massive Po	0.21	Po >> Ccp > Py	✓			
4190	501.30	501.40	Qtz vein	Po + Py + Ccp stringers, massive Po	0.36	Po >> Py > Ccp > Sp > Unknowns	✓	✓		
4191	501.80	501.90	Qtz vein	Po + Py + Ccp stringers, massive Po	0.36	Po > Py >> Ccp > Unknowns > Sp	✓			
4192	504.80	504.90	Qtz vein	Po + Py + Ccp stringers, massive Po	0.21	Po > Ccp	✓			
4193	509.80	509.90	Qtz vein	Po + Ccp stringer	0.04	Po > Py >> Ccp > Sp	✓			
4194	464.75	465.05	Qtz vein	Apy with Po+Py	0.01	Apy >> Po > Py >> Ccp	✓	✓	✓	✓
				HM-130						
4195	70.65	70.75	Qtz vein	Vuggy Po + Py with Po + Py stringer	0.21	Py >> Ccp ~ Po	✓			
4196	75.75	75.85	Qtz vein	Vuggy Po + Py with Po + Py stringer	0.01	Po > Py >> Ccp >> Unknowns	✓			
4197	82.80	82.90	Qtz vein	Massive Po with minor Ccp, Po + Py + Ccp stringer	0.10	Po > Py >> Ccp >> Sp	✓			
4198	91.80	91.90	Qtz vein	Po + Py + Ccp stringers	0.61	Po > Py >> Ccp >> Unknowns	✓			
4199	117.00	117.10	Qtz vein	Po + Py + Ccp stringers	2.44	Po > Py >> Ccp > Hed ~ Bi_3Te > native Bi > El ~ native Au > Bis ~ Mal	✓	✓	✓	
4200	117.25	117.35	Qtz vein	Po + Py + Ccp stringers	2.44	Po > Py >> Ccp > Hed ~ Bi_3Te > native Bi > El ~ native Au > Bis ~ Mal	✓	✓	✓	

Appendix C: Electron Microprobe Analyses

Table C.1 Pyrrhotite. Formula calculated on S = 1 atom. **Abbreviations:** apfu – atoms per formula unit, Apy – arsenopyrite, bdl – below detection limit, Bi – bismuth phase, BiAu – bismuth and/or gold phase, Bio – biotite, BSE – back scattered electron image, BiTe – bismuth telluride, Ccp – chalcopyrite, eu – euhedral, Gn – galena, Hess – hessite, incl – inclusion, Qtz – quartz, repl – replacing, Sp – sphalerite, Py – pyrite, blank space – not detected.

Sample No	**4173**	**4173**	**4173**	**4173**	**4173**	**4173**	**4173**	**4199**	**4173**	**4200**
BSE No	**SEM1**		**SEM1**	**SEM4**	**SEM2**	**SEM3**	**SEM2**	**SEM3**	**SEM4**	**SEM1**
Comment	**near Bi**	**center**	**far Bi**	**near Bi**	**far Bi**	**far Bi**	**near Bi**	**far BiAu**	**far Bi**	**center**
S [wt%]	39.1	39.2	39.3	39.3	39.3	39.3	39.3	39.3	39.4	39.4
Fe	61.7	61.6	60.5	62.0	61.3	61.3	61.7	61.8	61.5	61.3
Cu [ppm]		76		84	114	bdl			58	88
As				bdl		bdl				117
Zn										
Pb										
Au	591	489	299	97		bdl	115	138	298	147
Ag				62			56			
Hg									112	
Bi	103	bdl		211	bdl	289	308	109	146	172
Te				bdl	bdl	bdl	bdl		91	
Se			194		146				392	
Sb		65								
Cd	68	bdl	159	bdl	115		96	172	bdl	113
Cr										
Co	155	34	79	203	267	122	257	47	164	122
Ni		73	57		141	110	bdl	bdl		bdl
V			72				bdl	112		41
Ti	60	33	bdl	bdl	59	bdl	bdl			
Total [wt%]	**100.9**	**100.9**	**99.8**	**101.3**	**100.7**	**100.7**	**101.1**	**101.1**	**101.0**	**100.8**
					Formula: $Fe_{(1-x)}S$					
S [apfu]	1	1	1	1	1	1	1	1	1	1
Fe	0.90	0.90	0.88	0.91	0.90	0.90	0.90	0.90	0.90	0.89
x	0.10	0.10	0.12	0.09	0.10	0.10	0.10	0.10	0.10	0.11

Table C.1 Pyrrhotite. *[continued]*

Sample No	**4173**	**4173**	**4185**	**4200**	**4194**	**4199**	**4199**	**4199**	**4199**	**4173**
BSE No	**SEM5**	**SEM8**	**SEM2**	**SEM1**	**SEM1**	**SEM4**	**SEM3**		**SEM1**	**SEM7**
Comment	**far Bi**	**near Bi**	**within Sp and Gn**	**with Ccp rim**	**in veinlet**	**near eu Py**	**near BiAu**	**middle1**	**near Py near Bi**	**near Bi**
S [wt%]	39.4	39.4	39.4	39.5	39.5	39.6	39.6	39.6	39.7	39.7
Fe	61.5	60.9	59.9	61.2	60.2	61.7	61.3	61.3	59.9	60.4
Cu [ppm]			90	44			44			
As			bdl							
Zn			3239							
Pb			120							
Au	568	111		230		339	340	117	229	627
Ag			44	60	33	bdl	143		52	
Hg						114				
Bi	165	bdl	474	163	205	bdl	bdl	243	273	bdl
Te		53	104			99				
Se				122		bdl			144	
Sb			58							
Cd		106			bdl	155	51	96	43	
Cr					bdl					
Co	134	bdl	74	294	bdl	100	184	193	126	118
Ni	136	bdl	bdl	bdl	bdl					
V	114	bdl	32				bdl		32	34
Ti		bdl				bdl	48			98
Total [wt%]	**101.0**	**100.4**	**99.7**	**100.8**	**99.7**	**101.4**	**101.0**	**101.1**	**99.7**	**100.2**
					Formula: $Fe_{(1-x)}S$					
S [apfu]	1	1	1	1	1	1	1	1	1	1
Fe	0.90	0.89	0.87	0.89	0.88	0.89	0.89	0.89	0.87	0.87
x	0.10	0.11	0.13	0.11	0.12	0.11	0.11	0.11	0.13	0.13

Table C.1 Pyrrhotite. *[continued]*

Sample No	**4173**	**4173**	**4199**	**4173**	**4194**	**4199**	**4194**	**4194**	**4194**	**4194**
BSE No	**SEM7**	**SEM8**	**SEM1**	**SEM5**	**SEM10**	**SEM1**	**SEM1**	**SEM6**	**SEM1**	**SEM1**
Comment	**far Bi**	**far Bi**	**near BiAu**	**near Bi**	**in veinlet with eu Py**	**far Py near Bi**	**above Py 2**	**near Py Apy**	**between Py**	**above Py**
S [wt%]	39.7	39.9	39.9	39.9	40.0	40.0	40.0	40.0	40.0	40.0
Fe	60.5	60.9	60.9	60.9	59.9	61.0	59.7	61.3	59.8	61.4
Cu [ppm]	42	66				55			bdl	
As				bdl	115	bdl				
Zn									bdl	
Pb					bdl		160	bdl	134	
Au	431	255	243	332			145		318	178
Ag		61	95							
Hg	155								bdl	
Bi	352	453	bdl	141	253	351	bdl	80	278	bdl
Te		bdl	bdl		73					65
Se								271		bdl
Sb							bdl			
Cd	91			143		36	bdl	75	bdl	
Cr					bdl		bdl	bdl		bdl
Co	150	79	172	170		332	145		54	
Ni	46		93	62		42		104		109
V							bdl		bdl	
Ti	70	66	60			45		69	bdl	
Total [wt%]	**100.4**	**100.8**	**100.8**	**100.9**	**99.9**	**101.1**	**99.7**	**101.4**	**99.9**	**101.4**
					Formula: $Fe_{(1-x)}S$					
S [apfu]	1	1	1	1	1	1	1	1	1	1
Fe	0.87	0.88	0.88	0.87	0.86	0.88	0.86	0.88	0.86	0.88
x	0.13	0.12	0.12	0.13	0.14	0.12	0.14	0.12	0.14	0.12

Table C.1 Pyrrhotite. *[continued]*

Sample No	**4194**	**4199**	**4164**	**4194**	**4194**	**4194**	**4194**	**4194**	**4194**
BSE No	**SEM3**	**SEM3**	**SEM3**	**SEM9**	**SEM4_5**	**SEM10**	**SEM11**	**SEM4_5**	**SEM7**
Comment	**on thin section edge**	**near BiAu within Qtz**	**inclusion in Py**	**near Bio**	**around elongate Apy**	**veinlet rim on Apy**	**with Apy incl**	**with Py around Apy**	**center**
S [wt%]	40.0	40.0	40.1	40.1	40.1	40.1	40.1	40.2	40.3
Fe	61.3	60.5	59.7	59.6	61.2	59.8	61.3	59.7	59.8
Cu [ppm]	81					bdl	97	90	
As	239								389
Zn							bdl		
Pb			187		158		218	215	
Au	149			260	301	481		498	169
Ag					bdl	58	138		
Hg					bdl	103			
Bi	bdl	478	315		372		bdl	bdl	255
Te				bdl		81	65		
Se	bdl			bdl	369				
Sb									
Cd	40	bdl	52		33		128		
Cr	bdl		318	173	bdl		330	bdl	bdl
Co		bdl	381		33	80	44	174	74
Ni	192	47	86	111					61
V	bdl	bdl	58		73	93	bdl	53	
Ti	87					153		51	
Total [wt%]	**101.4**	**100.6**	**99.9**	**99.8**	**101.5**	**100.0**	**101.5**	**100.0**	**100.1**
				Formula: $Fe_{(1-x)}S$					
S [apfu]	1	1	1	1	1	1	1	1	1
Fe	0.88	0.87	0.86	0.85	0.88	0.86	0.88	0.85	0.85
x	0.12	0.13	0.14	0.15	0.12	0.14	0.12	0.15	0.15

Table C.2. Pyrite. Formula calculated on S = 2 atoms. **Abbreviations:** apfu – atoms per formula unit, Apy – arsenopyrite, bdl – below detection limit, Bi – bismuth phase, BiAu – bismuth and or gold phase, Bio – biotite, BSE – back scattered electron image, BiTe – bismuth telluride, Ccp – chalcopyrite, eu – euhedral, Gn – galena, Hess – hessite, incl – inclusion, Qtz – quartz, repl – replacing, Sp – sphalerite, Py – pyrite, blank space – not detected.

Sample No	**4194**	**4199**	**4194**	**4199**	**4194**	**4194**	**4164**	**4194**	**4185**	**4185**
BSE No	**SEM9**	**SEM1**	**SEM10**	**SEM1**	**SEM3**	**SEM6**	**SEM5**	**SEM4_5**	**SEM3**	**SEM6**
Comment		**near Bi**	**eu Py repl Po in veinlet**	**far Bi**	**on Au grain**	**near Po**		**with Po around Apy**	**near the Bi triangle**	**on Apy2**
S [wt%]	52.9	53.1	53.3	53.3	53.4	53.7	53.8	53.8	53.9	53.9
Fe	47.2	47.3	48.0	47.6	47.5	47.4	46.4	46.3	46.9	46.8
Cu [ppm]	bdl		212	bdl	142		85	bdl		45
As		186	333				183			bdl
Zn										
Pb	bdl				149	97	bdl	bdl		
Au	517	270	bdl	bdl		bdl	104	235	204	454
Ag							106			
Hg										
Bi	388	357		124	bdl	118	159	125	176	128
Te										
Se		63							144	200
Sb										
Cd	bdl			52	bdl		86			bdl
Cr	322				418		bdl			bdl
Co		46		101	bdl		240			
Ni	bdl	104		bdl			bdl	bdl	bdl	72
V				61	bdl	76	62		34	
Ti	33	32	112			118	bdl			67
Total [wt%]	**100.2**	**100.5**	**101.3**	**100.9**	**101.0**	**101.1**	**100.3**	**100.2**	**100.8**	**100.8**
					Formula: FeS_2					
S [apfu]	2	2	2	2	2	2	2	2	2	2
Fe	1.03	1.02	1.03	1.02	1.02	1.01	0.99	0.99	1.00	1.00

Table C.2. Pyrite. *[continued]*

Sample No	**4164**	**4194**	**4185**	**4164**	**4185**	**4185**	**4194**	**4164**	**4185**	**4164**
BSE No	**SEM6**	**SEM1**	**SEM2**	**SEM3**	**SEM10**	**SEM10**	**SEM1**	**SEM2**	**SEM6**	**SEM2**
Comment	**with Po inclusion**	**in Po on Apy rim**		**eu near BiTe**	**towards top**	**towards top**	**lower in Po on Apy rim**	**near whisps**	**on Apy**	**near skeletal**
S [wt%]	54.1	54.1	54.2	54.2	54.2	54.2	54.3	54.4	54.4	54.4
Fe	46.7	46.4	46.3	46.6	46.5	46.5	46.7	46.4	46.7	46.4
Cu [ppm]	95	139	bdl	bdl				49	bdl	
As		bdl	bdl		bdl					
Zn			1461							
Pb			430		bdl			91	96	
Au	204	158	224	99	337		bdl	bdl	537	358
Ag	40		80	35			49			bdl
Hg										
Bi				125	240			197	82	
Te	56			bdl						bdl
Se										
Sb		bdl								
Cd		142	63		bdl			bdl	52	52
Cr	bdl		bdl	bdl	514			bdl	bdl	168
Co	73	119		367		118	49		126	
Ni	bdl		70	98	bdl		bdl		bdl	bdl
V	37			bdl			bdl			59
Ti	96				71	bdl			54	
Total [wt%]	**100.9**	**100.6**	**100.7**	**100.8**	**100.8**	**100.7**	**101.0**	**100.8**	**101.2**	**100.9**
					Formula: FeS_2					
S [apfu]	2	2	2	2	2	2	2	2	2	2
Fe	0.99	0.98	0.98	0.99	0.99	0.98	0.99	0.98	0.99	0.98

Table C.2. Pyrite. *[continued]*

Sample No	**4185**
BSE No	**SEM7**
Comment	**near Sp**
S [wt%]	54.6
Fe	46.5
Cu [ppm]	bdl
As	
Zn	
Pb	bdl
Au	453
Ag	69
Hg	
Bi	
Te	
Se	
Sb	
Cd	34
Cr	176
Co	82
Ni	bdl
V	31
Ti	bdl
Total [wt%]	**101.2**
Formula: FeS_2	
S [apfu]	2
Fe	0.98

Table C.3. Chalcopyrite. Formula calculated on S = 2 atoms. **Abbreviations:** apfu – atoms per formula unit, Apy – arsenopyrite, bdl – below detection limit, Bi – bismuth phase, BiAu – bismuth and or gold phase, Bio – biotite, BSE – back scattered electron image, BiTe – bismuth telluride, Ccp – chalcopyrite, eu – euhedral, Gn – galena, Hess – hessite, incl – inclusion, Qtz – quartz, repl – replacing, Sp – sphalerite, Py – pyrite, blank space – not detected.

Sample No	**4173**	**4173**	**4194**	**4194**	**4194**	**4199**	**4199**	**4199**	**4199**	**4199**
BSE No			**SEM10**	**SEM10**	**SEM10**		**SEM4**	**SEM4**	**SEM2**	**SEM2**
Comment			**in veinlet1**	**in veinlet2**	**in veinlet3**	**middle1**	**on rim of Po with eu Py**	**on rim of Po with eu Py2**		**between Bi**
S [wt%]	34.8	34.8	35.1	34.8	34.8	35.2	35.1	34.9	34.8	34.5
Fe	30.7	31.1	31.1	31.2	31.1	31.1	31.1	30.9	30.9	30.7
Cu	34.6	34.5	34.7	34.4	34.5	34.4	34.3	34.3	34.5	33.8
As [ppm]			bdl			bdl				259
Zn										
Pb			270	166						
Au		bdl	bdl			498	205		222	249
Ag	97	93	44	87	296	88	153	198	262	96
Hg										
Bi	222		103	344	109	233	256		272	250
Te							79	40		
Se						bdl	132		bdl	165
Sb									42	
Cd		114	34	159	53			89	138	115
Cr				197						
Co	bdl	77				bdl	106		79	
Ni				102			bdl	122		68
V		56	bdl		bdl					36
Ti				97						
Total [wt%]	**100.1**	**100.5**	**101.0**	**100.6**	**100.4**	**100.7**	**100.6**	**100.1**	**100.3**	**99.1**
					Formula: $CuFeS_2$					
S [apfu]	2	2	2	2	2	2	2	2	2	2
Fe	1.01	1.03	1.02	1.03	1.03	1.02	1.02	1.02	1.02	1.02
Cu	1.00	1.00	1.00	1.00	1.00	0.99	0.99	0.99	1.00	0.99

Table C.3. Chalcopyrite. *[continued]*

Sample No	**4200**
BSE No	**SEM1**
Comment	**on rim of Po**
S [wt%]	34.6
Fe	30.4
Cu	34.2
As [ppm]	
Zn	
Pb	
Au	
Ag	108
Hg	
Bi	354
Te	
Se	
Sb	
Cd	bdl
Cr	
Co	
Ni	
V	31
Ti	
Total [wt%]	**99.4**
Formula: $CuFeS_2$	
S [apfu]	2
Fe	1.01
Cu	1.00

Table C.4. Arsenopyrite. Formula calculated on S = 1 atom. **Abbreviations:** apfu – atoms per formula unit, Apy – arsenopyrite, bdl – below detection limit, Bi – bismuth phase, BiAu – bismuth and or gold phase, Bio – biotite, BSE – back scattered electron image, BiTe – bismuth telluride, Ccp – chalcopyrite, eu – euhedral, Gn – galena, Hess – hessite, incl – inclusion, Qtz – quartz, repl – replacing, Sp – sphalerite, Py – pyrite, blank space – not detected.

Sample No	**4194**	**4194**	**4194**	**4194**	**4185**	**4185**	**4194**	**4194**	**4185**	**4194**
BSE No	**SEM3**	**SEM8**	**SEM3**	**SEM11**	**SEM6**	**SEM10**	**SEM10**	**SEM6**	**SEM6**	**SEM1**
Comment	**edge**	**with Py rim repl**	**with skeletal Py**	**incl in Po**	**near Py**	**on left with Sp**	**with veinlet**	**near Po+Py**	**edge of Py**	**far from veinlet**
S [wt%]	20.8	20.6	20.2	20.0	19.9	19.9	19.9	19.9	19.8	19.8
Fe	35.0	34.6	34.3	34.3	34.4	34.5	34.5	34.1	34.6	34.1
As	44.1	44.5	45.1	45.6	45.7	45.3	46.0	45.5	45.4	45.6
Cu [ppm]			bdl			49	85			
Zn										
Pb	597	321	356	290	857	182		468	394	351
Au	157	282	bdl	110	486	543	160	163	337	194
Ag	bdl	bdl								
Hg						bdl				
Bi		bdl		500				bdl		
Te			130		394	194			bdl	99
Se										
Sb			69							182
Cd	74	116		133		bdl	165		54	156
Cr	307	bdl	bdl	687	248	323	309		231	406
Co	bdl	442	123	1130	302	773		307	90	517
Ni	75	bdl					bdl		43	
V		89	155	bdl		83		83		
Ti	107		86		bdl	36	40			
Total [wt%]	**100.0**	**99.8**	**99.6**	**100.2**	**100.3**	**99.9**	**100.5**	**99.5**	**99.9**	**99.7**
					Formula: FeAsS					
S [apfu]	1	1	1	1	1	1	1	1	1	1
Fe	0.97	0.96	0.97	0.99	0.99	0.99	1.00	0.98	1.00	0.99
As	0.91	0.92	0.96	0.98	0.98	0.97	0.99	0.98	0.98	0.98

Table C.4. Arsenopyrite. *[continued]*

Sample No	**4194**	**4194**	**4194**	**4185**	**4194**	**4194**	**4194**	**4194**	**4194**
BSE No	**SEM4_5**	**SEM9**	**SEM7**	**SEM10**	**SEM10**	**SEM4_5**	**SEM1**	**SEM11**	**SEM7**
Comment	**in Py+Po**	**center**	**inside FeSiO**	**inclusion in Sp**	**near Py+Po rim**	**long incl in Po**	**grain in veinlet**	**with Po and incl**	**rim**
S [wt%]	19.8	19.8	19.8	19.7	19.7	19.7	19.7	19.6	19.5
Fe	34.3	34.3	34.4	34.3	34.2	34.6	34.3	34.3	34.4
As	45.6	45.6	45.5	46.0	45.6	45.6	45.8	45.4	46.1
Cu [ppm]		bdl	58	78					bdl
Zn				1326					
Pb	459	352		732	270	270	518	136	410
Au		422	230	285	183		175		
Ag					129	70			
Hg				bdl					
Bi						426	244		331
Te			bdl			bdl	94	53	
Se									
Sb					bdl				bdl
Cd		115		100		41		70	
Cr	428	349				747		447	
Co	548	145	894	134	477	1090	380	789	102
Ni		75		40					
V	bdl	bdl				70	75	bdl	48
Ti		73	82	bdl	102				
Total [wt%]	**99.9**	**99.8**	**99.8**	**100.3**	**99.6**	**100.1**	**99.9**	**99.5**	**100.1**
				Formula: FeAsS					
S [apfu]	1	1	1	1	1	1	1	1	1
Fe	0.99	1.00	1.00	1.00	0.99	1.01	1.00	1.01	1.01
As	0.98	0.99	0.99	1.00	0.99	0.99	1.00	0.99	1.01

Table C.5. Sphalerite. Formula calculated on S = 1 atom. **Abbreviations:** apfu – atoms per formula unit, Apy – arsenopyrite, bdl – below detection limit, Bi – bismuth phase, BiAu – bismuth and or gold phase, Bio – biotite, BSE – back scattered electron image, BiTe – bismuth telluride, Ccp – chalcopyrite, eu – euhedral, Gn – galena, incl – inclusion, Qtz – quartz, repl – replacing, Sp – sphalerite, Py – pyrite, blank space – not detected.

Sample No **BSE No** **Comment**	**4185** **SEM2** **interstitial Gn and Bi**	**4185** **SEM3** **on Bi**	**4185** **SEM1** **with Apy inclusion and Bi**	**4185** **SEM2** **with interstitial Gn and Bi**	**4185** **SEM10** **bottom left**
S [wt%]	33.7	33.5	33.5	33.4	33.4
Fe	7.75	7.71	7.93	7.60	8.25
Zn	58.1	58.1	57.9	58.3	57.4
Cd	1.14	1.05	1.09	1.04	1.06
Cu [ppm]					
As					bdl
Pb					
Au	289			100	180
Ag	bdl	bdl			
Hg			140		345
Bi	390	509	310	285	305
Te					
Se		339			
Sb		bdl			
Cr	bdl		bdl	bdl	331
Co	bdl				
Ni	bdl		81		
V		35	54		47
Ti			62	bdl	
Total [wt%]	**100.8**	**100.5**	**100.5**	**100.4**	**100.2**

Table C.5. Sphalerite. *[continued]*

Sample No **BSE No** **Comment**	**4185** **SEM2** **interstitial** **Gn and Bi**	**4185** **SEM3** **on Bi**	**4185** **SEM1** **with Apy** **inclusion and Bi**	**4185** **SEM2** **with interstitial** **Gn and Bi**	**4185** **SEM10** **bottom left**
			Formula: ZnS		
S [apfu]	1	1	1	1	1
Fe	0.13	0.13	0.14	0.13	0.14
Zn	0.84	0.85	0.85	0.86	0.84
Cd	0.01	0.01	0.01	0.01	0.01
Sum cations	*0.99*	*0.99*	*0.99*	*1.00*	*0.99*

Table C.6. Galena. Formula calculated on S = 1 atom. **Abbreviations:** apfu – atoms per formula unit, Apy – arsenopyrite, bdl – below detection limit, Bi – bismuth phase, BiAu – bismuth and or gold phase, Bio – biotite, BSE – back scattered electron image, BiTe – bismuth telluride, Ccp – chalcopyrite, eu – euhedral, Gn – galena, incl – inclusion, Qtz – quartz, repl – replacing, Sp – sphalerite, Py – pyrite, blank space – not detected.

Sample No **BSE No** **Comment**	**4185** **SEM7** **on with Bi grain**	**4185** **SEM7** **on Sp**	**4185** **SEM8** **with BiTe**	**4185** **SEM6** **inclusion in Apy**	**4185** **SEM2** **in Py 2**	**4185** **SEM6**	**4185** **SEM3** **on Bi and Hess**
S [wt%]	13.7	13.7	13.7	13.7	13.6	13.6	13.6
Pb	85.4	84.2	84.6	82.8	85.8	84.4	85.3
Ag	0.466	0.713	0.356	1.09	0.196	0.461	0.153
Bi	1.29	1.84	1.14	2.60	0.637	1.21	0.601
Fe [ppm]	2309	435	12915	2455	672	1624	4546
Cu							
As				185			
Zn					5901		7912
Au							
Hg							
Te	906	1160	554	383	663	907	783
Se	284	357	891	348	713	677	867
Sb							
Cd	44		172	96			
Cr	3118	2516	2523	2449	2876	1930	3011
Co	bdl						
Ni			bdl				
V				119			
Ti			97		136		81
Total [wt%]	**101.5**	**100.9**	**101.5**	**100.8**	**101.3**	**100.2**	**101.4**
			Formula: PbS				
S [apfu]	1	1	1	1	1	1	1
Pb	0.96	0.95	0.96	0.94	0.97	0.96	0.97
Ag	0.01	0.02	0.01	0.02	0.00	0.01	0.00
Bi	0.01	0.02	0.01	0.03	0.01	0.01	0.01
Sum cations	*0.99*	*0.99*	*0.98*	*0.99*	*0.99*	*0.98*	*0.98*

Table C.7. Native bismuth. Abbreviations: apfu – atoms per formula unit, Apy – arsenopyrite, bdl – below detection limit, Bi – bismuth phase, BiAu – bismuth and or gold phase, Bio – biotite, BSE – back scattered electron image, BiTe – bismuth telluride, Ccp – chalcopyrite, eu – euhedral, Gn – galena, incl – inclusion, Qtz – quartz, repl – replacing, Sp – sphalerite, Py – pyrite, blank space – not detected.

Sample No	**4185**	**4185**	**4185**	**4185**	**4164**	**4173**	**4164**	**4173**
BSE No	**SEM7**	**SEM2**	**SEM3**	**SEM8**	**SEM3**	**SEM4**	**SEM5**	**SEM7**
Comment	**with Gn**	**with the Hess**	**white**	**with Gn**		**phase 2**	**near Py**	**phase 1**
Bi [wt%]	99.9	100.4	100.0	100.6	98.2	100.1	98.0	99.7
Te					0.029			1.21
Au [ppm]								
Ag	276	57	253		46	90	206	304
S	191	50	48		213	116	24	
Fe	3790		576	7172	252	3114	1474	757
Cu								
As	1631	1729	960	1126	686	965	1125	657
Zn		7357	4250					
Pb								
Hg				159	279		bdl	
Se		507	151	275			458	220
Sb	180	432	571	514				196
Cd	137	336	275	360	366	222	247	249
Cr	2480	965	1003	2081	1305	1299	1030	465
Co	39						35	
Ni								
V							55	
Ti	146		76		bdl			
Total [wt%]	**100.8**	**101.6**	**100.8**	**101.8**	**98.5**	**100.7**	**98.5**	**101.2**

Table C.8. Unnamed bismuth telluride. Formula calculated on Te = 1 atom. **Abbreviations:** apfu – atoms per formula unit, Apy – arsenopyrite, bdl – below detection limit, Bi – bismuth phase, BiAu – bismuth and or gold phase, Bio – biotite, BSE – back scattered electron image, BiTe – bismuth telluride, Ccp – chalcopyrite, eu – euhedral, Gn – galena, incl – inclusion, Qtz – quartz, repl – replacing, Sp – sphalerite, Py – pyrite, blank space – not detected.

Sample No	**4173**	**4199**	**4199**
BSE No	**SEM1**	**SEM1**	**SEM1**
Comment			
Bi [wt%]	80.7	80.9	80.8
Te	16.8	17.0	17.0
Au [ppm]			
Ag			66
S	445	90	66
Fe	9462	208	
Cu			
As	645	373	1315
Zn			
Pb	981	253	458
Hg			
Se	1453	800	386
Sb	1804	1744	1756
Cd	244	171	113
Cr	1322	1847	377
Co	33	bdl	
Ni	37		
V			84
Ti	133	63	
Total [wt%]	**99.1**	**98.4**	**98.4**
Bi/Te	***4.80***	***4.77***	***4.74***
	Formula: Bi_3Te		
Bi [apfu]	2.93	2.91	2.90
Te	1	1	1

Table C.9. Hedleyite. Formula calculated on Te = 3 atoms. **Abbreviations:** apfu – atoms per formula unit, Apy – arsenopyrite, bdl – below detection limit, Bi – bismuth phase, BiAu – bismuth and or gold phase, Bio – biotite, BSE – back scattered electron image, BiTe – bismuth telluride, Ccp – chalcopyrite, eu – euhedral, Gn – galena, incl – inclusion, Qtz – quartz, repl – replacing, Sp – sphalerite, Py – pyrite, blank space – not detected.

Sample No	**4185**	**4173**	**4173**
BSE No	**SEM8**	**SEM4**	**SEM8**
Comment	**center**	**phase 1**	**phase 1**
Bi [wt%]	76.8	76.8	78.2
Te	20.5	20.4	20.0
Au [ppm]		113	
Ag	1568		146
S	854	181	18
Fe	13999	2391	
Cu			
As		777	367
Zn			
Pb		1087	253
Hg			
Se		1357	333
Sb	1108		2142
Cd	58	400	
Cr	1864	1319	1384
Co			48
Ni	56	148	
V	164	45	
Ti			
Total [wt%]	**99.3**	**98.1**	**98.6**
Bi/Te	***3.74***	***3.76***	***3.92***
	Formula: Bi_7Te_3		
Bi [apfu]	6.85	6.89	7.17
Te	3	3	3

Table C.10. Hessite. Formula calculated on Te = 1 atom. **Abbreviations:** apfu – atoms per formula unit, Apy – arsenopyrite, bdl – below detection limit, Bi – bismuth phase, BiAu – bismuth and or gold phase, Bio – biotite, BSE – back scattered electron image, BiTe – bismuth telluride, Ccp – chalcopyrite, eu – euhedral, Gn – galena, incl – inclusion, Qtz – quartz, repl – replacing, Sp – sphalerite, Py – pyrite, blank space – not detected.

Sample No	**4185**	**4185**	**4185**
BSE No	**SEM3**	**SEM9**	**SEM2**
Comment			**near Gn**
Ag [wt%]	63.3	63.2	61.4
Te	36.8	36.3	36.3
Au [ppm]			305
Hg	261		139
Bi	240	369	367
S	339	985	7696
Fe	620	1091	2759
Cu			
As			
Zn	4919	9053	18742
Pb		98	561
Se			
Sb	2277	2244	2216
Cd	103		271
Cr	1723	2021	1721
Co	37		
Ni	124	42	bdl
V	bdl	202	118
Ti	39		
Total [wt%]	**101.2**	**101.2**	**101.2**
Ag/Te	***1.72***	***1.74***	***1.69***
	Formula: Ag_2Te		
Ag	2.03	2.06	2.00
Te	1	1	1

Table C.11. Electrum. Abbreviations: apfu – atoms per formula unit, Apy – arsenopyrite, bdl – below detection limit, Bi – bismuth phase, BiAu – bismuth and or gold phase, Bio – biotite, BSE – back scattered electron image, BiTe – bismuth telluride, Ccp – chalcopyrite, eu – euhedral, Gn – galena, incl – inclusion, Qtz – quartz, repl – replacing, Sp – sphalerite, Py – pyrite, blank space – not detected.

Sample No	**4199**	**4199**
BSE No	**SEM1**	**SEM3**
Comment	**with BiTe phase 3**	**with BiTe phase 1**
Au [wt%]	91.4	89.7
Ag	8.31	9.10
Hg [ppm]	981	2256
Bi	7787	8633
Te	bdl	
S	628	696
Fe		bdl
Cu	68	bdl
As		
Zn		
Pb		
Se		
Sb		
Cd		156
Cr	2020	2573
Co	bdl	44
Ni	43	
V		
Ti	92	76
Total wt%	**100.9**	**100.2**
Au/Ag	***11.0***	***9.9***

Table C.12. Trace elements in quartz. SiO_2 =99.9 wt%. **Abbreviations:** apfu – atoms per formula unit, Apy – arsenopyrite, bdl – below detection limit, Bi – bismuth phase, BiAu – bismuth and or gold phase, Bio – biotite, BSE – back scattered electron image, BiTe – bismuth telluride, Ccp – chalcopyrite, eu – euhedral, Gn – galena, incl – inclusion, Qtz – quartz, repl – replacing, Sp – sphalerite, Py – pyrite, blank space – not detected.

Sample No	**4173**	**4173**	**4194**	**4173**	**4164**	**4164**	**4173**	**4164**	**4199**	**4164**
BSE No	**SEM1**	**SEM1**	**SEM4_5**	**SEM2**			**SEM4**		**SEM1**	
Comment	**with Bi rim**	**on Bi rim**	**on ApyPoPy grain**	**inclusion in Po**			**inclusion to side of Bi**		**near BiAu**	
S [ppm]	35	bdl	118		80		44	bdl		bdl
Fe	573		1611				645		bdl	
Cu	37				70			34		
As								bdl		
Zn										
Pb			52			bdl				
Au	216	bdl	173		147				108	
Ag		30	bdl		40					bdl
Hg				bdl	bdl	330	bdl		208	
Bi		92		bdl						309
Te					34			30	144	
Se				bdl						
Sb						269				
Cd		35		58	bdl	38				
Cr				bdl		bdl	51			
Co								bdl	bdl	
Ni	82	37								
V	31	60	bdl		35	bdl		65	62	
Ti	51	bdl	bdl	bdl	39				65	110
Total [wt%]	**100.03**	**99.94**	**100.16**	**99.92**	**99.97**	**99.98**	**100.00**	**99.93**	**99.98**	**99.96**
Totals_Trace elements [wt%]	**0.13**	**0.04**	**0.26**	**0.02**	**0.07**	**0.08**	**0.10**	**0.03**	**0.08**	**0.06**

Table C.12. Trace elements in quartz. *[continued]*

Sample No	**4199**	**4199**	**4185**	**4199**	**4185**	**4185**	**4199**	**4200**	**4200**	**4200**
BSE No	**SEM1**	**SEM3**		**SEM3**			**SEM3**	**SEM1**		
Comment	**far BiAu**	**far BiAu**	**within sulfides**	**far BiAu**	**outside Apy**	**veinlet intruding**	**center**	**incl in Ccp**	**center**	**center**
S [ppm]	68	358	bdl		113	bdl	bdl	52		57
Fe	bdl	bdl	178			1594				190
Cu	38	bdl						380		
As						bdl				
Zn										
Pb								73	148	
Au	129			182			120			
Ag					bdl		42	117	45	
Hg	137			319	210	383				
Bi			266		125		55	66		
Te				82			bdl			bdl
Se										
Sb										
Cd										
Cr	38			150		51				69
Co							bdl			45
Ni	bdl	bdl		bdl	bdl	bdl		86	34	
V			29			39	bdl	bdl	109	
Ti	125			bdl	53			bdl		43
Total [wt%]	**99.98**	**100.00**	**99.96**	**99.99**	**99.98**	**100.17**	**99.94**	**100.00**	**99.94**	**99.96**
Totals_Trace elements [wt%]	**0.08**	**0.10**	**0.06**	**0.09**	**0.08**	**0.27**	**0.04**	**0.10**	**0.04**	**0.06**

Table C.12. Trace elements in quartz. *[continued]*

Sample No	**4200**
BSE No	
Comment	**incl**
S [ppm]	bdl
Fe	219
Cu	
As	
Zn	
Pb	79
Au	
Ag	
Hg	bdl
Bi	
Te	
Se	
Sb	
Cd	
Cr	
Co	
Ni	
V	
Ti	
Total [wt%]	**99.94**
Totals_Trace elements [wt%]	**0.04**